ASSESSING AND IMPROVING STEAM-ASSISTED GRAVITY DRAINAGE: RESERVOIR HETEROGENEITIES, HYDRAULIC FRACTURES, AND MOBILITY CONTROL FOAMS

A DISSERTATION
SUBMITTED TO THE DEPARTMENT OF ENERGY
RESOURCES ENGINEERING
AND THE COMMITTEE ON GRADUATE STUDIES
OF STANFORD UNIVERSITY
IN PARTIAL FULFILLMENT OF THE REQUIREMENTS
FOR THE DEGREE OF
DOCTOR OF PHILOSOPHY

Qing Chen

May 2009

I certify that I have read this dissertation and that, in my opinion, it is fully adequate in scope and quality as a dissertation for the degree of Doctor of Philosophy.

(Anthony R. Kovscek) Principal Co-Advisor

I certify that I have read this dissertation and that, in my opinion, it is fully adequate in scope and quality as a dissertation for the degree of Doctor of Philosophy.

(Margot G. Gerritsen) Principal Co-Advisor

I certify that I have read this dissertation and that, in my opinion, it is fully adequate in scope and quality as a dissertation for the degree of Doctor of Philosophy.

(Roland N. Horne)

Approved for the University Committee on Graduate Studies.

Abstract

Steam-assisted gravity drainage (SAGD) is a promising approach for recovering heavy and viscous oil resources. In SAGD, two closely-spaced horizontal wells, one above the other, form a steam-injector and producer pair. The reservoir oil is heated by the injected steam and drains to the producer under the effect of gravity. The success of steam-assisted gravity drainage has been demonstrated by both field and laboratory studies mostly based on homogeneous reservoirs and reservoir models. A comprehensive understanding of the effects of reservoir heterogeneities on SAGD performance, however, is required for wider and more successful implementation. This dissertation presents an investigation of the effects of reservoir heterogeneities on SAGD. In addition, two potential methods, hydraulic fracturing and mobility control using foamed steam, are proposed and reported here to enhance SAGD performance, especially for heterogeneous reservoirs.

Reservoir simulations of SAGD are conducted with a number of realizations of Athabasca-type oilsand reservoirs that contain randomly-distributed shales geostatistically generated with a stochastic model. We interpret the complex effects of reservoir heterogeneities by identifying two flow regions, the near well region (NWR) and the above well region (AWR). Our simulations indicate that the drainage flow of hot fluids within the NWR, characterized by short flow length, is very sensitive to the presence of shale, whereas the expansion of the steam chamber in the AWR, characterized by long flow length, is affected adversely only when the AWR contains

long, continuous shale or a high fraction of shale. Vertical hydraulic fractures are found to improve steam chamber development considerably for reservoirs with poor vertical communication. For the synthetic reservoir under study, an increase in the oil production rate by a factor of two and considerable improvement of energy efficiency with the cumulative oil-steam ratio lifted from 0.2 to 0.3 bbl oil/bbl CWE steam are achieved by adding a vertical fracture.

The new concept of foam-assisted SAGD (FA-SAGD) is evaluated numerically with a foam simulator that incorporates the physical mechanisms of foam generation, destruction, and transport. To reduce computational costs, we develop a simplified foam model based on the assumption of local equilibrium of foam generation and coalescence at field scale. Foam displacements in a linear sandstone core are measured using pressure transducers, X-ray Computed Tomography (CT), and a visualization cell to quantify foam bubble texture. The local equilibrium approximation is validated, and good agreement between the experimental results and the predictions of the simplified model is found, with a minor mismatch in the entrance region. For the scenario under study, numerical simulation of the FA-SAGD process shows considerable improvement in the process efficiency over the conventional SAGD process. Live steam production is reduced by a factor of 5 for FA-SAGD compared to conventional SAGD. Consequently, cumulative oil production is increased by about 30% when production versus the volume of steam injected is compared for cases with and without foam.

Acknowledgements

First and foremost, I would like to express my sincere appreciation to my two advisors, Tony Kovscek and Margot Gerritsen. They both provided me with a great deal of freedom to explore the research area of my interest, and continuously supported and encouraged this work. Tony has been a constant source of knowledge and advice during my years at Stanford, and I have learned a tremendous amount while under his supervision. I am truly thankful for his patience, inspiring guidance, and, of course, the numerous hours he put in to correct this dissertation. Were not for Margot's trust and persistence, I would not have gotten this precious opportunity to come to Stanford six years ago and fulfil my doctoral dream today. For this and her enthusiasm and constant support of this work, I own her many thanks.

I wish to thank the members of my reading and examination committees, Roland Horne and Sally Benson, for their careful reading of the entire dissertation and many constructive comments on this work, and the chair of my examination committee, Mike Moldowan, for agreeing to chair my oral defense and insightful suggestions. I am also grateful to Louis Castanier, who was the reading comittee for my Ph.D. proposal, for invaluable suggestions, thoughtful discussion, and numerous helps in the lab during the course of this work.

I owe many thanks to my labmates in the SUPRI-A group, including Cindy Ross, Edgar Rangel-German, Bolivia Vega, Wenjuan Lin, and Jing Peng. Special thanks

are due to Tom Tang, who has been a great source of experimental ideas and trouble-shooting tips, and helped me greatly with designing and setting up the foam coreflood experiments.

I would also like to thank all the other faculties, staff, and fellow students of the Department of Energy Resources Engineering for making my years at the department so fruitful and enjoyable.

This work was prepared with the support of the U.S. Department of Energy, under Award No. DE-FC26-04NT15526 and the Stanford Graduate Fellowship. The support of the Stanford University Petroleum Research Institute (SUPRI-A) Industrial Affiliates is also acknowledged.

Finally, I would like to thank my family for their tremendous, unconditional support during these years. The continuous encouragement from my parents, Juanqiu Chen and Xingxing Xiong, is the source energy and powerful backing inspiring me to pursue my Ph.D. dream at Stanford. My special thanks go to my dearest wife Tianhong Chen whose understanding, patience, and love enabled me to complete this work. This dissertation is dedicated with love to my family.

Contents

List of Tables

List of Figures

Chapter 1

Introduction

Vast quantities of heavy and extra-heavy oil (bitumen) resources have been found worldwide. For example, an estimated original heavy oil in place of more than 1.8 trillion barrels is present in Venezuela, 1.7 trillion barrels in Alberta, Canada, and 20-25 billion barrels on the North Slope of Alaska, USA (Burton et al., 2005). Due to the high-viscosity nature of the crude, the efficient and economic recovery of these heavy oil and bitumen resources presents a significant challenge. At reservoir conditions, heavy oil normally has viscosity greater than 100 cp, and bitumen exhibits even greater viscosity, for example, 10^6 cp in Athabasca, Canada. At such high viscosity values, the oil flows extremely slowly through the formation. Thus, the recovery of the unconventional heavy oil requires efficient in-situ viscosity reduction.

Thermal-based methods have been developed extensively over the past several decades for heavy oil recovery. The essential idea of thermal-based methods is to heat up the reservoir and consequently increase the oil temperature to reduce its viscosity according to the strong temperature dependency of oil viscosity. The conventional thermal methods include cyclic steam stimulation, steam flooding, and in-situ combustion. With recent advances of horizontal well technology, a more-recently-developed technique, so-called steam-assisted gravity drainage (SAGD), has emerged

as one of the most promising techniques for recovering the huge resources of heavy oil discovered worldwide, especially for bitumen in Western Canada (Butler, 2001).

The purposes of this work are to investigate SAGD performance in heterogeneous reservoirs and to develop a modified SAGD configuration to enhance performance by the deployment of hydraulic fractures and combining the use of aqueous foam for mobility control with steam injection.

1.1 Research Background and Motivation

The concept of SAGD, initially proposed by Butler and his colleagues (Butler et al., 1981; Butler and Stephens, 1981), is shown schematically in Figure 1.1. In this process, two horizontal wells are placed close to the bottom of a formation, with one above the other at a short vertical distance (4–10 m). Steam is injected continuously into the upper well, and rises in the formation, forming a steam chamber. Cold oil surrounding the steam chamber is heated mainly by thermal conduction. As its temperature increases, oil becomes mobile and flows together with condensate along the chamber boundary toward the lower well that functions as a producer (Butler, 1998b). The SAGD technique enjoys many advantages over other thermal methods, especially the conventional steam flooding methods. SAGD overcomes the shortcomings of steam override by employing only gravity as the driving mechanism. This leads to a stable displacement and a high oil recovery. Moreover, in the SAGD process, the heated oil remains hot and movable as it flows toward the production well, whereas, in conventional steam flooding, the oil displaced from the steam chamber is cooled and is hard to push to the production well.

Several SAGD field pilots were carried out in western Canada in the late 1980s and the results reported in the literature are promising (Edmunds et al., 1994; Redford and Luhning, 1999). The reservoirs chosen for those field pilots, however, normally

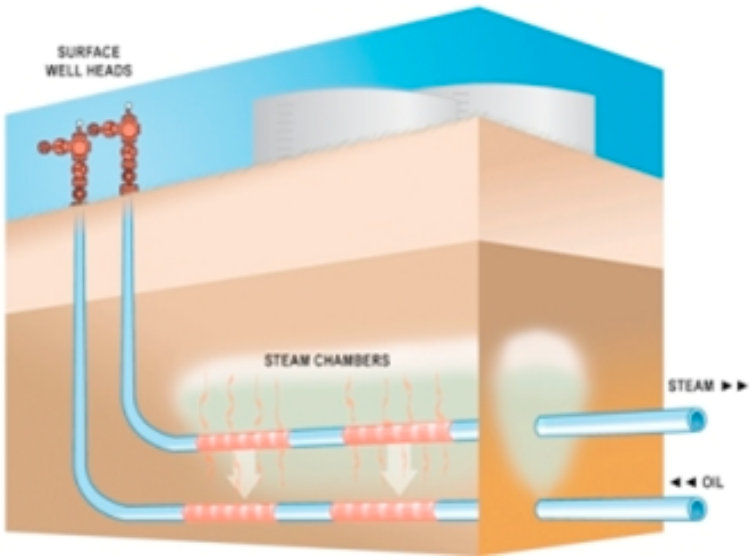

Figure 1.1: Schematic of a SAGD process (Courtesy of www.devonenergy.com).

consist of high quality, homogeneous formations. In reality, no reservoir is homogeneous because of natural geological features, such as shale, faults, and fractures. One example is the oil sand deposit in Peace River, Alberta, Canada. It contains a good deal of marine shale and mudstone, that forms continuous and discontinuous shale barriers throughout the formation (Webb et al., 2005).

As Farouq-Ali (1997) pointed out, the geology of the formation presents one of the major concerns in SAGD field applications. The heterogeneity introduced by shale barriers and other geological features plays an important role in the propagation of steam (Richardson et al., 1978) and thereby affects the overall performance of a SAGD process. For instance, steam often channels selectively through high permeability zones in a multiphase displacement because of its greater mobility compared with oil and water. In addition, because of the use of a long horizontal injector, the injectivity variance along the well due to the local heterogeneity makes it difficult to develop an even steam injection profile. As a result, the steam chamber forms only around well segments surrounded by high permeability formation.

Figure 1.2 gives a field example of unevenly-developed steam chambers that were observed at the Christina Lake SAGD project using a 4D seismic imaging technique (Zhang et al., 2007). There are four active well pairs, A1–A4 (well pairs A5 and A6 have limited production histories for analysis). The color in Figure 1.2 indicates the seismic amplitude difference between two seismic surveys conducted before and after steam injection. The steam chambers develop along the major portion of the well length, although not quite uniformly in the lateral direction, for A1, A2, and A4 areas, as evident in Figure 1.2. For A3 well pair, however, the steam chamber appears to cover approximately the two thirds of the well length on the heel side of A3 area. The pattern of steam distribution in the A3 area was found to be in high degree of correlation to the presence of low-permeability mudstone identified from high-resolution crosswell seismic (Zhang et al., 2007).

Apparently, the uneven development of the steam chamber as in the case of A3 well pair in Figure 1.2 leads to substantial reduction in the oil production rate and overall oil recovery. Such effects of reservoir heterogeneities on SAGD performance are worthy of a detailed study that provides knowledge for accurate, reliable predictions for field type systems.

The second aspect of this work is motivated by the need for SAGD improvement in heterogeneous reservoirs. Such improvement is crucial to broaden SAGD applications and unlock the huge, discovered heavy oil/bitumen resources worldwide. In this work, we propose hydraulic fracturing in the conventional SAGD configuration to mitigate the poor vertical communication accompanying the reservoirs with a large percentage of shale.

Moreover, in order to achieve more uniform steam chamber growth and better process efficiency, we introduce a new concept of foam-assisted SAGD (FA-SAGD), in which foamed steam is injected into the formation in the SAGD mode. Foam is frequently suggested to improve the sweep efficiency in multiphase displacement

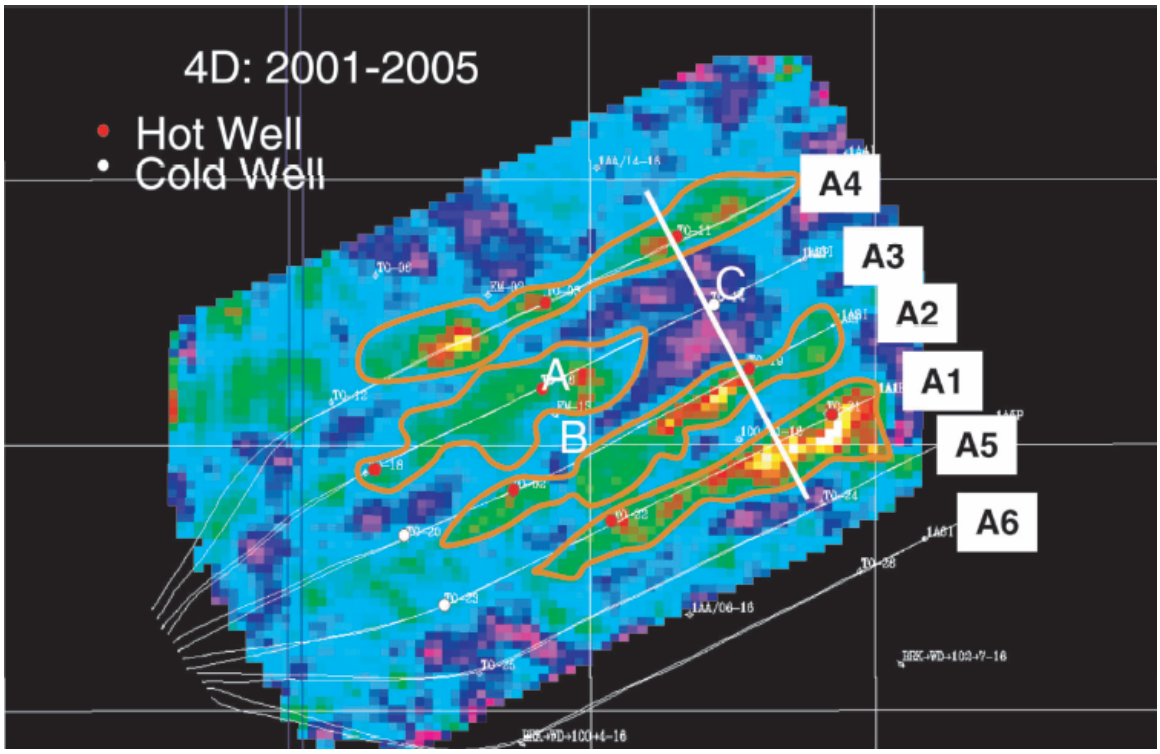

Figure 1.2: 4D seismic amplitude image of steam chamber growth at the Christina Lake SAGD project (Courtesy of Zhang et al., 2007).

processes (Patzek, 1996) and it provides a potential approach to enhance SAGD performance in a heterogeneous reservoir. Aqueous foams are formed by dispersing nonwetting gases within a continuous surfactant-laden liquid phase either by alternating or coinjecting gas and surfactant solution into porous media (Kovscek and Radke, 1994). Because foam encounters significant flow resistance in porous media, foaming the steam overcomes the adverse mobility of steam injection and possibly improves the steam chamber development in a SAGD process. To the best of the author's knowledge, deployment of foam in a SAGD process has not yet been investigated.

The actual performance of FA-SAGD should be evaluated experimentally and numerically. The current project focuses on the numerical perspective. An efficient, reliable simulation tool for modeling nonisothermal foam flow in porous media is desired for such studies. There are several foam modeling theories developed in the past decades, among which the population balance approach appears attractive due to its generality and similarity to the traditional mass and energy balance equations for flow in porous media. The population-balance model previously presented by Kovscek et al. (1995), however, exhibits certain limitations. First, Kovscek et al. (1995)'s model was developed to describe the high-quality or so called limiting capillary pressure regime. Secondly, the requirement of an additional equation for foam bubble population adds complexity to the implementation of the population-balance model, and also increases the computational cost of simulation runs. Hence, we need to develop a more effective foam model and then to simulate and assess the FA-SAGD process.

In summary, this report presents numerical, experimental, and theoretical research efforts aiming at assessing and improving SAGD performance in heterogeneous reservoirs.

1.2 Dissertation Outline

Chapter 2 summarizes literature on two research topics pertinent to this work, SAGD and aqueous foam in porous media. In the first section of that chapter, the development of the SAGD concept, process mechanisms, and laboratory and field studies are presented. The main focus is on several issues of considerable importance revealed from the SAGD field operations, including reservoir heterogeneity and steam trap implementation. Various modified SAGD configurations and SAGD derivatives that aim to accelerate and improve the efficiency of the SAGD process are also reviewed. The second section of Chapter 2 describes the previous research efforts for understanding and predicting foam behaviors in porous media. In that section, we first review foam generation, transport, and destruction mechanisms observed by microscopic and macroscopic-scale experimental studies. The existing theoretical foam models are then summarized, which is followed by a brief review of field-scale foam tests.

A numerical investigation of the effect of reservoir heterogeneity on SAGD using a stochastic model of shale distribution is presented in Chapter 3. The chapter starts with an analysis of flow characteristic length associated with the steam chamber in the SAGD process. The analysis leads to the definitions of two flow regions, the above well region (AWR) and the near well region (NWR) that make it possible in the subsequent numerical studies to interpret the complex effects of reservoir heterogeneity on the SAGD process. Numerical simulation results using CMG STARS with a number of equal-probability realizations in two dimensions are presented to compare SAGD performance. After discussion of the influence of shale distributions in AWR and NWR to the steam chamber development, a brief summary completes the chapter.

Hydraulic fracturing is discussed in Chapter 4 as a potential approach to accelerate steam chamber growth and therefore enhance SAGD performance for reservoirs with

poor vertical communication. We first introduce the basics of hydraulic fractures and discuss the fracture orientation in terms of in-situ stress and well orientations. After that, numerical predictions of SAGD performance for a highly heterogeneous reservoir in the absence and presence of horizontal or vertical fractures are presented. In the discussion of results, we comment on one major concern of live steam breakthrough with hydraulically-induced fractures that penetrate injection and production wells.

Chapter 5 presents the development of a simplified population-balance model based on local equilibrium between foam generation and coalescence for efficiently modeling foam flow in porous media. That chapter is composed of three main sections, foam modeling theory, experimentation, and results. The section of foam modeling theory provides the picture of the pore-level microstructure of foam during flow through porous media, and details the population balance approach that incorporates pore-level microstructure and texture-controlling mechanisms. In addition, the simplified population-balance model is developed and implemented with the local-equilibrium approximation.

The experimental setup and procedures of one-dimensional sandstone core-flood are presented in the section on experimentation. In the experiments, a visualization cell is employed to measure the effluent foam bubble sizes for a transient flow as well as to estimate the in-situ foam bubble sizes along the length of the core during steady flow. Additionally, the evolution of aqueous phase saturation is monitored using X-ray computed tomography (CT) and the pressure profile is measured by a series of pressure taps.

The section of results and discussion focuses on the verification and capability of the simplified model by examining the experimental results against the local-equilibrium assumption and numerical predictions. The experiments presented in this section include the in-situ measurement of foam texture along a 60 cm long core during during steady-state foam flow, and two transient foam flows, one with

surfactant presaturated core and the other brine presaturated core. Moreover, a field-scale radial foam flow case study is presented to illustrate the capability of the local equilibrium model. Finally, a summary of main findings completes the chapter.

Chapter 6 introduces the concept of foam-assisted SAGD and presents a numerical evaluation of FA-SAGD. Two potential benefits of foaming steam in a FA-SAGD process are first discussed. In order to simulate the FA-SAGD process, details of additional code development is provided to address the effects of the presence of the oil phase and high temperature on foam generation and coalescence that are necessary for modeling the FA-SAGD process. After giving a description of the synthetic reservoir model, we verify the capability of our own foam simulator for simulating SAGD-type processes by comparing its prediction of a typical SAGD with the Butler's analytical solution and STARS simulation results. Then, the performance of FA-SAGD is evaluated numerically with the recently-developed foam simulator and compared side-by-side with SAGD in terms of oil production and key parameter profiles.

Finally, we draw conclusions and make recommendations for future work in Chapter 7. Our recommendations include three-dimensional simulation and laboratory experiment of FA-SAGD as well as potential applications of FA-SAGD to naturally fractured carbonate reservoirs.

Chapter 2

Literature Review

Extensive research efforts have been devoted to the understanding of physical mechanisms and the development of mechanistic theories for SAGD and aqueous foam flow in porous media. In this chapter, we review the previous work on these two topics.

2.1 Steam-Assisted Gravity Drainage

2.1.1 SAGD Concept and Mechanics

The concept of SAGD was introduced originally by Butler and his former colleagues at Imperial Oil as a schematic technique for bitumen recovery in the late 1970s (Butler, 1998b; Butler et al., 1981; Butler and Stephens, 1981). As described in Chapter 1, the main feature of SAGD depends on introducing steam into a reservoir to form a steam chamber and producing heated oil using two horizontal wells by gravity. Since the oil production is mainly from the chamber/heated-oil interface, the steam chamber growth is responsible for oil production. Hence, a good deal of research work has focused on the analysis of steam chamber development and the associated physical processes, including counter-current flow at the top of the steam chamber

and cocurrent flow along the slope of the steam chamber.

From his sandpack laboratory experiment, Butler (1994) observed separate and ragged steam fingers, rather than a flat front at the top of steam chamber during the rise of the chamber. Butler attributed the occurrence of these fingers to instability caused by rising lighter steam below heavy oil. In his steam fingering theory, Butler (1994) described the rise of the steam chamber as a dome-shaped structure with steam fingers protruding from its upper surface. Steam flows into these fingers, condenses on their surface, and heats up the oil around the fingers. The heated oil drains downward around the perimeter of the fingers into the steam chamber where it meanders in counter-current flow against the steam. With a two-dimensional visual model, Sasaki et al. (2001) showed images of steam fingering during the rise of the steam chamber. They also reported increasing instability of the steam chamber interface near its ceiling, *i.e.*, steam fingering, with intermittent steam injection from the lower horizontal well. Ito and Ipek (2005) examined the steam fingering phenomenon with the measured field data from UTF Phase A, Phase B, Hangingstone, and Surmount SAGD projects. They expanded Butler's steam fingering theory and concluded that many observations in those field projects are clearly explained by the steam fingering concept.

Nasr et al. (2000) studied the steam-liquid countercurrent and cocurrent flows for different permeabilities and initial gas saturations with a nonsteady state, laboratory steam-front dynamic tracking technique and a CMG STARS numerical model. They performed two-dimensional scaled gravity drainage experiments designed to represent heavy oil/bitumen reservoirs. They made visual observations of the development of the steam chamber during the experiments and compared to numerical model predictions. In their conclusion, Nasr et al. (2000) indicated that the countercurrent steam front propagation rate is not a linear function of permeability, whereas the propagation rate, for a given permeability, is a linear function of time. They also

observed that for the same permeability, the countercurrent steam front propagates much slower than the cocurrent front. By history matching the experimental results using the numerical model, Nasr et al. (2000) determined the steam-water countercurrent and cocurrent relative permeability curves that show significant difference. They attributed the difference in the countercurrent and cocurrent relative permeabilities to the results of viscous coupling between phases.

Understanding heat transfer through the steam chamber is crucial to analysis and modeling of steam chamber growth and consequently the prediction of oil production and process efficiency. In the original SAGD concept, Butler assumed that heat transfer to cold oil ahead of the steam chamber is by conduction only. Farouq-Ali (1997) criticized such an assumption and argued that the strong condensate flow between steam and oil along the steam chamber slope is expected to result in more dominant convection. His statement was supported by the numerical simulation results presented in Ito and Suzuki (1999)'s paper. In response to that, Edmunds (1999) analyzed the associated change in enthalpy of fluids flowing inside and along the steam chamber. He stated that the liquid water could carry and deposit 18% of the heat of condensation of the same water. Another 4% of the latent heat would be transferred by convection due to oil flow and the remaining 78% would be carried by conduction. Edmunds (1999)'s further evaluation showed that the convection role due to water streamline being almost parallel to isotherms is less than 5%. Therefore, Edmunds (1999) stated that except for the very near vicinity of the liner or anywhere live steam penetrates, heat transfer in the mobile zone is dominated by conduction, not convection.

2.1.2 SAGD Prediction

Accurate prediction of SAGD performance in a reservoir is vital to successful project screening, efficient process optimization, and real field applications. Based on the

SAGD concept described in the previous section, Butler (1998b) developed an analytical model to predict the drainage rate. The evaluation of SAGD performance has also been achieved by conducting scaled sandpack experiments with appropriate scaling criteria. Numerical simulation, especially with the increasing CPU capability, has been applied extensively to model and predict the SAGD process in more complicated reservoir settings. Next, we review briefly the previous research work related to the above-mentioned prediction approaches.

By using Darcy's equation with countercurrent gravity drainage of mobilized bitumen (or heavy oil) and considering steam chamber geometries, Butler (1994, 1998b) developed a gravity drainage theory and derived semianalytical numerical models. The assumptions made in his gravity drainage theory include that only steam flows in the steam chamber, oil drains along the vertical steam chamber boundary, the steam pressure is constant in the steam chamber, oil saturation is residual, and heat transfer ahead of the steam chamber to cold oil is only by conduction. Eq. (2.1) provides one of the analytical equations for oil drainage rate obtained from Butler's theory.

$$q_o = L\sqrt{\frac{1.5\phi\Delta S_o k g \alpha h}{m\nu_s}} \quad , \tag{2.1}$$

where, L is the length of the horizontal well, ϕ is the porosity of the formation, ΔS_o is the difference between initial oil saturation and residual oil saturation to steam, k is the effective permeability for the flow of oil, g is the acceleration due to gravity, α is the thermal diffusivity, h is the steam chamber height, m is a constant between 3 and 4 depending on the oil viscosity versus temperature relation, and ν_s is the kinematic viscosity of oil at steam temperature. All the variables in Eq. (2.1) have equal weight in affecting the oil drainage rate, *i.e.*, changing any variable by a factor of n changes the predicted rate by a factor of $\sqrt{n}$.

Derivation of Butler's model (Eq. (2.1)) not only includes the dependency of the drainage rate on the drainage height, but also takes into account the shapes of the interface and boundaries, thereby providing more accurate prediction than the original model presented in Butler's earlier work. Butler further included the rising period of the steam chamber in his theory and provided an integrated approach to calculate analytically oil production as a function of time through a set of equations. More details can be found elsewhere (Butler, 1998b).

Reiss (1992) proposed modifications to Butler's gravity drainage model by using an empirical dimensionless temperature coefficient and the maximum velocity. He stated that such changes lead to more realistic representation of the experimental data reported in the literature and reported successful matches with some literature data. Recently, Akin (2004) modified the model by incorporating asphaltene content dependent viscosity to better match experimental data in the literature.

Butler also investigated the process experimentally. Most of laboratory studies of SAGD were carried out on sandpack models. Butler's early experiments gave an oil drainage rate consistent with the prediction by his semianalytical solution (Eq. (2.1)). Butler also developed scaling theory to estimate the corresponding oil production in field scale from lab-scale sandpack experiments.

Numerical simulation has been used widely by many researchers to investigate the physical process and practical operation of SAGD. Chow and Butler (1996) investigated the feasibility using a commercial CMG simulator (STARS) to history match the SAGD process. Their numerical results agreed reasonably with the measured data for cumulative oil production, recovery percentage, and temperature profiles in the model at different times. Edmunds et al. (1994) conducted two- and three-dimensional simulations to analyze steam trap control in SAGD. They found that two-dimensional simulations are normally optimistic for general SAGD problems. A numerical simulation study of the SAGD field application was reported by Ito and

Suzuki (1999). They predicted recovery performances of the SAGD project in the Hangingstone oil sands reservoir and investigated recovery mechanisms and subcooling temperature optimization. Tan et al. (2002) performed a numerical investigation of the importance of using a discretized wellbore for SAGD simulation and they found that a discretized wellbore model is necessary for accurately predicting temperature and saturation profiles for start-up and production of SAGD well pairs.

2.1.3 SAGD Field Pilots and Major Concerns

The first field-scale test of SAGD was AOSTRA's Underground Test Facility (UTF) project in Athabasca that was initiated by Butler's proposal (Butler, 1998a). The project started in 1988 with Phase A involving three short well pairs closely spaced (50 m in horizontal length and 25 m apart). The success of this pilot led to two succeeding phases, Phase B and D, where five additional well pairs 500 m long and 70 m apart were drilled. This pilot was operated until June 2004 and was reported to be successful with performance in agreement with expectations, *e.g.*, an ultimate recovery in excess of 65% and an oil-steam ratio (OSR) of 0.42. Another early field example of SAGD is the SAGD project in Tangleflags North field in the Lloydminster area that has been operated by Sceptre Resources since 1989. That project utilized horizontal production wells combined mostly with multiple vertical injectors. It was reported that more than 400,000 m^3 of oil had been produced with a COSR of 0.32 over operation lifetime.

Encouraged by those promising field test results, more than ten commercial SAGD projects have been operating in Canada, mainly in the Athabasca area in the past two decades. Recently, Jimenez (2008) presented a detailed review of the field performance of the existing SAGD projects in Canada. He analyzed a total of 32 pads from eight different SAGD operations. In his conclusion, Jimenez (2008) emphasized the geology and the operation as the key parameters for a successful SAGD process. He stated

that the ultimate average recoveries of SAGD were expected to be around 60 to 70% with dry COSR ranging from 0.30 to 0.50.

Despite the successful results from some projects, field applications of the SAGD process have revealed several issues of considerable importance to the recovery performance. Farouq-Ali (1997) pointed out that geology of the formation could have a profound influence on steam chamber growth. Similarly, Jimenez (2008) concluded from his analysis of the existing SAGD projects that slight differences in geology could easily reveal contrasting performances even over contiguous pads. Another major concern in SAGD applications is the well controls, or more specifically, steam trap control at wells for preventing live steam production. Next, we will focus on these two issues and review relevant research works in the literature.

Effect of Reservoir Heterogeneity

Due to the nature of reservoir geology, heterogeneity always exists in a formation, sometime with significant variations even within the same field. As illustrated in Chapter 1, the limited steam chamber growth observed using 4D and crosswell seismic images at the Christina Lake SAGD project (Zhang et al., 2007) gives a good example demonstrating the importance of reservoir heterogeneity effect on SAGD performance. Another example is UTF Phase A where the observed steam chamber in UTF Phase A was oblate and expanded sideways rather than vertically to the top of the formation. Farouq-Ali (1997) attributed this to small differences in formation characteristics.

Over the past decades, the role of reservoir heterogeneities in the steam chamber development for a SAGD process has been investigated numerically and experimentally.

Joshi and Threlkeld (1985) studied reservoirs with shale barriers and compared

the effects of various well configuration schemes as well as vertical fractures experimentally. They indicated that vertical fractures perpendicular to a horizontal injector improved oil recovery rate as compared with a horizontal injector/horizontal producer. Yang and Butler (1992) conducted SAGD experiments with reservoirs of two different types: reservoirs with horizontal layers of different permeabilities and reservoirs with thin shale layers. They observed faster production when a higher permeability layer located above a lower permeability layer than a lower permeability layer located above a higher permeability layer. For the effect of shale, they compared the experimental runs with horizontal barriers of different lengths placed in their two-dimensional scaled reservoir model. They found that a short horizontal barrier does not significantly affect the general performance of the SAGD process. The presence of a long barrier decreases the production, but, in some configurations, not as seriously as expected.

Kamath et al. (1993) presented a numerical investigation of SAGD performance in a layered reservoir. They found that the placement of horizontal producer in a high permeability zone significally improves the rate of recovery at early times. They also compared cases with 5 ft thick continuous shale barriers located above the injector and producer, and their results indicated that the presence of shale significantly lowers the oil recovery and increases SOR. Kisman and Yeung (1995) conducted a sensitivity test on flow barriers (discontinuous carbonate lenses) in their numerical studies of the SAGD process in the Burnt Lake Oil sands lease and reported results consistent with that presented earlier by Yang and Butler (1992) based on laboratory experiments.

Bagci (2004) reported experimental studies of the effect of fractures and well configurations on the SAGD processes. He used a 30 cm $\times$ 30 cm $\times$ 10 cm rectangular-shaped box model equipped with 25 thermocouples and obtained temperature profiles along time that visualize the effect of fractures on the steam chamber growth. His

experimental results indicated that vertical fractures improved SAGD. He also observed higher SORs during the early stage in the fractured model than those in the uniform permeability reservoir. Therefore, he stated that the vertical fracture could be used to improve the initial oil production rate. In a later paper, Bagci (2006) reported numerical simulation of his previous experiments. A reasonable agreement was found between the history-matched numerical simulation and the experiment in terms of oil production, steam chamber and temperature profiles.

Steam Trap Control

Avoiding steam breakthrough in the SAGD process is critical to ensure the energy efficiency and thus the economics of the process. A steam trap control is normally used as an operational control to reduce or prevent steam withdrawal from the steam zone in the reservoir (Doan et al., 1999). Das (2005) identified three main advantages of steam trap control to the SAGD process: 1) energy conservation and SOR reduction, 2) reduction of high vapor flow in wellbore that affects adversely the lifting capacity of the well and surface facilities, and 3) reduction of sands and fines movement through the liner that may cause erosion.

The steam trap control is generally achieved by adjusting the fluid withdrawal rate from the production well such that the temperature of the produced fluid remains below the steam saturation temperature by a preset subcooling temperature. The issue of subcooling has attracted a good deal of attention from researchers studying SAGD. Based on their experimental observations, Joshi and Threlkeld (1985) stated that production temperatures about 20 °C below steam temperatures are generally sufficient to establish a definite liquid leg above the producer, with no short circuiting of steam. Edmunds (1998), however, criticized Joshi and Threlkeld (1985)'s conclusions because their model experiment was operated at slightly above atmosphere pressure and was not well-scaled thermally.

Edmunds (1998) reviewed three approaches of steam trap controls in numerical simulations. One is setting injection and production pressures to the same value. In this case, steam can never enter the producer because there is no potential difference, but liquids can be produced by gravity alone, with just a few meters of liquid head. The second is to use a gas rate constraint to produce a small amount of steam. It is usually not possible to reduce the steam rate to a completely insignificant value and keep a stable solution, but this approach seems to guarantee maximum production. The third is called thermodynamic approach that is based on a downhole thermocouple and some estimate of reservoir or bottom hole pressure.

With two- and three-dimensional simulation models, Edmunds (1998) analyzed SAGD steam trap control with the thermodynamic approach. He found that for a specific case a steam trap of 20–30 °C is optimum. Ito and Suzuki (1999)'s simulation study showed that optimum subcooled temperature, based on minimization of the SOR at moderate recoveries, is about 30–40 °C for the SAGD process in the Hangingstone reservoir. Das (2005) noticed a positive effect of subcool temperature of higher than 20 °C.

In a typical SAGD configuration, however, the short vertical spacing (about 5 m) between injectors and produces makes it challenging in field operations to maintain a subcool condition at the producers, *i.e.*, no live steam production. Farouq-Ali (1997) expressed concern that operating wells from surface with steam trap control is difficult. Das (2005) also commented in his paper that it is very difficult in the field to control steam breakthrough due to the uneven nature of reservoir heterogeneity and the well trajectory. In order to minimize steam breakthrough, he proposed an alternative SAGD configuration in which the injected and the produced fluids flow in the same direction and thus the pressure drop along the well segment between the injectors and producers is more even. This new configuration, though, requires multiple pads, causing additional capital expense.

2.1.4 SAGD Improvement

It is believed that consistent steam chamber growth is necessary for a successful SAGD process. In order to improve SAGD performance, researchers have proposed various modifications to the classical configuration resulting in a number of derivative processes. Those modifications focus mainly on accelerating steam chamber growth and enhancing heat efficiency. According to the mechanisms of the changes made to SAGD, Albahlani and Babadagli (2008) in a recent review classified the modified SAGD processes into two categories: geometrical attempts and chemical attempts.

The geometrical approach attempts to alternate pressure differential points related to well placement in order to fasten steam chamber expansion. Polikar et al. (2000), for example, proposed a so-called Fast-SAGD process that utilizes additional single horizontal wells alongside the SAGD well pair. Those single horizontal wells (called offset wells) are operated in a cyclic steam stimulation (CSS) mode after the steam chamber anchoring at the SAGD well pair has fully developed and has reached the top of the pay zone. The CSS operation at the offset wells creates a pressure sink in the lower part of the reservoir by which steam is driven downward against its tendency to rise due to gravity. This helps the steam chamber expand laterally. From their two-dimensional simulation studies, Shin and Polikar (2006) concluded that the Fast-SAGD has a lower cumulative steam-oil ratio due to thermal efficiency and higher oil recovery as much as 34% greater than conventional SAGD.

Stalder (2007) described an alternative SAGD configuration that was termed as Cross-SAGD (XSAGD). In XSAGD, a series of horizontal injection wells are placed perpendicular, rather than parallel as in SAGD, to the producers, creating a mesh of wells. During the process, the plugging or flow-restricting operation is applied to the producers and injectors cross points following a strategic timing and thus to increase drainage rate while minimizing steam short-circuiting. Stalder (2007)'s simulation comparison of SAGD and XSAGD showed accelerated recovery and higher thermal

efficiency in XSAGD. He also pointed out two penalties with the XSAGD concept. First, in the early stage, only portions of wells near cross points are effective for steam chamber growth, therefore giving a limited initial production rate. Second, the complex plugging operation requires additional cost and poses a serious practical challenge to operations.

The chemical approach attempts to improve heat efficiency and reduce the oil water interfacial tension to achieve a higher production. The examples include noncondensable gas (NCG) or SAGP and expanding solvent SAGD (ES-SAGD). In the former, noncondensable gas is coinjected with steam into the reservoir. As described by Butler (1998b), for the process of SAGP, a very high concentration of noncondensable gas accumulates in the steam chamber, particularly near the top, thereby resulting in a lower temperature at the top and providing a thermal cushion to reduce heat loss to the overburden. It was reported, however, that the addition of noncondensable gas to injected steam gathers at the leading edge of the steam chamber and retards the growth of the steam chamber (Ito et al., 2001). On the other hand, addition of gas to steam injection in the later stage results in an improved steam-oil ratio.

ES-SAGD was developed by Nasr et al. (2003). The essential idea of ES-SAGD is coinjection of hydrocarbon additive (solvent) with steam at low concentration. Solvent, normally existing in its vapor phase at the elevated injected steam temperature, condenses with steam at the boundary of the steam chamber causing oil dilution and further viscosity reduction as well. Experiments conducted with two-dimensional models for Cold Lake-type live oil showed improved oil recovery and rate, enhanced noncondensable gas production, lower residual oil saturation, and faster lateral advancement of heated zones (Nasr and Ayodele, 2006).

2.2 Foam Flow in Porous Media

In 1961, Fried demonstrated that aqueous surfactant-stabilized foam could significantly reduce the mobility of gases in porous media (Fried, 1961). This unique property of reducing gas mobility makes foam highly applicable in gas mobility control in improved oil recovery. Traditional oil recovery by steam or carbon dioxide processes, for example, is observed to be much lower than expected due primarily to the poor sweep efficiency (Henry et al., 1996; Rossen, 1996). The low sweep efficiency is mostly attributed to channeling, gravity override, and viscous fingering in the gas-displacement processes because the residual oil and water are more viscous and denser compared with the injected gaseous drive fluids. Foaming the injected gases increases the gas-phase resistance dramatically, and thereby providing mobility control to improve the sweep efficiency and oil production. Foam applications, however, require knowledge to predict and control foam behavior to achieve the desired purpose. Consequently, both experimental and modeling studies have been extensively carried out for better understanding of the mechanisms as well as behaviors of foam in porous media.

2.2.1 Mechanisms and Behaviors of Foam in Porous Media

Visualization at the microscopic level provides direct observations of foam phenomena in porous media. Microscopic visualization is achieved by using micromodels that normally consist of a silicon wafer or a glass plate on which different pore network patterns, homogeneous or heterogeneous, are etched (Chambers and Radke, 1991; Mast, 1972; Owete and Brigham, 1987; Shirley, 1988). Based on numerous micromodel observations, Gillis and Radke (1990) proposed a pore-level picture of foam bubble distribution (see Figure 5.1 in Chapter 5) during flow through porous media. In their highly schematic picture, the aqueous wetting phase occupies the smallest

pore space, and foam bubbles reside in the intermediate or the largest pore space, depending upon whether they are flowing or stationary. Regardless of whether foam is generated in situ or externally, foam bubbles are continuously molded and shaped by the porous medium through complicated foam generation and destruction processes.

Several foam generation mechanisms, including snap-off, lamella-division, and leave-behind, and two basic mechanisms of foam destruction, *i.e.*, capillary-suction coalescence and gas diffusion have been identified through the microscopic studies of foam using micromodels. Kovscek et al. (1995), who gave a detailed review on foam pore-scale events, stated that snap-off and capillary-suction coalescence are the two dominant mechanisms, especially under conditions of coinjection of surfactant solution and gas.

For the snap-off mechanism that is schematically shown in Figure 2.1, Chambers and Radke (1991) observed three varieties, namely pre-neck snap-off, Roof snap-off, and rectilinear snap-off that occur depending upon local liquid saturation change and pore-body geometry. Kovscek et al. (2007)'s recent micromodel experiment confirmed Roof snap-off as a dominant, repeated event for foam generation at steady state. Their experiments were conducted under conditions of constant injection rates of aqueous foamer solution and nitrogen as well as constant outlet pressure. They found that snap-off occurs over the range of $0.890 < f_g < 0.993$ in a variety of pores within the micromodel that are smoothly constricted and exhibit dimensionless constriction sizes of roughly 0.30 or less. A series of microscopic images of foam recorded by Kovscek et al. showed that snap-off occurs over and over again at steady state within the same germination site. In addition, the authors stated that the frequency of division events is quite small in comparison to the frequency of snap off events.

Capillary-suction mechanism is illustrated in Figure 2.2 that shows the thickness evolution of a lamella translating through a periodically constricted tube and occurring of coalescence. As supported by a large body of experimental evidence,

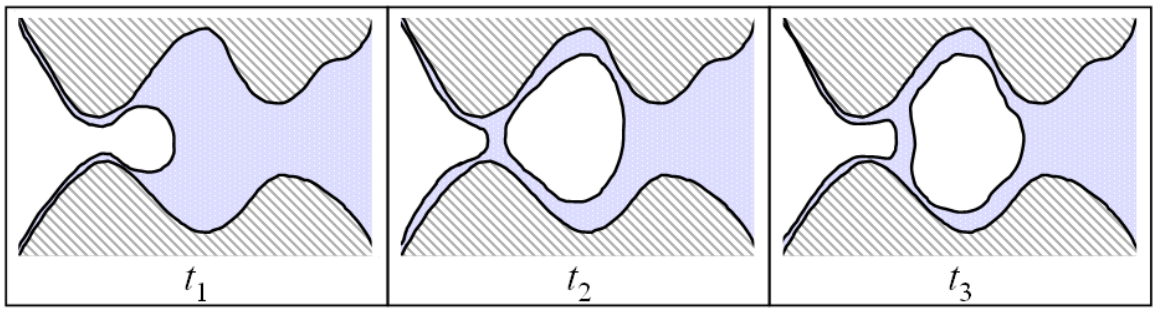

Figure 2.1: Schematic of snap-off mechanism (Kovscek and Radke, 1994).

capillary-suction coalescence is strongly affected by a so-called limiting capillary pressure. Khatib et al. (1988) first directly measured capillary pressures in their glass-bead packs during steady foam flow and observed a drastic foam coarsening at a specific capillary pressure. Jimenez and Radke (1989) observed a catastrophic collapse of an 80% quality foam upon transferring from a wet upstream micromodel to an identical attached dry micromodel. The foam coalescence was attributed to the significant difference in the capillary pressure between the two micromodels. Limiting capillary pressure is a function of local phase saturations and surfactant formulation in liquid phase and represents foam stability. Jimenez and Radke (1989) proposed a simple hydrodynamic stability theory that correctly explains the gas velocity dependency of the limiting capillary pressure measured by Khatib et al. (1988).

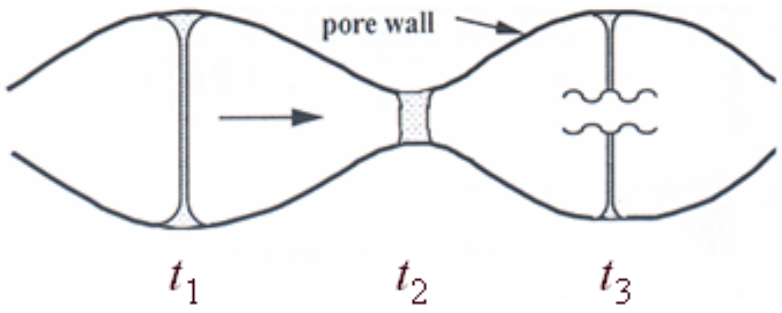

Figure 2.2: Schematic of capillary-suction coalescence mechanism (Kovscek and Radke, 1994).

Core-flooding experiments were also employed by several researchers to examine the foam texture and mobility for real field conditions. Using a visual cell, Martinez (1996) measured foam texture of the effluent phase from the core in different experiments. He found that the foam texture is much finer and stabler in low foam quality corefloods than in high foam quality ones. His observations were consistent with the finding of Ettinger and Radke (1992) who measured effluent mean bubble density and size distribution of foams generated with and without a foam generator. Friedmann and Jensen (1986) studied foam propagation during transient foam flow by injecting gas (nitrogen) at a constant rate in a Berea sandstone previously saturated with surfactant. By analyzing the resulting pressure drop variations, the authors concluded that foams propagate like a sharp foam front with gas bank ahead. The pressure drop and gas saturation evolution showed that steady state was reached rapidly in short core section, except for at the inlet section after the passage of the foam front. This result was in agreement with findings of several other investigators (Kovscek et al., 1995).

2.2.2 Foam Modeling Theories

Based on the documented laboratory observations, a variety of theoretical models have been developed to model foam flow through porous media. These models rely on the fact that foam texture determines the strength and mobility of foam and that foam texture itself depends on many factors, such as pore structure, surfactant formulation, permeability, capillary pressure, flow rates, presence of nonwetting phase, etc. Therefore, most of the models modify gas mobility according to the presence of foam. The existing theoretical models range from empirical and semiempirical models (Fisher et al., 1990; Mohammadi et al., 1993; Patzek and Myhill, 1989), to fractional-flow theory (Zeilinger et al., 1995; Zhou and Rossen, 1995), to percolation models (Chou, 1990; Rossen and Gauglitz, 1990), and to population-balance models (Chang

et al., 1990; Fergui et al., 1995; Friedmann et al., 1991; Kovscek et al., 1995; Patzek, 1988).

Empirical Correlation Method

As its name suggests, this method accounts for the presence of foamed gas by modifying either relative permeability of the porous medium to gas or gas viscosity, or both according to an empirical function of key factors. Marfoe et al. (1987), for instance, developed a one-dimensional foam model in which the mobility reduction of foamed gas is incorporated via modification of the gas viscosity. Their formula of gas viscosity in the presence of foam takes into account surfactant concentration, the amount of water available for foaming and gas velocity. Islam and Ali (1990) expanded this model by incorporating the dependency of gas viscosity on oil saturation, reservoir matrix heterogeneity, and pressure gradient. Following a similar logic, many other expressions with more sophisticated correlations and more variables have been proposed for the mobility reduction of foamed gas. In general, the parameters in those empirical models have to be determined from experimental or field data, and, thus, are problem-dependent.

Fractional Flow Method

Zhou and Rossen (1995) developed a model of foam displacement by applying fractional flow theory. In this method, the basic mathematical principles of the Buckely-Leverett displacement were retained through describing foam flow in terms of spreading or shock waves of fixed component saturation or concentration. This model was later improved by other researchers by introducing the concept of limiting capillary pressure (Hill and Rossen, 1994; Zeilinger et al., 1995). Because of problematic assumptions made in the theory, including fluid incompressibility, no chemical reaction

between rock and fluids, and an immediate attainment of local steady-state mobilities, the fractional flow methods generally provide qualitative rather than quantitative predictions of foam displacement.

Percolation Network Method

In the percolation network method, a random spatial distribution of connected flow paths of different conductivity, called a network, is adopted to represent a porous medium and certain microscopic event or mechanism is incorporated to network percolation for mimicking foam flow. For example, Rossen and Wang (1997) used a capillary-bundle as the pore network with assumption of foam flow behaving like a Bingham plastic to model lower quality foams. Cohen et al. (1997) successfully employed a pore network model to predict the portion of trapped foam under a given pressure gradient and given pore size distribution. In general, percolation approaches provide good qualitative prediction; however, they may require intensive computations and be constrained to achieve generality by their assumptions.

Population Balance Method

Compared with the aforementioned foam models, the population balance model is the most comprehensive. In the population balance approach, the number of foam bubbles per unit volume of gas, so-called foam texture, is tracked and the population of bubbles is used to compute gas mobility. The theoretical development of this approach is described in detail by Patzek (1988). Several investigators have successfully applied the volume averaged bubble population equation to describe laboratory experiments. For example, Kovscek et al. (1995) implemented the population balance equation in a reservoir simulator and compared the numerical results with their coreflood experiments. Kovscek et al. (1997) also modeled the foam flow in a heterogeneous porous medium. Myers and Radke (2000) extended the approach to three-phase flow

and studied the effect of residual oil on foam evolution.

The population-balance model presented by Kovscek et al. (1995), however, was formulated to describe the high-quality or so-called limiting capillary pressure regime (Khatib et al., 1988) that is thought to be characteristic of continuous vapor and surfactant solution injection during steam drive enhanced oil recovery. Early studies (de Vries and Wit, 1990; Osterloh and Jante, 1992) indicate flow regimes that depend on foam quality and other factors. The experiments of Osterloh and Jante (1992) teach that the pressure drops generated by high quality foams are sensibly independent of the gas superficial velocity and increase linearly with liquid injection rate, whereas the pressure drop generated by low quality foams is independent of liquid superficial velocity but increases with gas injection rate. A series of subsequent papers established generality of the phenomenon including Parlar et al. (1995), Vassenden and Holt (1998), Alvarez et al. (2001), and Kim et al. (2005). Additionally, Kovscek et al. (1995) found similar, quality-dependent pressure drop trends for foam flow experiments through fractures. The difference between high and low quality results was related visually and mathematically to the microstructure of foam bubbles within the fracture.

Modification of the description of net foam generation in the model of Kovscek et al. (1995) is needed to make this population-balance model applicable to the low-quality regime and, thus, more general. Secondly, the requirement of an additional equation for foam texture evolution adds complexity to the implementation of the population-balance model, and also increases the computational cost of simulation runs. Hatziavramidis et al. (1995) proposed a simplified model that accounts for the relative permeability of the gas for weak foam and includes additionally the effective gas viscosity for strong foam. Bertin et al. (1998) proposed a simplified approach to the full population balance model. They calculated foam texture using a bubble-population correlation that is expressed as a function of porosity, permeability, gas

saturation, the limiting capillary pressure for foam coalescence, and the flowing foam fraction. These existing simplified approaches are important first steps, but seem to lack generality. On the other hand, the local equilibrium approximation of the population balance approach has been applied to steady state (*e.g.*, Ettinger and Radke, 1992; Kam and Rossen, 2003) and transient (*e.g.*, Kam et al., 2007) foam flow. A local equilibrium population balance model holds promise of mechanistic and predictive foam flow simulation at reduced computational cost.

2.2.3 Field Applications of Foams

Practical oil field exercises with foams have been conducted over the past decades. A broad range of results from technical and economic success to abject failure have been reported in the literature. Here, we do not try to give a complete reviews but attempt to summarize important results and findings from several major field tests. More comprehensive reviews of existing foam field projects can be found elsewhere (Castanier and Brigham, 1991; Patzek, 1996; Turta and Singhal, 1998).

The improved oil recovery by the use of steam foam has been observed in many field steam-foam pilots in late 1980's. The first steam-foam test was conducted by Shell in the Mecca lease of the Kern River field and its preliminary results were presented by Dilgren et al. (1982). Later, further field results of the Mecca lease project and one additional Bishop steam-foam pilot were reported to be encouraging (Patzek and Koinis, 1990). In these two pilots, steam foam was continuously injected either at the base or full interval to achieve in-depth control of gas mobility and it is believed that steam foam propagated a significant distance into the reservoir. After the injection of foamer solution and steam, Patzek and Koinis (1990) reported dramatic improvement in vertical sweep of the reservoir as interpreted by neutron logs and temperature surveys. Major oil responses were observed after about 2 years of foam injection. The incremental oil recovery of 8.5% and 18% original oil in place

(OOIP) were reported over a five year period of steam foam injection for the Bishop pilot and Mecca pilot, respectively.

Djabbarah et al. (1990) presented the field data of a steam-foam diversion pilot operated by Mobil in the South Belridge Field. Their tracer tests and casing gas analysis indicate redistribution of steam by foam across the vertically heterogeneous oil sand and corresponding enhanced volumetric sweep and oil production. Foam injection in this pilot resulted in an incremental oil production about 183,000 barrels. The steam-foam field trial operated by Chevron in section 26C of the Midway-Sunset field was another field-scale demonstration project of steam-foam. Similarly, substantial improvements in both the vertical and areal sweep of the reservoir were reported as a result of the presence of foam in-depth (Friedmann et al., 1994).

Recently, Blaker et al. (2002) reported the foam-assisted water alternating gas project (FAWAG project) in the offshore Snorre field, the North Sea. The main target for FAWAG was the Upper Statfjord zone that has permeability ranging from 400 to 3,500 md. Four sequences of foamer solution injection took place with surfactant concentrations from 0.4 to 0.7 wt%. During conventional WAG operations, breakthrough of injection gas occurs between 40 and 60 days after the start of gas injection and the breakthrough time deceases as more WAG cycles occur. It is estimated that 65 to 100% of the injected gas is eventually produced. By adopting the FAWAG approach, significantly less injection gas is produced with an average back production of injection gas of only 33%. The producing GOR is substantially lowered compared to pre-foam tests and tracer data indicated significantly delayed gas breakthrough.

Chapter 3

Effect of Heterogeneity on SAGD

Heterogeneity is an intrinsic aspect of any reservoir, resulting from its complex sedimentary geologic origin, tectonic evolution, and erosion through millions of years. Often observed in oil fields are shales, fractures (naturally or artificially induced), and faults that easily cause one or even several orders of magnitude variation in formation properties, such as permeability. For SAGD, the presence of reservoir heterogeneity, depending upon its extent, may influence steam chamber development significantly, and thus has considerable impact on the effectiveness and economics of the process.

This chapter focuses on reservoir heterogeneity caused by randomly-distributed shale barriers and reports a numerical investigation of the effects of such heterogeneity on SAGD performance. The chapter begins with an analysis of characteristic length of flows associated with the steam chamber development in a typical SAGD process. According to the unique shape of the steam chamber, we identify two flow regions in which the characteristic length of fluid flow is different. A simulation model of a synthetic Athabasca-type reservoir is then detailed with the descriptions of the reservoir parameters, the numerical grid system, and the shale distribution. Properties are generated using a stochastic representation based on a geostatistical model. After

that, simulation results are presented to illustrate the effects of reservoir heterogeneity on oil production, recovery, and efficiency in the SAGD process. Discussions follow on the difference in the effects of heterogeneity within the two identified regions.

3.1 Feature of the SAGD Process

Figure 3.1 shows the common implementation of SAGD with two horizontal wells. The view is a vertical cross section. In practice, the SAGD process is normally initiated with a preheating period to overcome the difficulty of steam injection due to extremely unfavorable mobility ratio (Saltuklaroglu et al., 2000). During the preheating period, steam is circulated in the tubing and out of the annulus for both horizontal wells, thus heating the surrounding oil by conduction. Once thermal communication is established between wells and the oil in the inter-well region becomes mobile, steam is injected into the reservoir to develop a chamber above the wells. An idealized steam chamber in a homogeneous reservoir is shown schematically in Figure 3.1. The development of this inverse-triangularly-shaped steam chamber involves complicated steam condensate flows and thermal processes. Injected steam rises within the chamber under buoyancy forces and flows continuously to the perimeter of the chamber, where it condenses and releases a large amount of latent heat. The heat is transferred, by both conduction and convection, first to the condensate that flows inside the steam chamber, and then the adjoining oil (Farouq-Ali, 1997; Ito and Suzuki, 1999). The mobilized oil and the condensate drain by gravity along the steam chamber toward the production well. As the oil is removed and more steam is injected, the boundary of the steam chamber expands upwards and sideways. Butler's gravity drainage theory, as shown in Eq. (2.1), indicates that steam chamber growth is necessary for oil production and that the rate of drainage is a function of the vertical height and (homogeneous) permeability of the steam chamber.

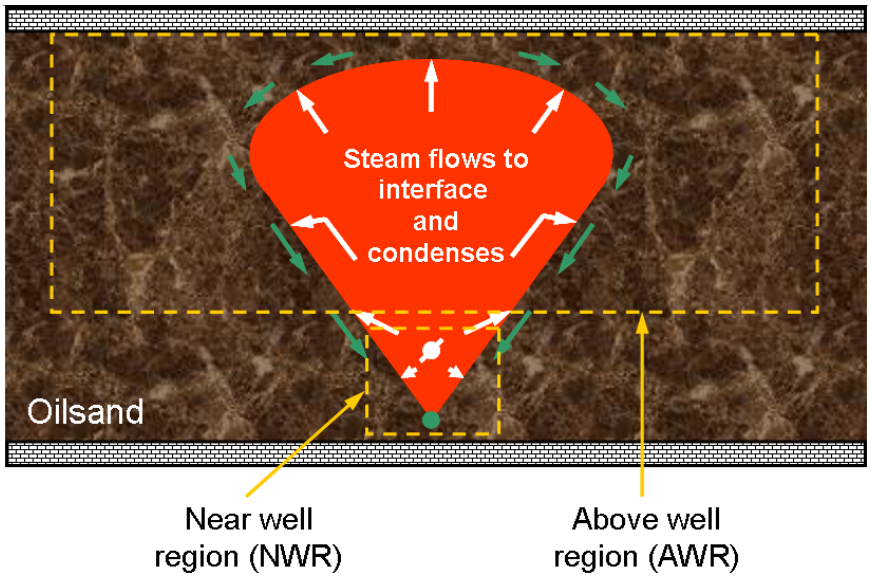

Figure 3.1: Schematic steam chamber growth in a SAGD process. Boxes drawn with dashed lines indicate the near well region (NWR) and the above well region (AWR).

Consider a heterogeneous reservoir that contains randomly distributed shale barriers. The development of a steam chamber is affected to some extent and the ideal steam chamber shown in Figure 3.1 does not form. Because of the unique well arrangement and gravity driving mechanism, the steam chamber is expected to attain the inverse triangular shape during its development, although it will be distorted. The drainage path of hot oil and condensate is still along the slopes of the steam chamber. One analogy to such a drainage path is the fluid flow along the surface of a funnel.

The triangular shape and orientation of the steam chamber result in different characteristic lengths. In the upper part of the chamber, the heated volume is large, and the steam flow inside and hot oil drainage around the chamber propagates in relatively long and wide paths. The flows in this region are of relatively long characteristic length, *e.g.*, half of the formation height.

On the other hand, in the bottom of the steam chamber, all the flows are limited to

the small region around the well. Accordingly, the characteristic length of steam and oil flows is relatively short. Recall that the gravity drainage theory indicates that the success of a SAGD process depends on the balance between a rising steam chamber and draining hot fluids. The effects of reservoir heterogeneity on steam rising and oil drainage are not the same throughout the formation because of the difference in the characteristics of the flows in different regions. This observation leads to the definition of two regions, the near well region (NWR) and the above well region (AWR). Each region is indicated in Figure 3.1 by dashed-lines. As demonstrated later, identification of the NWR and AWR makes it possible to decouple the complex effects of reservoir heterogeneities on the SAGD process.

3.2 Reservoir Simulation Model

3.2.1 Description of the Synthetic Reservoir

A synthetic reservoir representing a generic formation in the Alberta oil sands (Western Canada) is selected. Detailed reservoir properties are listed in Table 3.1. The reservoir is 300 m deep with a pay zone thickness of 20 m. Initial oil and water saturations in the pay zone are 0.8 and 0.2, respectively, and reservoir temperature is 50 °F. The reservoir formation consists of clean sands and shaly sands that contain laterally-orientated thin shale. The absolute permeability of the clean sands is 3.0 D (μm^2) in the horizontal direction and 1.8 D (μm^2) in the vertical direction. The representation of shale in the model is detailed in the next subsection. Both clean sands and shaly sands have a porosity of 32%.

According to typical properties of Athabasca bitumen, a four-pseudocomponent model is used to represent the oil in reservoir. Figure 3.2 depicts the viscosity of oil mixture as a function of temperature. Figure 3.3 presents the water-oil and gas-oil

Table 3.1: Reservoir properties.

Reservoir depth	300 m	Reference depth	315 m
Reservoir thickness	20 m	Initial pressure	420 psi
Porosity	0.32	Initial temperature	50°F
Horizontal permeability	3.0 D	Initial S_o	0.80
Vertical permeability	1.8 D	Initial S_w	0.2
Oil viscosity (RC)	1,000,000 cp	Oil density (RC)	8.8 °API

relative permeability curves adopted in this work. The Stone II model is used to calculate relative permeabilities for three-phase flow (Stone, 1973). More details of the simulation model parameters are provided in the example STARS input file for SAGD simulation included in Appendix A.

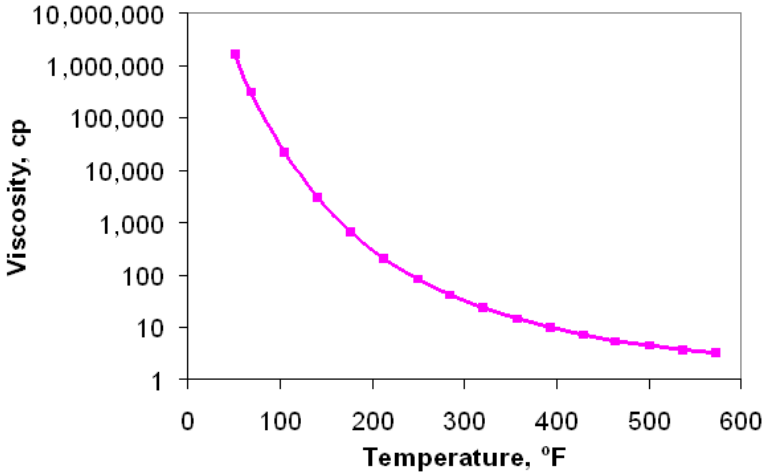

Figure 3.2: Oil viscosity versus temperature.

3.2.2 Numerical Grid System

A SAGD project generally includes a series of parallel well pairs spreading through the formation, as shown schematically in Figure 3.4. The horizontal spacing between well pairs varies from 75 m to 150 m in practice. In this study, with the assumption

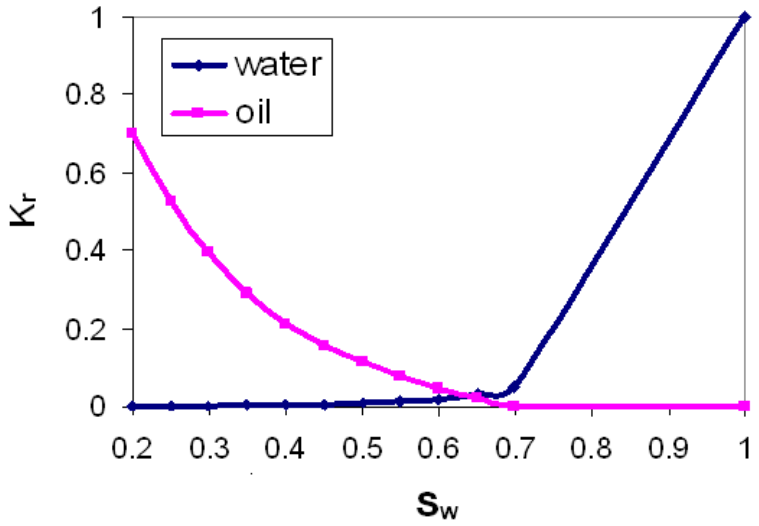

(a)

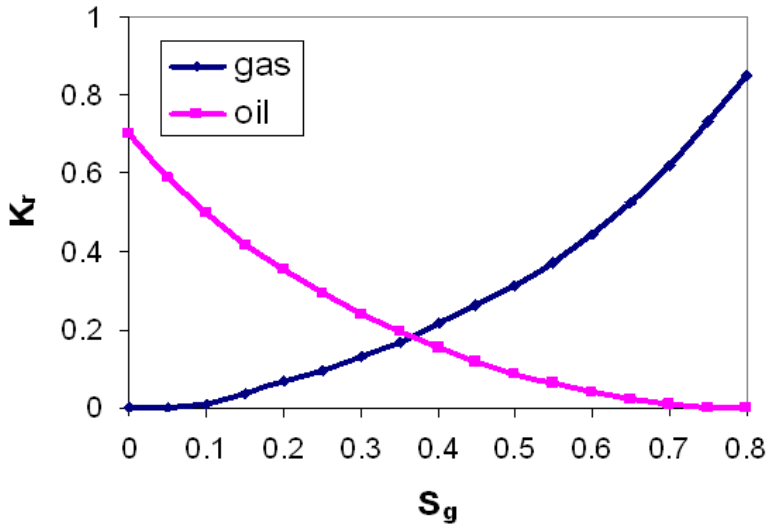

(b)

Figure 3.3: Rock and fluid properties: (a) water-oil and (b) gas-oil relative permeability curves.

of symmetry between well pairs, we consider a confined formation unit with one well pair in the center. A horizontal well spacing of 100 m is chosen accordingly. The well pair consists of two horizontal wells with lengths of 1,000 m. One well acts as a producer and the other as an injector. The production well is placed 1.5 m above the bottom of the pay zone and the injection well is drilled parallel to the producer with a vertical well spacing of 4 m. The vertical well spacing chosen here falls into the lower end of the practical range that ranges from 4 to 10 m.

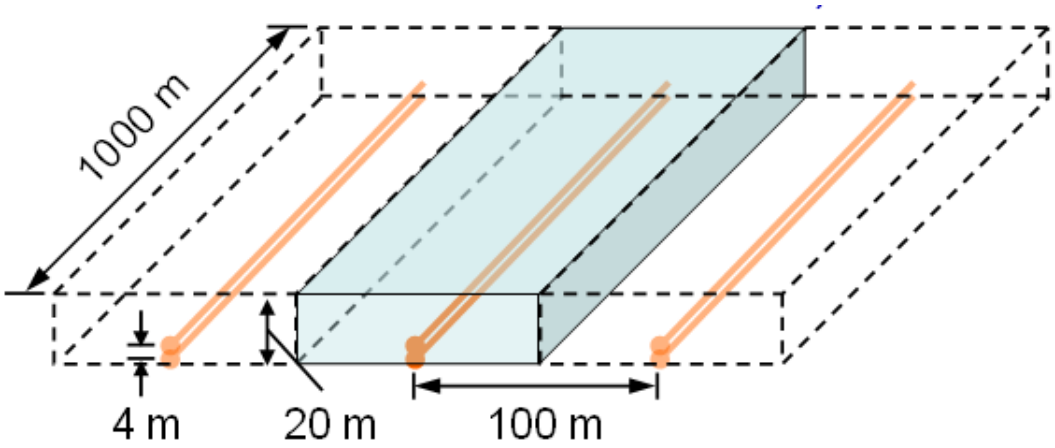

Figure 3.4: Schematic of parallel well pairs employed in practical SAGD projects. The center gray block indicates a confined unit considered in our simulation model with assumption of symmetry between well pairs.

Figure 3.5 shows the two-dimensional grid system used for the reservoir simulation. The two-dimensional domain represents a vertical reservoir cross section perpendicular to the wells. This grid contains 67 grid blocks in the x-direction, and 20 grid blocks in the z-direction. The cells are 1.5 m wide and 1.0 m high, except for the center column in which the cells are 1.0 m $\times$ 1.0 m. The choice of the 1.0 m wide block in the center is simply to make the total width of the blocks add to 100 m. Our sensitivity analysis shows that such a choice of one smaller grid block in the center gives identical results to the case with the uniform grid system of the same block size. Also, this grid size in the vertical cross section was found to be sufficiently fine to

resolve complex flows occurring in the vertical plane. The effects of grid size and the grid are examined in the Appendix A.

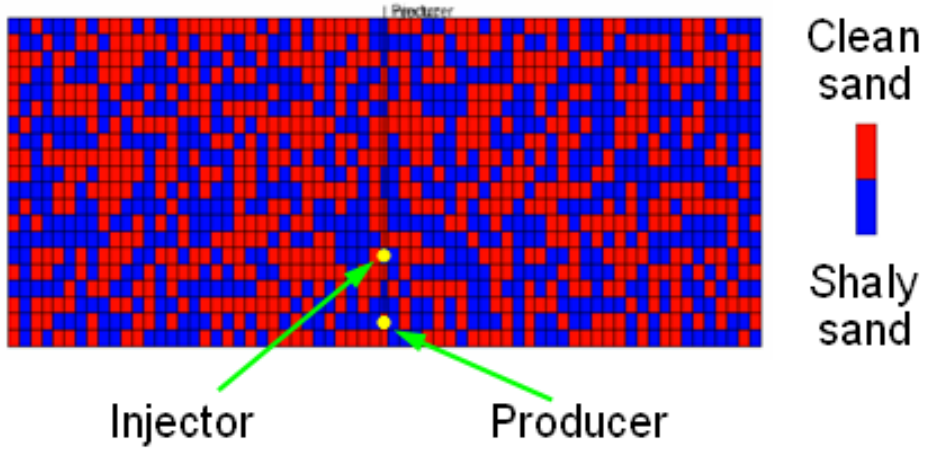

Figure 3.5: Two-dimensional numerical grids for SAGD simulation runs. The blue and red grid blocks indicate shaly sand and clean sand, respectively. The distribution of the shaly sand and clean sand grid blocks is generated by SISIM with 30% shale content and 1.5 m shale correlation length.

3.2.3 Shale Distribution

As reviewed in Chapter 2, due to the limitation of the experiments or simplification made in the numerical models, previous researchers studied reservoir heterogeneities by simply including a limited number of shale barriers at designed locations. Considering the intrinsic geological nature of shale observed in fields, one better representation of shale distribution is the stochastic model based on geostatistical methods (Pooladi-Darvish and Mattar, 2002).

In this work, reservoir heterogeneity is introduced by including randomly distributed, discontinuous, thin shale lenses. The shale is characterized by low vertical permeability, typically in the range of 10^{-9} to 10^{-6} D. For laterally-oriented thin shale lenses, it is acceptable to assume that the occurrence of shale in sand reduces

dramatically the vertical permeability of the sand block, but has no effect on the horizontal permeability. Therefore, a reduction factor of 10^{-5} is applied to the vertical permeability of the shaly sand blocks in this study. As exact geological information of sand and shale sequences is not available to us, we model the distribution of shaly sands with a stochastic representation based on a geostatistical method, sequential indicator simulation (SISIM) (Goovaerts, 1997). In the geostatistical model, the probability of the shaly-sand occurrence (P_s) and correlation length of shale (L_s) are the two key parameters that determine the fraction of shaly sands and the continuity of shale in the distribution, respectively. These two characteristics of shale distribution, as demonstrated later, play important roles in the SAGD process. For each pair of P_s and L_s, SISIM generates a number of realizations, all honoring the predetermined data (*e.g.*, hard data) and, thus all realizations are equally probable. Figure 3.5 shows one of the realizations obtained with $P_s = 30\%$ and $L_s = 1.5$ m.

3.2.4 Simulation Runs

The thermal and compositional simulator, STARS, developed by the Computer Modeling Group (CMG) was used for all simulation runs. The simulation runs are classified into two groups: (1) varying NWR and (2) varying AWR. For the baseline simulation runs, electrical preheating is first carried out at both well locations for 90 days to mobilize the oil around the wells and to establish hydraulic communication between them. Then, 95% quality steam at 3,000 kPa (*i.e.*, 104 kPa greater than the initial pay zone pressure) is injected continuously at the upper well. The lower production well is operated using steam trap conditions to avoid excessive steam production. This steam trap control is achieved in the simulation by setting the production temperature 18 °F below the steam temperature to establish a definite liquid leg above the producer (Edmunds et al., 1994; Egermann et al., 2001). The

simulation runs are terminated after 10 years of injection. The CPU times for two-dimensional (67×20 grid blocks) simulations of a 10-year production on a Dell server (dual 2.8 GHz processors, 3.75 GB RAM) are 15 minutes approximately.

3.3 Results and Discussion

Next, steam chamber development and oil production are examined in the heterogeneous system. The role of shale barriers in the region immediately around the injection well is examined first.

3.3.1 Near Well Region — NWR

The extent of the NWR is chosen appropriately if a consistent SAGD performance is obtained for a number of equal-probability realizations (equally probable to occur) with a similar fraction of shaly sand (P_s) and shale continuity (L_s). These results are presented in two dimensions for ease of visualization and discussion.

Figure 3.6(a) illustrates three choices of NWR size, labeled small ($D_v \times 1.5D_v$), medium ($3D_v \times 1.5D_v$) and large ($6D_v \times 1.5D_v$) with respect to the vertical well spacing (D_v). For each case, three equal-probability realizations are generated. First, a random distribution of shaly sands is created and used as synthetic hard data. The fraction of shaly sands is 30% and shale correlation length is 1.5 m. The volume defined by a NWR size in this synthetic realization is then used as hard conditioning data to generate three realizations of shaly sand distribution. As a result, the three realizations in each case share the exact same configuration in the NWR, but have different AWR with the same fraction of shaly sand and shale continuity.

Reservoir simulation runs were conducted with the three equal-probability realizations for each NWR size. Figure 3.6(b)–(d) compare SAGD performance in terms of oil production rate, oil recovery versus cumulative steam injection, and cumulative

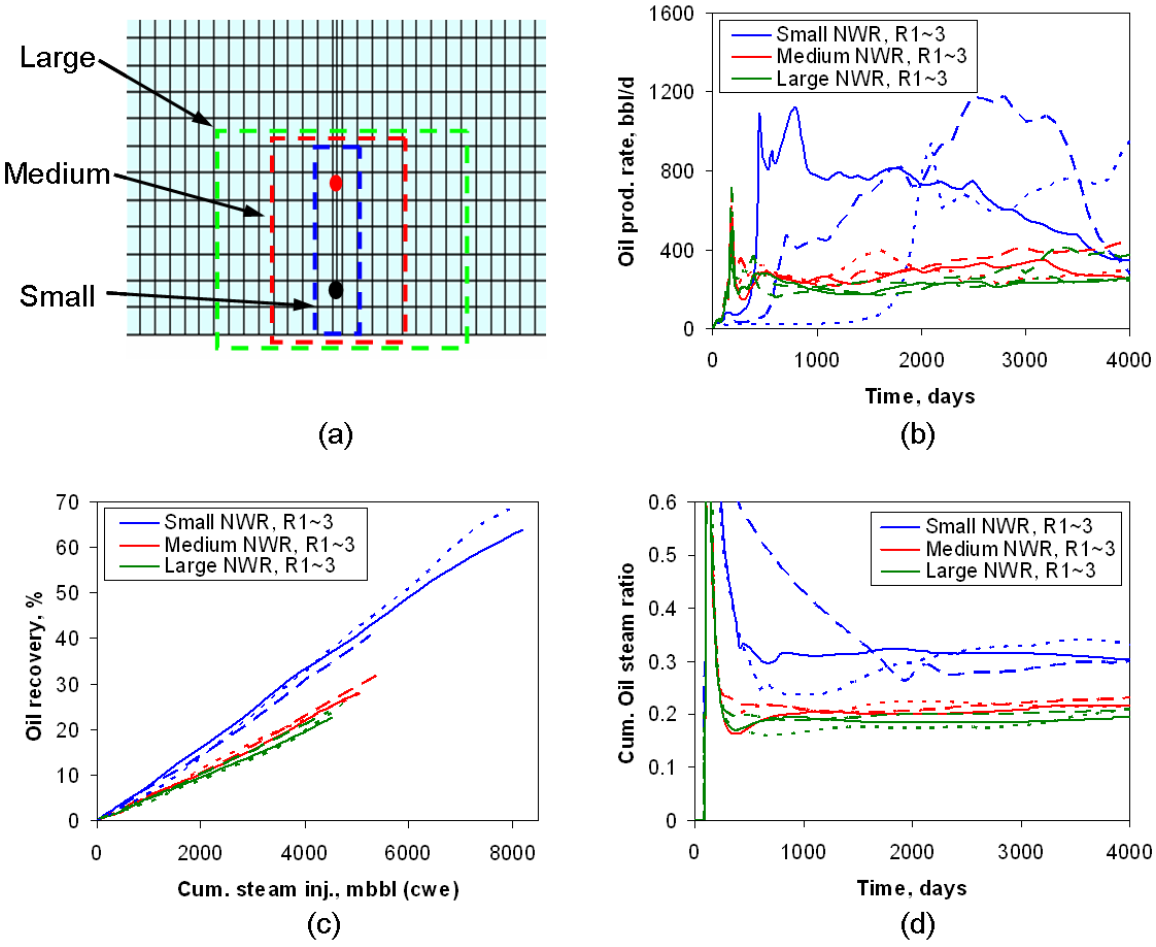

Figure 3.6: Comparison of NWR sizes: (a) definition of three sizes, (b) oil production rate, (c) oil recovery versus cumulative steam injection, and (d) cumulative oil-steam ratio.

oil-steam ratio for the three sets of realizations. In all the figures, three types of curves (solid, dashed, and dotted) in the same color represent the three realizations for the same NWR size. As seen in the figures, the curves in blue corresponding to the case of small NWR size exhibit considerable variations between realizations. For instance, for the case of small NWR size, the startup time of oil production in Figure 3.6(b) varies from 300 days to 1,900 days, and the oil recovery after 10 years of operation differs from 40% to 70%. In contrast, the curves in green and red, for the medium and large NWR sizes, respectively, show consistent results between realizations. This comparison suggests that the medium size of the NWR ($2D_v$ by $1.5D_v$ where D_v is the vertical well spacing) is likely to be the appropriate definition of NWR size for this particular reservoir setting.

This result is intuitive. The NWR affects the SAGD process mainly by influencing the drainage flow of hot fluids (water and oil) along the steam chamber boundary in the bottom portion of the chamber (Figure 3.1). Because the angle of the chamber wall with respect to the horizontal plane changes gradually as the steam chamber expands, it is reasonable to assume an average value of 45 ° for the qualitative analysis based on previous visualization of physical model experiments (Butler, 1998b) and simulation results. A rectangular region is determined with the angle to be $2D_v$ by $1D_v$ that covers fully the bottom part of steam chamber. This leads to a NWR size corresponding to the case of the medium NWR size in Figure 3.6(a).

After determining the correct NWR size, we investigate the effect of the NWR on SAGD performance. Figure 3.7(a) shows two configurations of a medium-sized NWR. Two random realizations with 30% shale occurrence and correlation length of 1.5 m were used to select the NWR. The SAGD performance with three realizations conditioned to each fixed NWR are illustrated in Figure 3.7(b)–(d). Note that the three realizations share the same configuration in the NWR, but have different AWR with the same fraction of shaly sand and shale continuity. The result of the equivalent

homogeneous model with a vertical permeability of 0.467 D calculated using a flow-based upscaling method (Wen et al., 2003) is also included in Figure 3.7(b)–(d) as a reference.

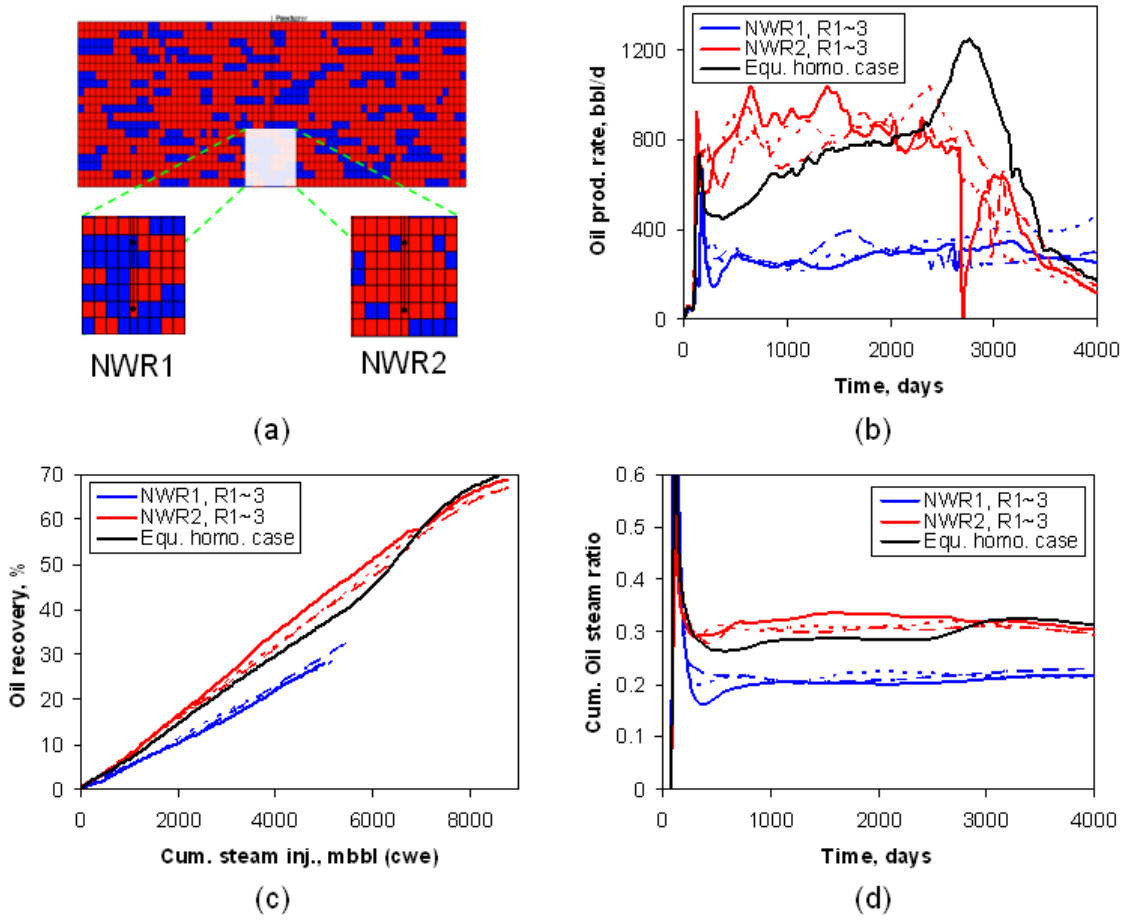

Figure 3.7: Comparison of SAGD performance between two shaly-sand distributions in the NWR: (a) NWR1 and NWR2, (b) oil production rate, (c) oil recovery versus cumulative steam injection, and (d) cumulative oil-steam ratio. The equivalent homogeneous case shown by the solid black line is included as a reference.

As expected, the curves in the same color that represent the cases with the same NWR collapse together with acceptable variance. This confirms that the determined NWR size is appropriate. Secondly, two sets of curves, in red and blue, as illustrated

in Figure 3.7(b)–(d), reveal dramatic differences in SAGD performance between realizations that have different shaly-sand configurations in the NWR. For the case of NWR1, all three realizations yield an average oil production rate of about 300 bbl/d. This rate is less than half the oil production rate of NWR2, which is 800 bbl/d. Similar results are observed in the comparisons of oil recovery and cumulative oil steam ratio.

This large discrepancy is mainly attributed to the manner in which the permeability distribution in the NWR affects the steam chamber development. Effectively removing heated oil and condensate from the reservoir is necessary for continuous steam injection and thus successful steam chamber expansion. Hot fluids must pass through the NWR before being produced. Therefore, a NWR with substantial vertical and horizontal connectivity facilitates fluid drainage thereby aiding steam chamber development. If the NWR contains shale barriers that impede vertical flow, the drainage path of hot oil may be blocked in the NWR. Moreover, because of the relatively short characteristic length of flows in the NWR, the drainage flow is sensitive to the distribution of shale barriers in the NWR, especially when the shale continuity is increased. The above analysis is easily verified by visual comparison of NWR1 and NWR2 in Figure 3.7(a). The comparison of SAGD performance between the cases of NWR1 and NWR2 suggests that in practice horizontal well pairs should be placed in the high quality region (less shale) of the formation to optimize SAGD performance.

3.3.2 Above Well Region — AWR

Two sets of simulation runs were conducted to investigate the effect of the shale percentage and shale continuity in the AWR. In the first set, the fraction of shaly sands is fixed at 30%, and the shale correlation length is varied as 1.5 m, to 6 m, 12 m, and 24 m. In the second set, the shale correlation length is fixed at 6 m, and the fraction of shaly sands is changed from 10% to 30% and 50%. All permeability

realizations are conditioned to the same predetermined NWR data (NWR2 shown in Figure 3.7(a)).

Figure 3.8 compares the effect of shale continuity in the AWR on SAGD performance. Again, for reference purpose, the equivalent homogeneous cases are presented by dashed lines in Figure 3.8. For each case of the shale correlation length, reservoir simulation runs were conducted with three realizations. As their responses are consistent, only one is plotted in the figure. The figure shows that oil production is strongly correlated to the shale continuity. The oil production rate curve for the more continuous shale, for example, is below that for the shale with shorter correlation length.

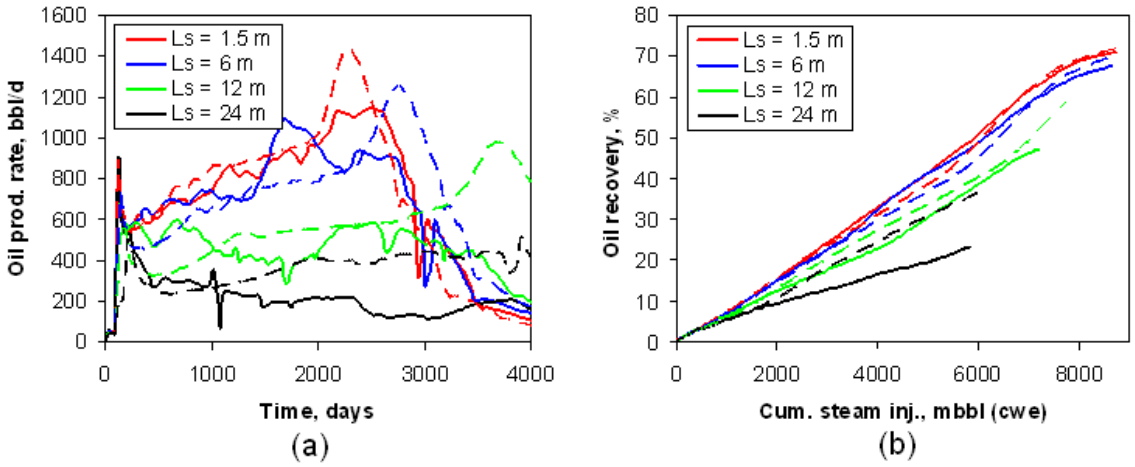

Figure 3.8: Effect of correlation length of shaly-sand in AWR on SAGD performance: (a) oil production rate and (b) oil recovery versus cumulative steam injection. The dashed lines in the figures present the results of the equivalent homogeneous cases whose permeabilities are obtained from the corresponding cases (in the same color) using a flow-based upscaling method (Wen et al., 2003). The equivalent vertical permeabilities are 0.615, 0.467, 0.310, and 0.203 D as the shale length increases.

As the shale becomes more continuous, from 1.5 m to 24 m, the oil recovery factor decreases from 70% to 23% after 10 years of injection, and the cumulative oil steam ratio reduces from 0.3 to 0.15. Notice that this decreasing trend is not

uniform. For changes in shale continuity from 1.5 m to 6 m, the resulting difference in SAGD performance is not obvious, but when the shale correlation length is significant, they cause dramatic reduction in oil production. This is because the steam chamber expansion mainly occurs in the AWR. The flows associated with the steam chamber expansion are of relatively long characteristic flow length depending on the steam chamber height. As a result, the horizontal barrier formed by shale can only affect the steam chamber development when it is greater than about 12 m. Otherwise, steam easily bypasses the discontinuous shale and extends the chamber further into the cold zones.

These observations are corroborated by the temperature profiles. The critical shale length that effectively limits the steam chamber growth is observed to be about half of the formation thickness. Such results confirm our analysis of the flow characteristic length in the AWR.

When the fraction of shaly sand increases, we observe a similar reduction trend in SAGD performance, as presented in Figure 3.9. Note that the dashed lines in Figure 3.9 represent the results of the equivalent homogeneous cases. The case with 10% shale gives the greatest oil production rate as well as the best oil recovery factor. Note that there is a sharp fluctuation in the oil production rate at 3,000 days for the 10% shale case. This is likely attributed to the steam trap control that triggers an increase in the producer BHP at 3,000 days to avoid steam breakthrough. There is a small reduction in oil production when the shale percentage is increased by 20%, whereas another 20% increase in shale percentage results in a substantial reduction in oil production, *i.e.*, approximately 60% decrease in both the average oil production rate and oil recovery factor. As the shale percentage increases, the shaly sand blocks form a more continuous barrier to the vertical flow, that, in turn, limits the development of the steam chamber.

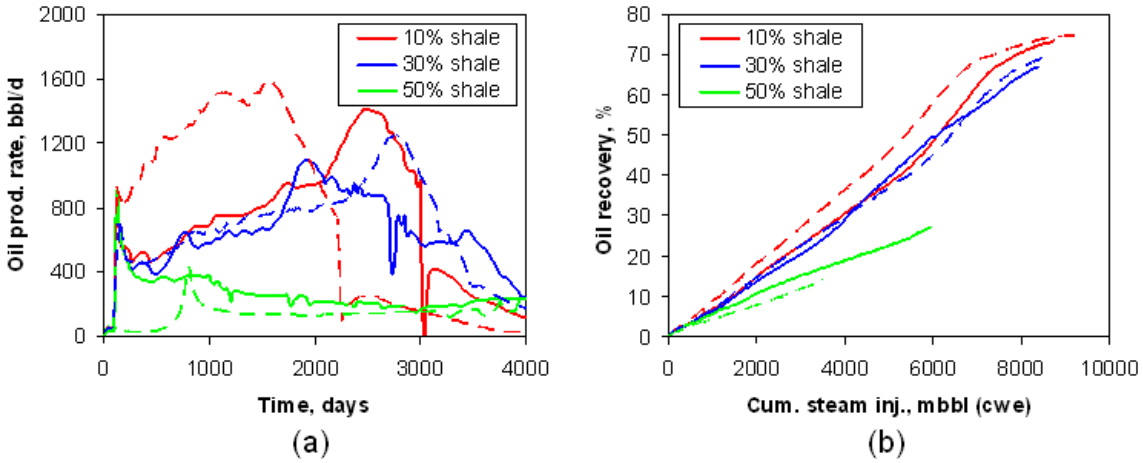

Figure 3.9: Effect of shaly-sand percentage in AWR on SAGD performance: (a) oil production rate and (b) oil recovery versus cumulative steam injection. The vertical permeabilities of the equivalent homogeneous cases denoted by dashed lines are 1.148, 0.467, and 0.091 D as the shale percentage increases.

3.4 Concluding Remarks

In this chapter we presented a numerical study of reservoir heterogeneity effects on the SAGD process using a stochastic model of shale distribution and a thermal numerical reservoir simulator. The complex effect of reservoir heterogeneity on the SAGD process is decoupled by identifying two flow regions: the near well region (NWR) and the above well region (AWR). The drainage and flow of hot fluids within the NWR are of short characteristic length and found to be very sensitive to the presence and distribution of shale. Based on this observation, we suggest placing horizontal well pairs in the high quality region of the formation to optimize SAGD performance. On the other hand, the AWR affects the (vertical and horizontal) expansion of the steam chamber that is of characteristic flow length on the order of half of the formation height. SAGD performance is affected adversely only when the AWR contains long, continuous shale or a high fraction of shale.

It is also shown clearly in our simulation results that SAGD operations yield low

or moderate oil production rate and recovery in reservoirs with poor vertical communication due to the presence of a high percentage of shale or continuous shales. Applications of conventional SAGD to such reservoirs that are quite common in reality would be problematic from the economical perspective. This raises an urgent question as to how we may improve SAGD performance for reservoirs with unfavorable heterogeneity. The following chapters attempt to provide potential solutions to this question.

Chapter 4

Hydraulic Fracturing in SAGD

A successful SAGD operation normally requires a high-quality, homogeneous reservoir. In reality, commonly existing shales that typically extend laterally throughout the formation impair the vertical permeability resulting in poor vertical communication in the reservoir. As presented in Chapter 3, in such reservoirs SAGD fails to produce bitumen efficiently and economically because of the limited steam chamber growth. We propose hydraulic fracturing as a potential method to enhance SAGD performance in those reservoirs. In this chapter, we first discuss the possible orientation of fractures induced hydraulically. Simulations are conducted for a synthetic reservoir with a good deal of shale. The effects of hydraulic fractures, including horizontal and vertical orientations, are contrasted by comparing the resulting oil production and oil-steam ratio from two-dimensional and three-dimensional simulations. At the end, we comment on the feasibility of hydraulic fracturing in oil sand in terms of practical operations and other concerns.

4.1 Orientation of Hydraulic Fractures

Hydraulically-induced fractures always propagate perpendicular to the least principal stress (Hubbert and Willis, 1957). Therefore, to determine the orientation of hydraulic fractures, the tectonic stresses in a reservoir should be analyzed to obtain knowledge of the principal stresses. Figure 4.1(a) shows the orientation of the maximum horizontal stress (S_{Hmax}) in Alberta (Collins, 2005) that is one of the major heavy-oil resource areas attracting interest. The orientation of S_{Hmax} is determined from the borehole breakout analysis of vertical wells. A consistent NE-SW trend of the maximum horizontal stress is observed throughout the Alberta Province. Figure 4.1(b) shows the magnitudes of the three principal stresses as functions of depth. For the formations shallower than 150 m, the vertical stress corresponds to the least principal stress, hence horizontal fractures are induced. Beyond a depth of 200 m, the least principal stress changes to the minimum horizontal stress leading to vertical fractures.

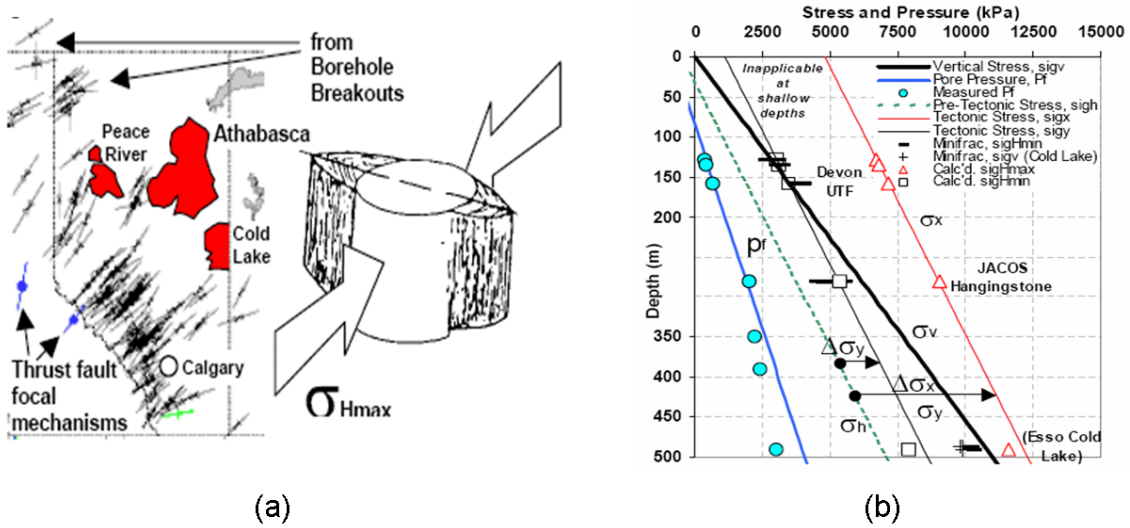

Figure 4.1: In-situ stresses in Alberta oil sand: (a) maximum horizontal stress orientation and (b) stress magnitudes versus depth (Collins, 2005).

Consequently, we consider two categories of SAGD projects according to the formation depth: shallow SAGD and deep SAGD. In a shallow SAGD project, the least principal stress corresponds to the overburden stress. Once a fracture is induced hydraulically, the dominant orientation of the fracture plane is horizontal (Figure 4.2(a)). For deep SAGD projects, the reservoirs have a minimum horizontal stress corresponding to the least principal stress. The dominant orientation of the induced fracture plane is vertical. In addition, depending on the drilling direction of the horizontal well pairs in a SAGD process, a vertical fracture can be parallel or perpendicular to the wells (Figure 4.2(b) and Figure 4.2(c)). In the following subsection, we examine the effects of the fractures with these three different orientations on the SAGD process by reservoir simulation.

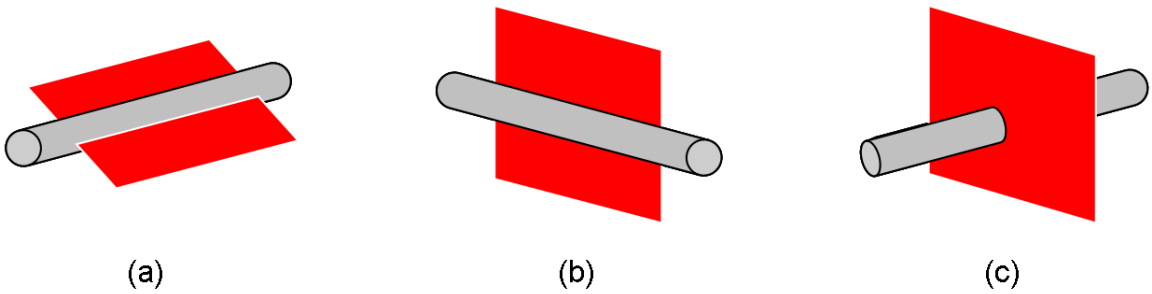

Figure 4.2: Schematic of possible orientations of hydraulic fractures: (a) horizontal fracture, (b) vertical fracture parallel to the well direction, and (c) vertical fracture perpendicular to the well direction.

4.2 Reservoir Simulation Model

For this study, we use the same reservoir simulation model as described in Chapter 3. In addition to the two-dimensional grid system, as shown in Figure 3.5, a three-dimensional model (Figure 4.3) is specially designed to compare the effect of fractures. To achieve sufficient spatial resolution in all three dimensions while limiting the total

number of grid blocks for reasonable machine run time, nonuniform grids of 37 by 37 by 20 are adopted to simulate the synthetic reservoir with 1/10 of its original length. The grid block widths and lengths vary gradually from 0.5 to 3.5 m, while the thickness remains constant at 1 m.

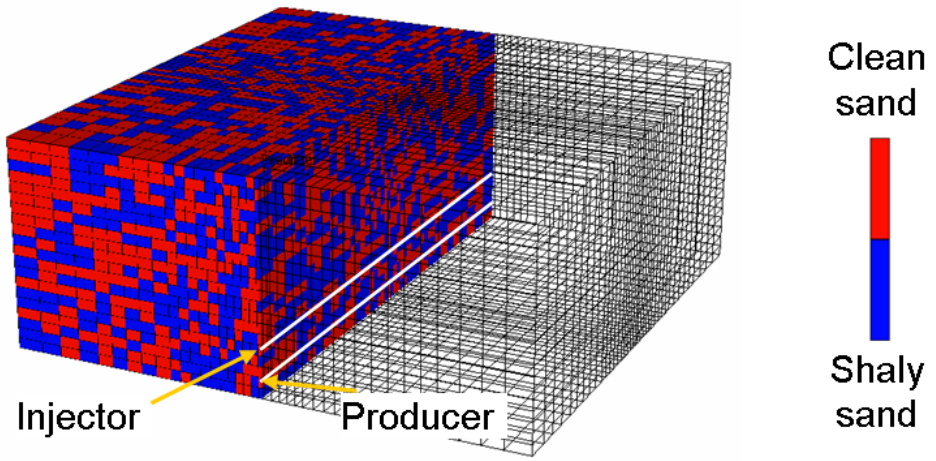

Figure 4.3: Three-dimensional numerical grids for SAGD simulation runs. The blue and red grid blocks indicate shaly sand and clean sand, respectively. The distribution of the shaly sand and clean sand grid blocks is generated by SISIM with 30% shale content and 1.5 m shale correlation length.

4.2.1 Representation of Fracture

Besides shale barriers, another common case of reservoir heterogeneity is the presence of fractures, either naturally-existing or hydraulically-induced. Fractures have substantial permeability and very small pore volume. In this study, we only consider hydraulic fractures. The effect of a hydraulic fracture on petrophysical properties of the grid block where it is located is approximated as follows. A fracture permeability of 10^3 D and aperture of 0.01 m are assumed. The absolute permeability in the direction perpendicular to the fracture plane remains identical to the case without a fracture. For the directions parallel to the fracture plane, the permeability of the

grid block is changed to the equivalent permeability computed by arithmetic averaging according to fracture and block geometries. In the two-dimensional model, for example, the 1.0 m by 1.0 m clean sand blocks in the center column containing the vertical fracture have an effective vertical permeability of 11.782 D, while the shaly sand blocks have an effective vertical permeability of 10.0 D.

4.3 Results and Discussion

4.3.1 Two-Dimensional Study

Figure 4.4 compares the SAGD performances with four shale/fracture configurations. The four cases share the same shale distribution that has 50% shale and shale correlation length of 1.5 m. The fracture orientations and lengths are illustrated in Figure 4.5. The horizontal fractures are 28 m long and the vertical fractures penetrate through the whole pay zone, *i.e.*, 20 m long. Note that the injector and producer are penetrated by the same hydraulic fracture in the third case. This puts great reliance on steam trap control to limit short-circuiting of steam from the injector to the producer as well as steam intrusion into the producer. Therefore, in the fourth case, the injector is shifted slightly (4 m horizontally apart) so that it does not lie in the same vertical plane as the producer. It is believed that this completion technique provides further assurance that steam is injected deep into the reservoir.

As shown in Figure 4.4, the oil production rate of the base case (red curve) is low and then experiences a jump at about 700 days that leads to the main production period. The oil production rate, after reaching a peak, drops back to 300 bbl/d, and remains at a plateau rate with a slow decline for the rest of production time. The final oil recovery is only 21% and the cumulative oil steam ratio is 0.2. For the case with horizontal fractures, the oil production rate curve (in blue) shows a similar shape as

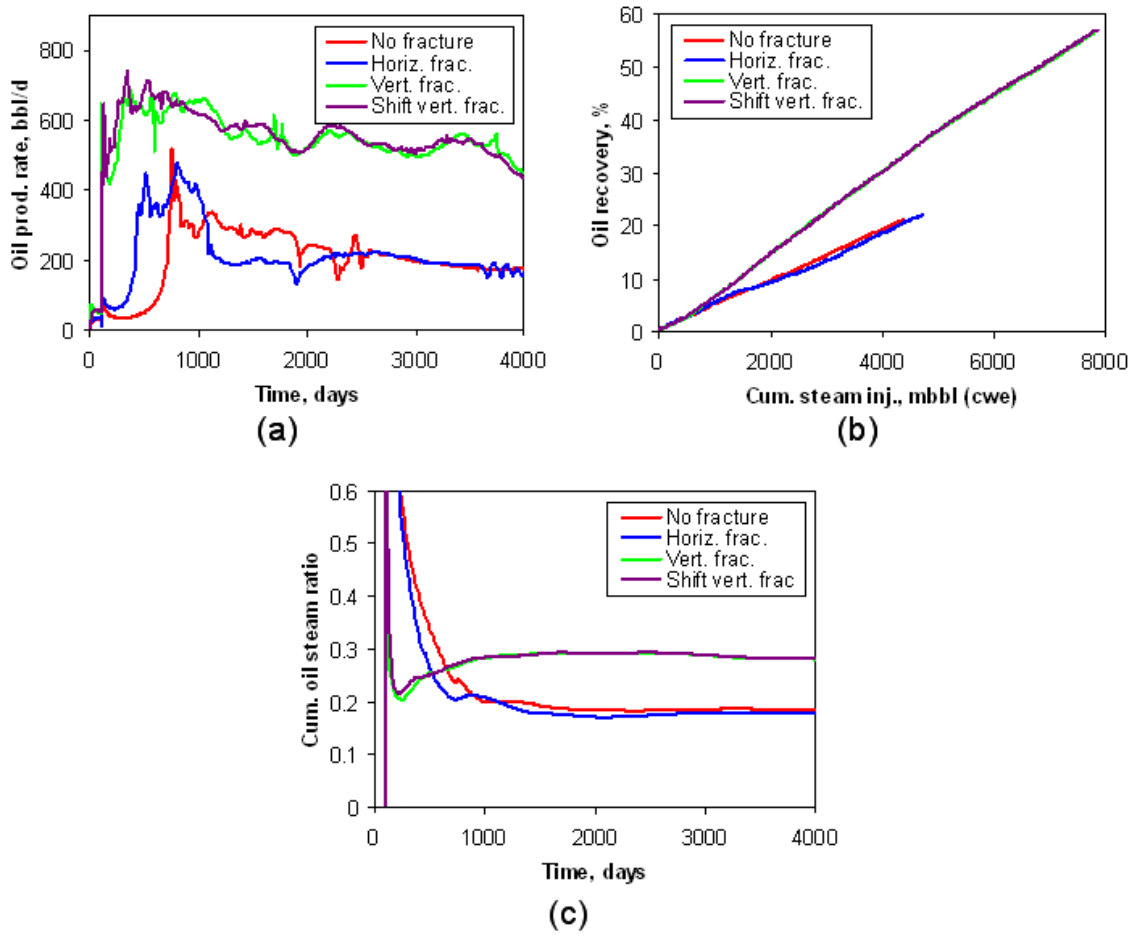

Figure 4.4: Comparison of no fracture, horizontal fractures, and vertical fractures: (a) oil production rate, (b) oil recovery versus cumulative steam injection, and (c) cumulative oil-steam ratio.

the base case except that the main production period occurs approximately 300 days earlier. The two cases with a vertical fracture show similar performance. The main oil production period in both cases starts shortly after steam injection and exhibits an average oil rate more than twice the oil rates of the other two cases.

As seen in Figure 4.4(b), the base case yields an oil recovery of only 21% after 4,500 Mbbl ($\times 10^3$ bbl) CWE steam injection. Adding horizontal fractures increases the oil recovery to 24%, while the presence of the vertical fracture, with the injector and producer aligned or slightly shifted, improves the oil recovery dramatically, up to 56%.

The observed effects of horizontal and vertical fractures are explained by examining how the steam chamber profile is affected by the presence of fractures. Figure 4.5 shows the temperature profiles in the vertical cross section of the formation after 3 years of steam injection. Because the shaly sands have low vertical permeability, the steam chamber in the base case develops very little in the formation after 3 years of steam injection. The horizontal fractures (Figure 4.5(b)) help the steam chamber extend laterally in the region near the wells because of better inter-well communication, thus causing an earlier main production period than the base case. Limited improvement, however, is observed in the vertical direction for steam chamber growth. The steam chamber in the cases with vertical fractures (Figure 4.5(c) and (d)) is developed fully through the whole thickness of the formation. The vertical fracture provides a highly permeable vertical path for steam that substantially improves the vertical development of the steam chamber. Recall that steam trap control helps to limit steam breakthrough.

According to Eq. (2.1), the oil drainage rate is proportional to the square root of the chamber height. Hence, the improvement in the vertical development of the steam chamber accelerates oil drainage, and consequently the performance of SAGD is enhanced dramatically. As seen in Figure 4.5, the volume of the steam chamber

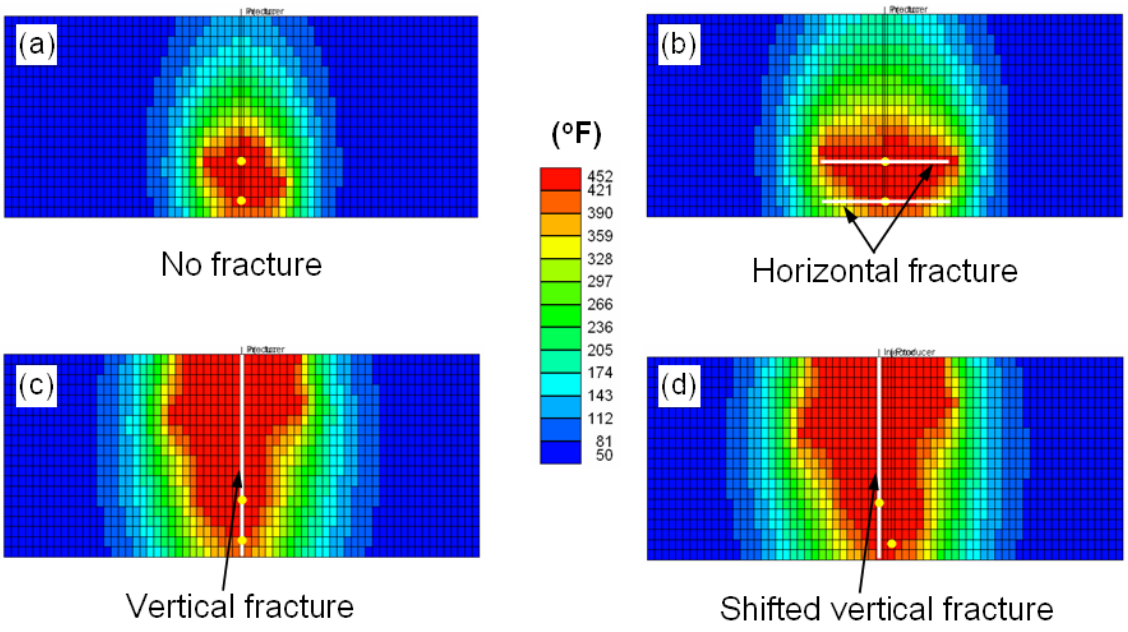

Figure 4.5: Temperature profiles after 3 years of steam injection with (a) no fracture, (b) horizontal fractures, (c) a vertical fracture, and (d) a vertical fracture in the offset-well configuration.

with a vertical fracture is much larger than the case with no or horizontal fractures.

The vertical fractures considered here are parallel to the well axis. According to the argument in the previous section, another possible orientation is perpendicular to the well axis if the well is drilled along the direction of the minimum horizontal stress. The effects of these two situations are investigated with the three-dimensional grid system and compared to a base case with no fractures.

4.3.2 Three-Dimensional Study

Figure 4.6 compares the predicted oil production for the three cases. Figure 4.6(a) shows that the case with the vertical fracture along the wells gives an oil production rate more than twice that of the base case. It is interesting that with a vertical fracture perpendicular to the well, the oil production begins with a rate less than that of the base case and then accelerates and exceeds the latter in the later stages. This is a result of the steam trap control that was implemented to avoid direct steam production. The vertical fracture perpendicular to the well creates a very permeable channel between the two wells at the perpendicular intersection plane. This actually increases the heterogeneity contrast along the wells. To avoid steam breakthrough, the steam trap control has to set a low steam injection rate at the beginning because of a high injectivity contrast along the well. As a result, the oil production rate is low in the early stages. When the steam chamber develops around the wells, the injectivity contrast along the well is smoothed out and then steam is injected at the reservoir's full capability in the later stages. Because the vertical fracture, as demonstrated in the two-dimensional model, aids the vertical development of the steam chamber, the oil production shows an increase at later time. Figure 4.6(b) shows that the oil recovery factors after 10 years of steam injection are 23%, 29%, and 45% for the three cases, respectively.

Figure 4.7 presents the steam chamber profiles after 6 years of steam injection

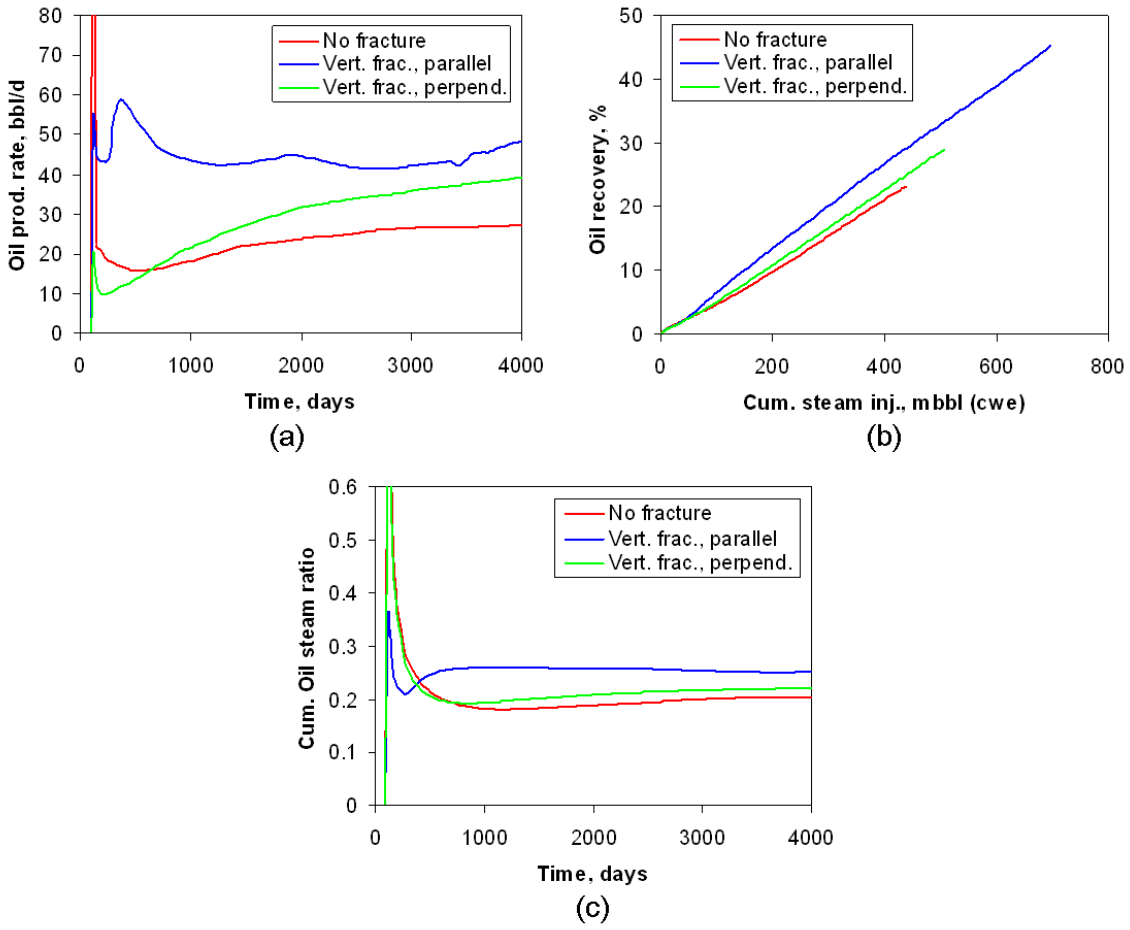

Figure 4.6: Comparison of formation with/without vertical fractures: (a) oil production rate, (b) oil recovery versus cumulative steam injection, and (c) cumulative oil-steam ratio.

in the three cases. The case with a vertical fracture along the well (Figure 4.7(b)) develops a steam chamber that is large and nearly symmetrical. A large volume of the oil sand is swept by steam. For the case with a vertical fracture perpendicular to the well (Figure 4.7(c)), steam extends along the fracture plane to the top of the formation and forms a nice chamber. As shown, the well-developed steam chamber is limited to the region near the fracture plane. In the regions far from the fracture around the two ends of well, the development of the steam chamber is relatively poor. This means that the improvement in production brought by the vertical fracture perpendicular to the well direction is moderate. Note that this result is obtained with the assumption of one vertical fracture perpendicular to the well within the interval of interest. It is possible to induce hydraulically multiple fractures, which likely results in a more successful steam chamber development along the whole length of the well.

These simulation results suggest that vertical fractures enhance the SAGD process. One of the challenges of such an idea is the feasibility of generating the desired vertical fractures in the field. To achieve vertical fractures propagating along the well, it is required that the horizontal wells be drilled along the direction of the maximum horizontal stress (S_{Hmax}). This requirement, fortunately, coincides with the general field practice that horizontal wells are normally drilled exactly in this fashion to ensure well stability. If the well stability is not an issue (*e.g.*, strong rock) for a particular reservoir, drilling wells along the direction of the minimum horizontal stress (S_{hmin}) and creating a series of vertical fractures perpendicular to the well direction may indeed provide an effective way to enhance the performance of the SAGD process in a shaly reservoir.

Effective steam trap control presents another challenge in the field operation of SAGD with hydraulically-induced fractures. In addition to the off-set well configuration described in the previous subsection, injection of foamed steam provides a potential method to overcome live steam production. Steam foam in porous media

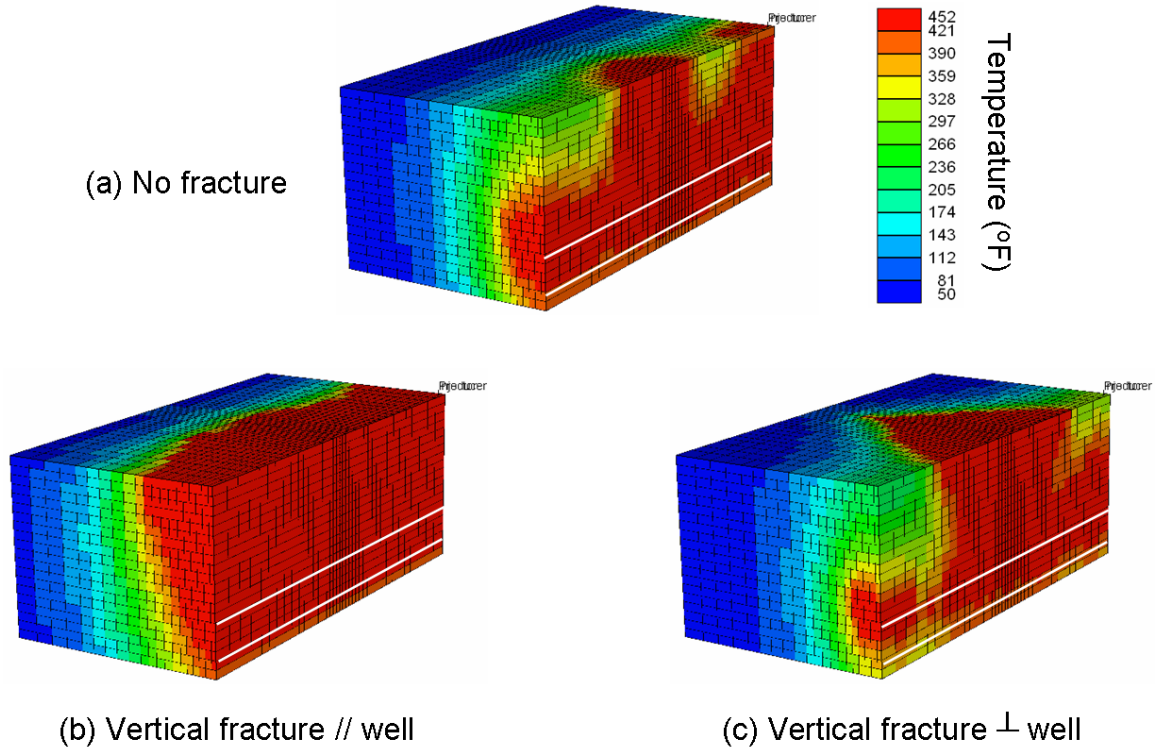

Figure 4.7: Temperature profiles after 6 years of steam injection with (a) no fracture, (b) a vertical fracture parallel to the well direction, and (c) a vertical fracture perpendicular to the well direction.

causes significant flow resistance due to foam trapping and non-Newtonian flow behavior (Kovscek and Radke, 1994; Patzek, 1996), and, therefore, can be used to block the interwell region. The related research on foam modeling and foam application to SAGD are presented in Chapters 5 and 6, respectively.

4.4 Concluding Remarks

Hydraulic fracturing improves steam injectivity dramatically to achieve an economical oil production rate in a SAGD process for reservoirs with poor vertical communication. The orientation of hydraulic fractures generally depends on the depth of the formation. Fractures are usually horizontal for shallow SAGD projects and vertical for deep SAGD projects. It is shown that a vertical hydraulic fracture enhances SAGD performance considerably and thus hydraulic fracturing may be desirable for deep SAGD projects. It is also found that a vertical hydraulic fracture along the well direction is superior to a direction perpendicular to the well direction. The field practice that a horizontal well is drilled along the direction of the maximum horizontal stress to ensure well stability coincides with the requirement of vertical hydraulic fractures parallel to the well direction. Moreover, for the case of vertical fractures along the well direction, we propose a modified well configuration with injectors and producers off-set laterally at a short distance to mitigate the difficulty in operations for steam trap control while maintaining effective oil production.

Chapter 5

Foam in Porous Media

As discussed, the presence of intrinsic heterogeneity introduces many difficulties to the practical operation of conventional SAGD and impairs process performance dramatically. In addition to hydraulic fracturing, we propose the use of foam in combination with steam injection during SAGD to improve the process efficiency for a heterogenous reservoir. To evaluate the proposed concept of Foam-Assisted SAGD, a suitable numerical model for foam was incorporated into a multidimensional, fully featured reservoir simulator to obtain a comprehensive investigation from a numerical perspective. This chapter presents the development of a simplified population-balance foam model based on the local-equilibrium approximation. We first give a brief introduction to foam flow through porous media at the microscopic scale to illustrate foam mechanisms. A framework of the population balance approach is then described, followed by the derivation of the local-equilibrium model. Details of experiments used for model verification are provided. Then we present and discuss four main results. First, predictions of steady state foam behaviors from foam models with a modified snap-off generation model are examined for both low- and high-quality foam regimes. Second, experimental measurements of a foam texture profile at steady state are presented to verify the assumption of local-equilibrium. Third, experimental data and

theoretical predictions from full physics and local equilibrium models are compared quantitatively for two types of one-dimensional, linear transient foam flows, one with constant surfactant and the other with transient surfactant transport. Finally, the applicability of the local equilibrium model is tested with a one-dimensional, radial foam flow at the field scale.

5.1 Theory of Foam Models

Foam is a dispersion of a gas within a continuous liquid. It reduces gas mobility dramatically. For instance, when compared to gas that is not foamed, foam lowers gas mobility by factors as great as 5,000. To understand foamed gas mobility control and to model foam behaviors accurately, it is necessary to consider foam characteristics within the pores of rocks.

5.1.1 Schematic of Foam Flow at Pore-Scale

Figure 5.1 illustrates a simplified schematic of two-phase foam flow in porous media at the pore scale (Chambers and Radke, 1991; Ettinger and Radke, 1992; Kovscek and Radke, 1994). In the figure, cross-hatched circles represent water-wet sand grains, whereas the dotted area refers to wetting surfactant solution. Unshaded and darkly shaded bubbles designate flowing and trapped (stationary) foam bubbles, respectively.

Because of capillary forces, the smallest pore spaces are occupied by wetting liquid that forms wetting films on the surface of sand grains. The continuous wetting films assure continuity of the aqueous, wetting phase throughout the pore structure. Consequently, wetting-phase relative permeability is insensitive to the presence of foam. Flowing foam bubbles are generated by snap off or mobilization and division of liquid lenses and lamellae, whereas stationary bubbles are created by a so-called leave behind mechanism as well as by stationary bubbles that cease to flow (Ransohoff and

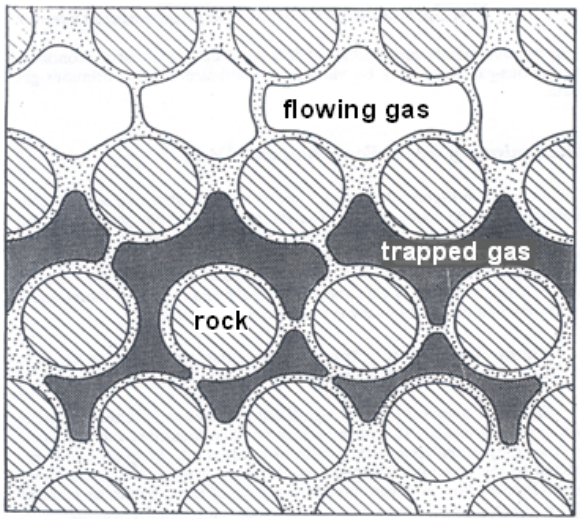

Figure 5.1: Schematic of foam flow in porous media (Courtesy of Kovscek and Radke, 1994).

Radke, 1988). The largest pore spaces, as shown in the upper part of the figure, are occupied by flowing foam bubbles that transport as bubble trains together with lamellae through porous media. The flowing bubble trains encounter drag because of the presence of pore walls and constrictions, and because the gas-liquid interfacial area of a flowing foam bubble is constantly being rearranged by viscous and capillary forces. This non-Newtonian effect of foam flow increases the effective viscosity of the gas-phase, thereby reducing the gas mobility. Significant bubble trapping occurs in the intermediate-sized pores, as indicated in the middle of Figure 5.1. In effect, the stationary bubbles block the intermediate-sized pores that would otherwise carry gas flow. According to published gas tracer studies (Friedmann et al., 1991; Gillis and Radke, 1990; Tang and Kovscek, 2006), the fraction of gas trapped within a foam at steady state in sandstones ranges from about 85 to 99%. The large gas blockage reduces the relative permeability of gas phase significantly and lowers gas mobility further.

As reviewed in Chapter 2, a variety of theoretical models have been developed

to model foam flow in porous media based on documented laboratory observations. Among all these foam models, the population-balance method is the most comprehensive and addresses directly the evolution of foam texture and, in turn, reduction in gas mobility. The theoretical underpinnings of this approach are described in detail by Patzek (1988). The population balance approach provides a framework for expressing all the relevant physics of foam generation, coalescence and transport.

5.1.2 Full Physics Model

We choose the population-balance method for our studies because of its generality and similarity to the traditional mass and energy balance equations for flow in porous media. To distinguish the comprehensive model with full physics from the simplified model described in the next subsection, we refer to the former as the full physics model (FPM). For illustrative purposes, the transient balance on the mean foam bubble size in the full physics model is written in one dimension as:

$$\frac{\partial}{\partial t}[\phi(S_f n_f + S_t n_t)] + \frac{\partial}{\partial x}(u_f n_f) = \phi S_g (k_1 |v_w||v_f|^{\frac{1}{3}} - k_{-1}|v_f| n_f) + Q_b \quad , \qquad (5.1)$$

where t is time, ϕ is porosity, S is the phase saturation, n is bubble concentration (bubbles per unit volume of gas), u is Darcy velocity, v is the interstitial velocity, k is the rate coefficient, and Q_b is a source/sink term for bubbles. The subscript f refers to flowing foam, t to trapped foam, g to the gas phase, w to the aqueous phase, 1 to foam generation, and -1 to foam coalescence. On the left of Eq. (5.1) are the accumulation and flux terms of foam bubbles, respectively. The first term on the right of Eq. (5.1) is the net rate of foam generation. Most foam population balance models, to date, have differed significantly in their representation of foam generation and destruction mechanisms and the mathematical representation of net foam generation (*e.g.*, Falls et al., 1988; Friedmann et al., 1991; Kam and Rossen, 2003; Kovscek et al., 1995).

For example, Friedmann et al. (1991) incorporate a minimum pressure gradient for foam generation via a critical gas velocity condition.

The expression for the net rate of foam generation used here is based on snap-off and capillary suction coalescence (Kovscek and Radke, 1994). The interstitial velocities in the expression are local vector quantities that depend on pressure gradient and the local phase saturation. The liquid velocity dependency arises from the net imposed liquid flow through pores occupied by both gas and liquid, whereas the gas velocity dependency arises from the time for a newly formed lens to exit a pore.

Foam texture arises from a balance between foam generation and destruction mechanisms. The generation rate constant, k_1, reflects the number of active foam germination sites. An active germination site is determined by factors including pore topology, availability of wetting liquid, and pore space that is free of preexisting bubbles (Chambers and Radke, 1991; Kovscek and Radke, 1996). A pore needs to be sufficiently constricted, as gauged by the pore throat to body aspect ratio, to present a site where enough liquid may accumulate into an unstable configuration that "snaps off" into a liquid lens that spans the pore space (Kovscek and Radke, 1996). As the aqueous-phase saturation of pore space decreases, snap off only occurs in pores with progressively smaller constriction ratios because only these more tightly constricted pores accumulate enough liquid for snap off (Kovscek and Radke, 2003). Consequently, fewer active foam germination sites are found as the porous medium becomes drier. Additionally, an active snap off site must be free of preexisting pore-sized gas bubbles (Kovscek and Radke, 1996; Kovscek et al., 2007; Ransohoff et al., 1987). Ransohoff et al. (1987) show that mobile bubbles with volumes significantly greater than the volume of a pore are subject to snap off into progressively smaller bubbles. When pore-sized bubbles occupy a potential foam germination site, foam generation is inhibited. Hence, as stable finely-textured foam is generated, the number of foam germination sites with the proper combination of topology and fluid

occupancy decreases.

In most transient laboratory experiments that have been modeled to date, strong coalescence forces, as described next, modify foam texture before foam generation is impacted. Hence, Kovscek and Radke (1994) did not make explicit the limiting role of preexisting bubbles on foam generation sites. A foam generation constant, k_1, applicable to both the high and low quality foam regimes is written as,

$$k_1 = k_1^0 \left[1 - \left(\frac{n_f}{n^*} \right)^{\omega} \right] \quad , \tag{5.2}$$

where ω is a constant determining the shape of inverse proportionality of foam germination sites to preexisting gas bubbles and n^* is an upper limit for the concentration of foam bubbles that is related to pore size. It is found from our sensitivity studies (see Appendix B) that the predictions of the foam model are insensitive to the value of ω for the range of $\frac{1}{2}$ to 3. Equation (5.2) reflects fewer foam germination sites as bubble texture increases. More than one foam bubble per pore is not expected (Bertin et al., 1998) and the one bubble per pore limit sets n^* in simulations to follow. Additionally, the dependence of k_1 on S_w has not been needed to describe foam flow in sandstone (Kovscek et al., 1995) and is not included here.

Surfactant in the aqueous phase prevents the immediate coalescence of newly formed gas bubbles by stabilizing the gas/liquid interface. At significant capillary pressure, however, surfactant fails to stabilize the interface and foam lamellae collapse. A flowing foam lamella is vulnerable to coalescence as it flows into pore space where it is stretched rapidly and wetting liquid cannot flow into the lamella to prevent rupture (Jimenez and Radke, 1989). Accordingly, the rate of foam coalescence in Eq. (5.1) is proportional to the flux, $v_f n_f$, of foam lamellae into termination sites. The coalescence rate constant, k_{-1}, varies significantly with the local capillary pressure and surfactant

formulation as

$$k_{-1} = k_{-1}^0 \left(\frac{P_c}{P_c^* - P_c} \right)^2 \quad , \tag{5.3}$$

where the scaling factor k_{-1}^0 is taken as a constant and P_c^* is the limiting capillary pressure for foam coalescence (Khatib et al., 1988). Highly concentrated foamer solutions and robust surfactants lead to large P_c^*. Experimental investigations of various aqueous surfactants suggests the following functional form for P_c^* versus surfactant concentration (Aronson et al., 1994),

$$P_c^* = P_{c,max}^* \tanh \left(\frac{C_s}{C_s^0} \right) \quad , \tag{5.4}$$

where $P_{c,max}^*$ is a limiting value for P_c^* and C_s^0 is a reference surfactant concentration for strong net foam generation. Capillary pressure, P_c is estimated from the following form of the Leverett J-function used by Kovscek et al. (1995) for their Boise sandstone experiment

$$J(S_w) = \frac{P_c}{\sigma} \sqrt{\frac{k}{\phi}} = \left(\frac{0.022}{S_w - 0.15} \right)^{0.2} \quad , \tag{5.5}$$

where ϕ is the rock porosity, σ the surface tension of the foamer solution, and k the absolute permeability of the rock.

The convection of foam and liquid phases also must be described. For flowing foam, we replace the gas viscosity with an effective viscosity. Because flowing gas bubbles lay down thin lubricating films of aqueous fluid on pore walls, they do not exhibit Newtonian viscosity. The effective viscosity increases as texture increases, but is shear thinning at constant foam textures as (Hirasaki and Lawson, 1985)

$$\mu_f = \mu_g + \frac{\alpha n_f}{|v_f|^{\frac{1}{3}}} \quad , \tag{5.6}$$

where α is a constant of proportionality that varies with surfactant formulation and permeability. As the foam texture becomes very coarse, the gas viscosity is recovered.

Relative permeability of each phase follows as suggested by Kovscek and Radke (1994). Foamed gas mobility is treated by analogy to the Stone model of relative permeability (Stone, 1973). The relative permeability of the most wetting aqueous phase is a function of the aqueous phase saturation, whereas the relative permeability of the foamed gas is function of only the flowing gas saturation. The functionalities of standard, Corey-type two-phase relative permeability functions are retained, as follows,

$$k_{rw} = k^0_{rw} S^f_{wd} \quad , \tag{5.7}$$

and

$$k_{rf} = k^0_{rg} S^g_{fd} \quad . \tag{5.8}$$

Here, k_{ri} is the relative permeability to phase i, and the reduced saturations, S_{id} are written as

$$S_{fd} = X_f(1 - S_{wd}) \quad , \tag{5.9}$$

and

$$S_{wd} = \frac{(S_w - S_{wc})}{(1 - S_{wc})} \quad , \tag{5.10}$$

where, $X_f = S_f/S_g$ is the fraction of the foam phase that is flowing.

Obviously, the trapped gas saturation has a relative permeability of zero. The fraction of foam trapped, $X_t = 1 - X_f = S_t/S_g$, varies with pressure gradient, capillary pressure, aqueous-phase saturation, and pore geometry. Recently, Tang and Kovscek (2006) developed percolation scaling relationships to describe the trapped gas fraction as a function of foam bubble texture and pressure gradient. Nevertheless, for simplicity, we take the trapped gas fraction to be a constant here. The expression for gas trapping proposed by Tang and Kovscek (2006) is presented and discussed in Chapter 7.

5.1.3 Local Equilibrium Model

A local equilibrium approximation to the full population balance computation of n_f may be useful for large-scale calculations as the local equilibrium solution is obtained without laborious calculations. The basic idea of the local equilibrium approximation originates from the findings of previous researchers.

Friedmann and Jensen (1986) studied foam propagation during transient foam flow by injecting gas (nitrogen) at a constant rate in a Berea sandstone presaturated with surfactant solution. Ettinger and Radke (1992) measured effluent mean bubble density and size distribution of foams generated with and without a foam generator at steady state. By analyzing the resulting pressure drop variations, these authors concluded that foams propagated like a sharp foam front. More importantly, the pressure drop and gas saturation evolution showed that steady state was reached rapidly in a short core section, except for at the inlet section after the passage of the foam front. By comparing their steady-state population balance model and experimental measurements, Ettinger and Radke (1992) also concluded that local equilibrium was a good approximation for steady-state flow.

Extending the local equilibrium approximation to model transient foam flows has been attempted by many research efforts. One example is a simple foam model implemented in CMG STARS, a commercial reservoir simulator widely used in industries. That model assumes that foam creation and coalescence events occur rapidly relative to flow such that whenever gas and aqueous surfactant coexist, foam exists. It is also assumed that the presence of foam reduces the gas phase mobility by a dimensionless factor, FM. In the model, the gas mobility reduction factor, FM, due to foam is estimated by an experiment-based interpolation scheme that incorporates effects of the surfactant concentration, local gas phase velocity, and aqueous and oil phases saturations, as given by

$$FM = \left[1 + MRF \left(\frac{C_s}{C_s^{max}}\right)^{es} \left(\frac{S_o^{max} - S_o}{S_o^{max}}\right)^{eo} \left(\frac{N_c^{ref}}{N_c}\right)^{ev}\right]^{-1} \quad , \tag{5.11}$$

where C_s is the surfactant concentration in the aqueous phase, S_o is the saturation of the oil phase, N_c is the capillary number as a function of gas velocity. The maximum mobility reduction factor, MRF, is normally obtained from foam water flow experiments at maximum surfactant concentration, C_s^{max}, a reference flow rate or capillary number N_c^{ref}, and no oil in the core. The constants, es, eo, and ev are the exponents determined from experiments. Obviously, this semi-empirical option in STARS does not represent foam physics correctly. For instance, the effect of aqueous phase velocity on foam generation and coalescence as illustrated in the full physics model in the previous section is not accounted for in the above equation. Also, the nature of empirical correlation makes it less likely to predict foam behaviors correctly at various reservoir conditions.

Here, we apply the same concept of local equilibrium to the formulation of the full physics model directly and derive a more robust local equilibrium model (LEM) for the transient foam flow regime as follows. Equation (5.1) is nondimensionalized as

$$\frac{\partial}{\partial \tilde{t}}[\phi(S_f \tilde{n}_f + S_t \tilde{n}_t)] + \frac{\partial}{\partial \tilde{x}}(\tilde{u}_f \tilde{n}_f) = \phi S_g Da_{-1}(\frac{Da_1}{Da_{-1}}|\tilde{v}_w||\tilde{v}_f|^{\frac{1}{3}} - |\tilde{v}_f|\tilde{n}_f) \quad . \tag{5.12}$$

Note that the source/sink term, Q_b, is omitted as we are interested in the cases without injection of pre-generated foam. The dimensionless numbers, Da_1 and Da_{-1}, in Eq. (5.12) are Damkohler numbers that are defined as the ratio of characteristic fluid motion time scale to characteristic reaction (foam generation/coalescence) time, *i.e.*,

$$Da_1 = \frac{t_c}{t_{1,c}} = \frac{LU_c{}^{\frac{1}{3}} k_1}{n_c} \quad , \tag{5.13}$$

and

$$Da_{-1} = \frac{t_c}{t_{-1,c}} = Lk_{-1} \quad , \tag{5.14}$$

where most of the symbols have their usual definitions and the subscript c refers to characteristic value. Large Damkohler number, $Da \gg 1$, corresponds to very rapid foam generation/coalescence in comparison to transport processes. Small Damkohler number, $Da \ll 1$, corresponds to very slow foam generation/coalescence in comparison to transport processes. Parameter values in Table 5.1 and characteristic length, velocity, and bubble texture of 1 m, 1.1×10^{-5} m/s (1 m/d), and 1×10^{-11} m^{-3} (100 mm^{-3}) yield $Da_1 = 37$ and $Da_{-1} = 10$.

The dimensionless form of the population balance equation, Eq. (5.12), teaches that when $\mathrm{Da}_1, \mathrm{Da}_{-1} \gg 1$ the in-situ foam texture is dominated by local foam generation and coalescence (Ettinger and Radke, 1992). This is particularly true for applications at the field scale, as Da_1 and Da_{-1} are proportional to the length scale, L. Consequently, we set the net rate of foam generation in Eq. (5.1) to zero to place foam generation and coalescence rates in equilibrium:

$$S_g \left(k_1 |v_w| |v_f|^{\frac{1}{3}} - k_{-1} |v_f| n_f \right) = 0 \quad , \tag{5.15}$$

or

$$\frac{n_f}{1 - \left(\frac{n_f}{n^*}\right)^{\omega}} - \frac{k_1^0 v_w}{k_{-1} |v_f|^{\frac{2}{3}}} = 0 \quad . \tag{5.16}$$

Rearranging Eq. (5.16) gives

$$n_f{}^{\omega} + \frac{n^{*\omega} k_{-1} |v_f|^{\frac{2}{3}}}{k_1^0 |v_w|} n_f - n^{*\omega} = 0 \quad . \tag{5.17}$$

For $\omega = 3$, Eq. (5.17) becomes a cubic equation that is easily solved for n_f at given liquid velocity, gas velocity, and capillary pressure using standard analytical formulae (Hodgman, 1959). Note that Eq. (5.17) presents only a single real root. Stable foam

requires the presence of surfactant. Hence, a simple check is made for the presence of surfactant before solving Eq. (5.17). If no surfactant is present, the local equilibrium foam texture is set to zero.

5.1.4 Implementation of Foam Simulator

The foam models presented in this work are implemented in the framework of M^{2}NOTS (Adenekan et al., 1993). M^{2}NOTS is a compositional extension to the TOUGH2 simulator, a classic, nonisothermal simulator based on the integral finite difference method (IFDM) (Narasimhan and Witherspoon, 1976), that was originally developed in the 1990's at University of California, Berkeley for simulating the coupled transport of water, vapor, air and heat in porous media . The previous code development by Kovscek (1994) who extended M^{2}NOTS to include the transport and generation of foam in porous media is the starting point of this work.

In the current implementation, the average foam bubble density is treated as a nonchemical component of the gas phase. Thus, for the full physics model, the additional transport equation (Eq. (5.1)) is added to the standard mass balances and solved fully implicitly to predict foam behaviors with upstream weighting of the gas-phase mobility. For the local equilibrium, the simplified equation of foam texture (Eq. (5.17)) is solved explicitly as it is no longer coupled with the standard mass balance equations. For both models, foam generation and coalescence rates in each gridblock are calculated according to the magnitude of the vectors representing the interstitial gas and liquid velocities in the gridblock. The magnitude of each velocity is obtained by first summing the flow of each phase into and out of a grid block in the three orthogonal directions. Then the arithmetic average for each direction is calculated and the magnitude of the resultant vector is used for foam texture calculation. The gas velocity is similarly computed for the shear-thinning portion of the foam effective viscosity.

Appendix B provides a detailed description of the model implementation as well as the development and sensitivity studies of the local equilibrium models.

5.2 Experimentation

Coreflood experiments are designed to extend our understanding of foam behavior and verify quantitatively the applicability of the local equilibrium model for foam prediction.

5.2.1 Experimental Apparatus

Figure 5.2 shows schematically the apparatus. This setup allows simultaneous injection of gas and foamer solution as well as measurements of the flow parameters including the in-situ aqueous phase saturation, pressure drop, and textures of effluent foam bubbles.

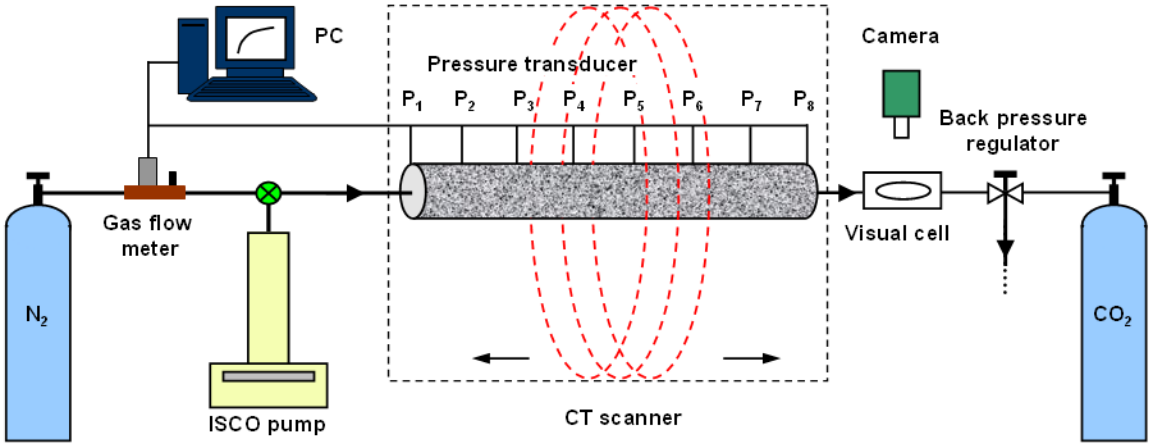

Figure 5.2: Schematic of the experimental setup for foam flow in a coreflood.

The centerpiece of the experimental setup is a 5.08 cm diameter by 60 cm long cylinder of Berea sandstone (Cleveland Quarries). The core is quite homogeneous with an average porosity of 0.18 and permeability of 0.30 D (μm^2). Figure 5.3 gives

sample CT images of air- and brine-saturated core and the porosity profile measured with an X-ray CT scanner (described shortly). Darker shading on the CT images corresponds to lower rock density. The core is placed in an aluminum sleeve and potted in place with epoxy of thickness 6.4 mm. Eleven ports are machined into the aluminum sleeve at 5.0 cm intervals for pressure measurement and foam sampling.

Injection of fluids into the core is precisely controlled by a mass flow controller (Aalborg Instrument and Controls) and a piston pump (ISCO 500D) that supply nitrogen and aqueous foamer solution, respectively. The aqueous foamer solution contains 1.0 wt% active Stepan Bioterg AOS40 (sodium C14–16 olefin sulfonate) in 0.5 wt% NaCl (J.T. Baker, Inc) brine. The injected foam quality is zero as no foam pregenerator is employed. Pressure is measured with seven differential pressure transducers (Celesco) that connect to the inlet and six pressure taps at 10 cm intervals along the core with respect to the exit pressure. The exit pressure is controlled by a dome-loaded back-pressure regulator (MityMite, Grove Valve).

A visualization cell is attached to the outlet of the core holder and upstream of the backpressure regulator for direct measurement of bubble texture of the foamed gas exiting the core. The visualization cell is made of two pieces of Plexiglas with a channel machined into one side. The small depth of the channel, 25 μm (0.001 inch) makes it possible to obtain a single layer of bubbles within the visualization cell. Back illumination is provided by a diffused, uniform light source. A digital camera records images of foam bubbles within the visualization cell versus time and the bubble texture is then obtained by image analysis.

Core characterization and in-situ measurements of aqueous phase saturation are provided by employing an X-ray CT scanner (Picker 1200SX). Figure 5.4 shows the experimental setup in the chamber of the X-ray CT scanner. The spatial resolution of such measurements is determined by voxel volume that is 0.25 mm $\times$ 0.25 mm $\times$ 3 mm, and the acquisition time of a single image is 4.5 s. During the experiment, the

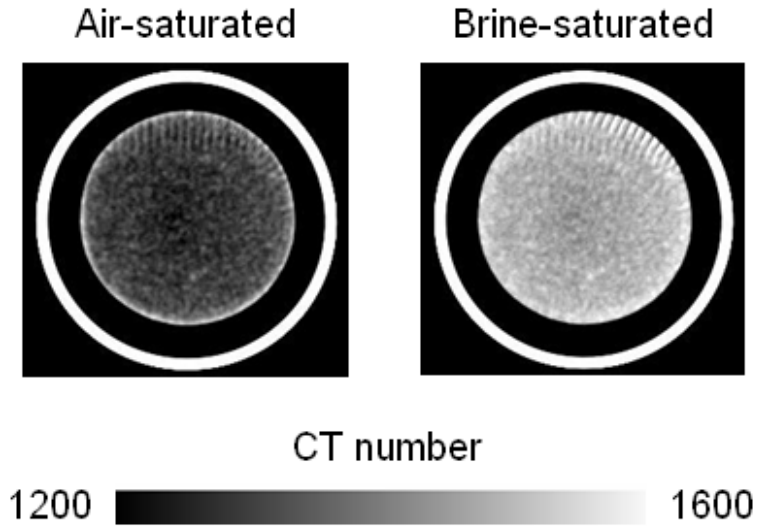

(a) CT images

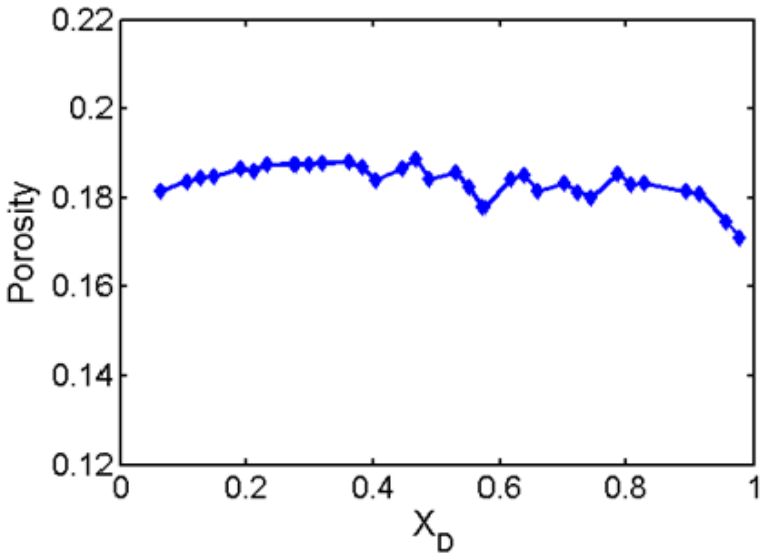

(b) porosity profile

Figure 5.3: Characterization of the 5.0 cm diameter by 60 cm long sandstone core: (a) representative cross-sectional CT images of air- and brine-saturated core at $x/L = 0.5$ and (b) porosity profile along the length of the core.

core holder is mounted on a motorized stage controlled by an automated positioning system for precise, repeatable translation long the length of the core. Thirty-two cylindrical volume sections of the core perpendicular to its central axis are scanned for in-situ measurements in the experiments.

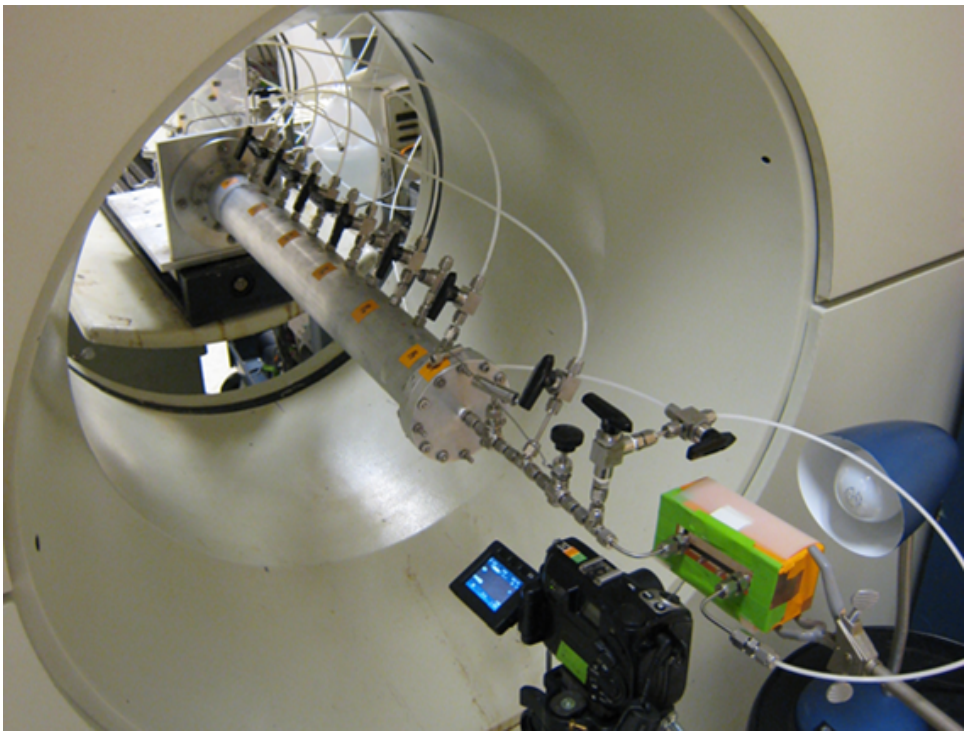

Figure 5.4: Picture of the experimental setup in the lab for a coreflood.

5.2.2 Procedures

Two experiments, a steady-state foam flow and a transient foam flow, are reported. Both the experimental runs start with flushing the core with a large volume (> 20 PV) of 0.5 wt% brine at 2.07 MPa (300 psi) backpressure. The backpressure is periodically released and reapplied during the flushing. This treatment removes virtually all the gas and surfactant from the core. Next, brine is replaced by 1 wt% active surfactant solution to saturate the core. To satisfy any surfactant loss to the rock, at least

$15 \sim 20$ PV of surfactant solution is injected into the system. For the second transient foam flow, the core is pre-saturated with only brine, *i.e.*, no surfactant initially.

For the steady-state run, nitrogen and surfactant solution are coinjected continuously into the presaturated core at specified gas and liquid rates and backpressure. Note that the gas-liquid mixture is never foamed before injection. The pressure profile is monitored by the pressure transducers as an indicator of the steady state. When steady state flow is established after roughly 5 PV of total injection, the stabilized pressure drop along the core is recorded for later reference.

To estimate in-situ foam textures, we carefully sampled the foam bubbles from different pressure taps and measured them with the visualization cell. This series of measurements started with the outlet, and then moved to the next *upstream* port. After finishing the foam texture measurement for one sampling port, we quickly closed the port using a valve, disconnected the foam measurement unit (including the flow tubing, the visualization cell, and the back-pressure regulator), and attached the unit to a spare syringe pump filled with surfactant solution. The back-pressure regulator was then set to the desired pressure value for the next upstream port as recorded during pressure measurement of the whole core at steady state. The syringe pump was enabled to raise the pressure inside the foam measurement unit to the prescribed backpressure. Then, the foam measurement unit was reconnected to the target port and flow was allowed through the visualization cell at the desired backpressure. About one minute was needed from closing the port to connecting the bubble measurement unit to a new sampling port and reestablishing flow. In this way, we minimized disturbance to the region upstream of the sampling port and reduced the time to reach steady state with the new configuration. The pressure upstream of the current sampling port was monitored as an indicator of steady-state. It took about 30 minutes for flow to reestablish steady state for each foam texture measurement.

The bubble residence time in the foam measurement unit is also of interest. The

residence time depends on the length of the flow path and the flow rate. In our experimental setup, pressure taps were machined directly into the core holder and the flow tubing made as short as practical (about 12 in). At the injection conditions, the residence time for foam flowing out of the core, through the sampling port, and into the visualization cell was less then 8 minutes. The tubing used in the experiment was transparent and visualization of foam flowing inside the tubing for diagnostic purposes was possible. The residence time for foam bubbles flowing through the narrow channel inside the visualization cell was 5 seconds. Close inspection of bubbles in tubing and the visualization cell showed no apparent changes to foam texture during transit. In testing, doubling the length of tubing from the sampling port to the visualization cell, as suggested by Ettinger and Radke (1992), produced no changes in the measured texture of bubbles.

The transient flow run is straightforward. Unfoamed gas and surfactant solution mixture are injected into the core presaturated with the surfactant solution. The progress of foam propagation in each run is then tracked by frequent pressure and saturation sweeps. The texture of effluent foam bubbles is monitored with the visualization system versus time as well.

5.2.3 Data Analysis

Raw CT data are processed to obtain porosity and aqueous phase saturation. According to Beer's law, the porosity for each voxel is determined by (Akin and Kovscek, 2003),

$$\phi = \frac{CT_{wet} - CT_{dry}}{CT_w - CT_a} \quad , \tag{5.18}$$

where CT is the X-ray attenuation measured in units of Hounsfield (H), the subscripts w and a represent pure water and air CT numbers, whereas wet and dry refer to fully water- and air-saturated rock, respectively. Similarly, aqueous phase saturation is

computed by

$$S_w = \frac{CT - CT_{dry}}{CT_{wet} - CT_{dry}} \quad , \tag{5.19}$$

where CT is the X-ray attenuation of the partially water-saturated porous medium. The above two calculations are defined on a voxel basis; therefore, the porosity and water saturation are obtained by averaging the matrix of ϕ and S_w values for a particular cross section.

Digital images of foam bubbles are analyzed to characterize foam texture. The original color images are first converted to gray scale intensity images with scale adjustment to enhance contrast in bubble boundaries. Binary images are then obtained by thresholding the intensity images with an appropriate threshold level. The threshold level is critical for identifying bubbles and, thus, is determined interactively by comparing the intensity images with the resulting binary images such that the bubbles in the images are completely separated from each other. The isolated bubbles are identified and labeled by applying a labeling algorithm (Haralick and Shapiro, 1992) to the binary images. The number of bubbles are easily obtained by counting all the labeled objects, and the size of each individual bubble in two-dimensional view is given by the number of pixels associated with the corresponding labeled object. Finally, the size of the two-dimensional bubbles is converted to the diameters of equivalent undeformed spheres by

$$d_b = \left(\frac{6Ah}{\pi}\right)^{\frac{1}{3}} \quad , \tag{5.20}$$

where A refers to the area of bubble in the two-dimensional channel and h refers to the depth of the two-dimensional channel. The statistics of bubbles size distribution and the average foam texture, n_f, are obtained accordingly.

5.3 Results and Discussion

The full physics model and the local equilibrium model described previously are implemented in the framework of a nonisothermal, n-component, compositional simulator capable of handling three-phase flow in response to viscous, gravity, and capillary forces (Kovscek et al., 1997). In the following subsections, we first test the ability of the modified formulation of the population balance model to represent high and low quality foams. Then, steady-state foam flow is examined to ascertain the applicability of the local equilibrium assumption for foam displacement. Finally, we present experimental data or/and model predictions of three transient foam flows, *i.e.*, two linear core foam-flood experiments and one synthetical radial foam flow, to illustrate the capability of the simplified model with the local equilibrium approximation in reproducing the foam-flow behavior.

5.3.1 Model Predictions of Steady State

Before analyzing modeling results, we first examine the steady-state trends of foam flow reported in the literature. In some of the very earliest studies (de Vries and Wit, 1990; Osterloh and Jante, 1992) of foam flow in porous media, it was found that the pressure drop versus flow rate behavior differed between foams created at high gas fractional flow as compared to those created at low gas fractional flow. In the former, capillary suction controls the size of gas bubbles. Pressure drop is sensibly independent of the gas flow rate, but pressure drop increases linearly with liquid flow rate. In the latter regime, the topological properties of the porous medium control bubble size (*i.e.*, one bubble per pore). Pressure drop is then found to be sensibly independent of liquid velocity, but pressure drop increases with gas velocity.

We consider the foam coreflood system described by Kovscek et al. (1995) to test our models. The foam model parameters from the literature (Kovscek et al., 1995), as

provided in Table 5.1, are used to populate the model and the two newly-introduced parameters, n^* and ω, are set to 400 mm^{-3} and 3, respectively. The linear 0.6 m long sandstone core in Kovscek et al. (1995)'s experiments is represented in the simulation by a one-dimensional, uniform grid system that contains 60 gridblocks. Each block is 0.01 m long.

Table 5.1: Model parameters for foam flow simulation with population balance methods from Kovscek et al. (1995)'s paper.

Two-phase flow parameters		Population balance parameters	
Parameter	Value	Parameter	Value
K	1.3 μm^2	k_1	6.6×10^{13} $s^{1/3}$ $m^{-13/3}$
ϕ	0.25	k_{-1}^0	17.0 m^{-1}
f	3.0	$P_{c,max}^*$	3.0×10^4 Pa
k_{rw}^0	0.70	α	8.6×10^{-16} Pa $s^{2/3}$ $m^{10/3}$
g	3.0	$X_{t,max}$	0.90
k_{rg}^0	1.0	C_s^0	0.083 wt%
S_{wc}	0.25	n^*	4×10^{11} m^{-3}
μ_w	1.0×10^{-3} Pa s	ω	3
μ_g	1.8×10^{-5} Pa s		

Figure 5.5 plots contours of the steady-state pressure gradient as a function of the gas and liquid superficial velocities for the modified full physics model. At low liquid rate, the steady-state pressure gradient is not sensitive to the gas velocity resulting in almost vertical contours, especially at liquid rate less than 0.1 m/day. On the other hand, the pressure gradient is virtually independent of liquid velocity, at fixed gas velocity, when the liquid flow rate is high. These trends result from the adjustment of bubble texture as a function of gas and liquid flow rates as embodied in Eqs.(5.2)–(5.3) and shown in Figure 5.6. When the liquid rate is small and the gas rate is fixed, foam bubbles become more finely textured as the liquid rate is increased. A more finely texture foam, at virtually the same advance rate, encounters more resistance to

flow. For foams that are significantly wet, additional liquid injection does not change the bubble size once foam generation is limited by preexisting bubbles blocking pores. Hence, the pressure gradient becomes insensitive to the liquid velocity.

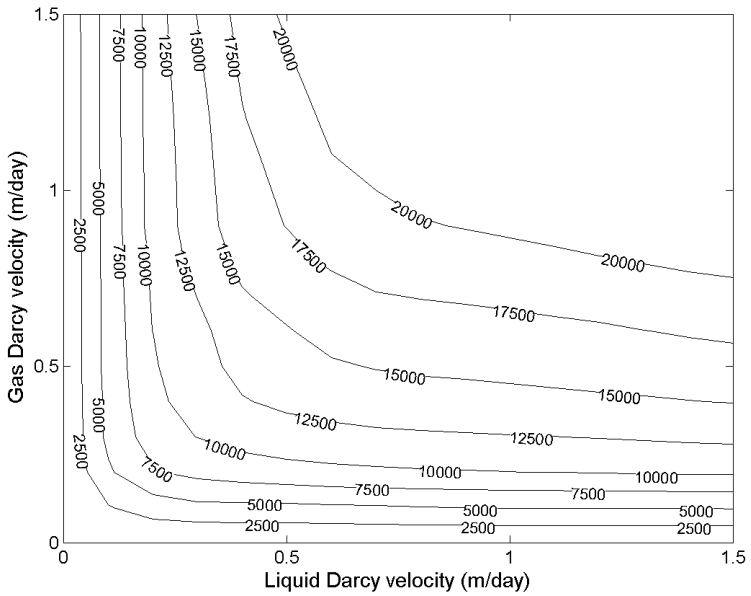

Figure 5.5: Contour of pressure gradients (kPa/m) of steady-state foam flow predicted by the full physics model.

The local equilibrium model also predicts similar contours of the steady-state pressure gradient and average foam texture that are shown in Figure 5.7 and Figure 5.8, respectively. In this calculation, the same set of foam model parameters as mentioned for the full physics model are used. Close comparison of the contours in Figure 5.5 and Figure 5.7 shows slight overestimation of steady-state pressure gradient in the local equilibrium model as compared to that in the full physics model. Similar observations are made in the comparison of the contours in Figure 5.6 and Figure 5.8. These differences are mainly attributed to the approximation of local equilibrium in LEM that results in constant, finely-textured foam in the entrance zone. The overestimated foam texture in the entrance zone causes more flow resistance and consequently

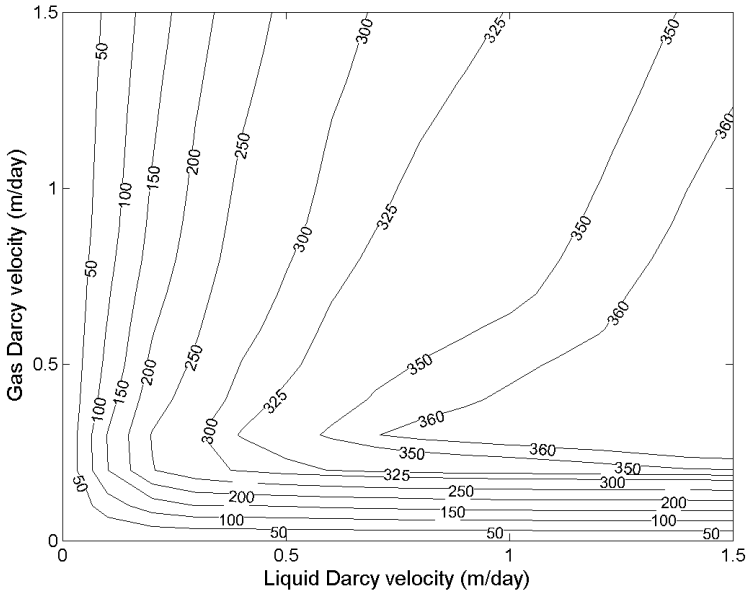

Figure 5.6: Contour of average foam texture (mm^{-3}) of steady-state foam flow predicted by the full physics model.

greater pressure gradient.

Notably, the results of the two population-balance models transition smoothly from high gas fractional flow to low gas fractional flow. The trends from the literature for pressure drop versus gas flow rate are correctly predicted (*e.g.*, Osterloh and Jante, 1992). Recently, Kam et al. (2007) presented a similar contour plot of steady-state pressure gradients obtained with their population-balance model incorporating a bubble-creation function controlled by pressure gradient. In order to generate the low-quality and the high-quality regimes, they simply imposed an upper limit to foam texture and obtained "L"-shaped contours with virtually no transition between two regimes. In contrast, our new models, with incorporation of foam texture dependency of foam generation, are capable of reproducing the low-quality and high-quality regimes as well as a smooth transition in between.

It is interesting to note from the results presented that although the macroscopic

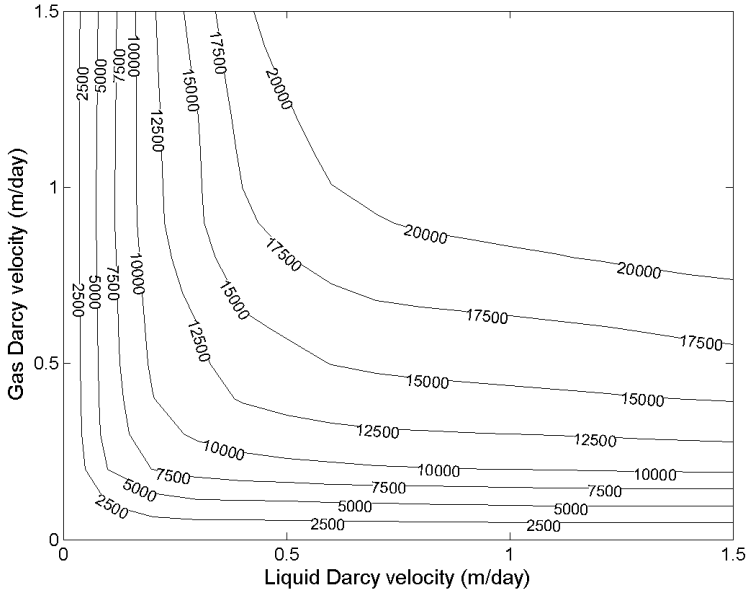

Figure 5.7: Contour of pressure gradients (kPa/m) of steady state foam flow predicted by the local equilibrium model.

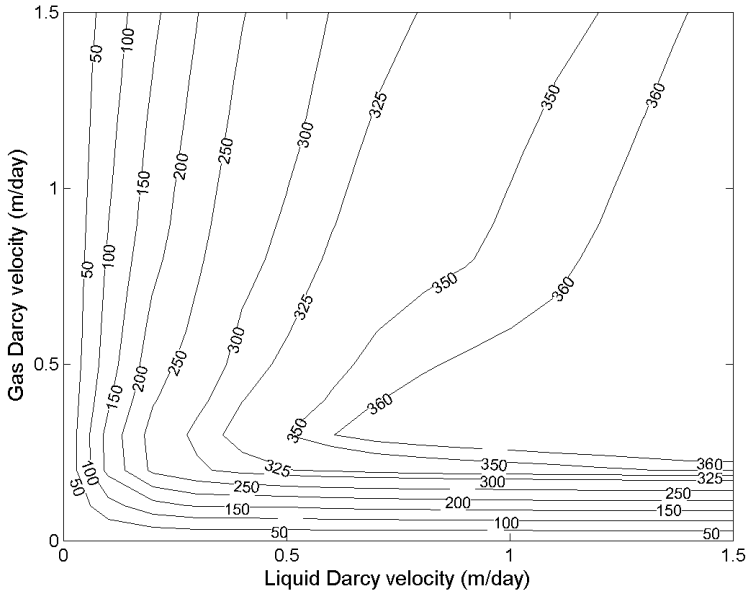

Figure 5.8: Contour of average foam texture (mm^{-3}) of steady-state foam flow predicted by the local equilibrium model.

trends are quite different for low- and high-quality regimes, the constitutive equations for foam generation, foamed-gas effective viscosity, and relative permeability are identical. The seemingly different foam rheology is predicted via the detailed accounting of foam texture versus gas and liquid flow rates without changes to the underlying foam generation equation and parameter adjustment.

5.3.2 Experimental Verification of Local Equilibrium

The local equilibrium approximation is examined with a steady-state foam flow experiment. In this experiment, the gas velocity is 1.125 m/day relative to the back pressure of 2.07 MPa (300 psi), and the velocity of surfactant solution is set at 0.125 m/day to provide a gas fractional flow of 0.90 at the core exit. After the foam flow in the core reaches its steady state, the foam texture along the core is measured using the visualization cell in the fashion described in the previous section. Figure 5.9 gives the measured average foam texture. The dots represent the experimental data. The solid line is a constant fit to all the experimental points except the gray square dot that is obtained close to the core inlet and shows very different foam texture than the other measurement points. The dashed curve illustrates roughly the transition of the average foam bubble size in the entrance zone according to the sparse experimental data points in that zone.

The foam textures measured with the external visualization cell in Figure 5.9 are considered to reflect the characteristic of the in-situ foam textures inside the core. First, the foams are sampled along the core in a careful manner in which the flow conditions upstream of the sampling port remain unchanged by applying appropriate exit pressure. Secondly, one may expect new foam bubbles generated at the exit face of a porous medium and foam texture alteration in the lines leading to the visualization cell. As a result, bubble sizes observed in the visualization cell may not be representative of in-situ texture. Ettinger and Radke (1992) addressed

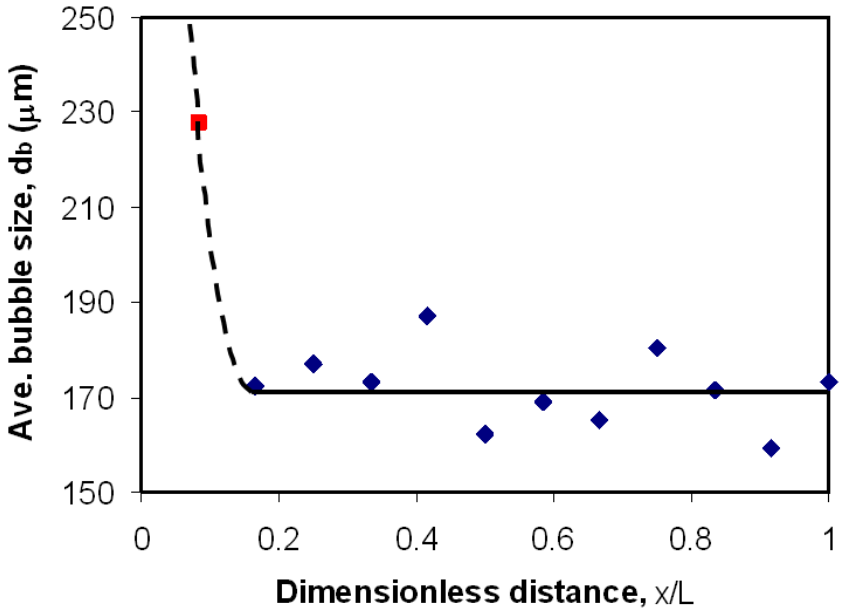

Figure 5.9: Experimental estimates of in-situ foam texture: mean bubble size versus dimensionless distance in a 60 m long, cylindrical Berea sandstone core during a steady state foam flow.

the former issue by comparing weak and strong foams exiting a Berea sandstone with an in-line visualization cell. They found that the foam generation at the core exit face contributes much larger foam bubbles in comparison to the in-situ finely textured foam. Hence, for the bubble size measurement in our experiments, the foam alteration at the core exit face has negligible effects on the results of finely textured foams. Third, flowing in the tubing and fittings prior to the visualization cell, foam bubbles experience coarsening effects due to gas diffusion between bubbles of different sizes. Such a texture alteration to the foam bubbles, however, is ignorable. According to the work by Patzek (1993) who investigated the dependence of bubble size on time during bulk foam flow based on a hypothesis of statistical self-similarity, the number of bubbles decreases as an inverse function of time to the power $1/\left[3\left(1-\alpha\right)\right]$, where α varies from 0 to 1 depending on the bubble shapes. As described in the experimental section, the residence time for foam flowing out of the core, through the sampling port, and into the visualization cell was less then 8 minutes. With our experiment conditions, Patzek (1993)'s theory predicts less than 5% coarsening during the foam flow in tubing and fittings. This was also verified by close inspection of bubbles in tubing and the visualization cell that showed no apparent changes to foam texture during transit. Therefore, our bubble size measurements provide reasonable texture estimates of in-situ foam for the steady-state flow under study.

As shown in Figure 5.9, the measured average foam bubble diameters vary from 160 μm to 230 μm, corresponding to foam texture of 500 mm^{-3} to 170 mm^{-3}. Ettinger and Radke (1992) and Tang and Kovscek (2006) reported their measurements of mean foam texture at the core exit to be 100 mm^{-3} and 200 mm^{-3} for similar sandstones but with different permeabilities and porosities, *i.e.*, $K = 1.3$ μm^2, $\phi = 0.25$ and $K = 0.74$ μm^2, $\phi = 0.20$, respectively. In general, the texture of foam bubbles depends greatly upon the pore-body size of the porous medium due to the nature of the snap-off generation mechanism. Smaller bubbles, or finer foam textures result from

tighter cores provided that surfactant stabilizes the interface. The mean foam textures measured by Ettinger and Radke (1992) and Tang and Kovscek (2006) follow such a trend. Our results of 400 mm^{-3}, considering that our core has lower permeability and porosity, are consistent with those reported in the literature.

One key observation in Figure 5.9 is the profile of the average foam bubble size, as illustrated by the solid and the dashed lines, that reveals the foam evolution along the core in the steady state at given injection conditions. As described before, the gas-liquid mixture is not foamed prior to entering the core and thus the foam bubble size is very large, giving foam texture of nearly zero, at the inlet. The foam bubble size decreases to 220 μm at $x/L = 0.08$ and reaches a plateau around 170 μm with some fluctuations for $x/L \geq 0.2$.

To illustrate the difference in the foam texture between the entrance zone and the plateau zone, Figure 5.10 shows images of foam bubbles obtained at $x/L = 0.08$ and $x/L = 0.50$. Note that the foams sampled at the locations beyond $x/L = 0.2$ look very similar in the visualization cell and therefore only one data point at $x/L = 0.50$ is selected for the purpose of comparison. Large bubbles with diameter greater than 2 mm in a two-dimensional view are frequently observed in the foam close to inlet, whereas the bubbles for the case at $x/L = 0.50$, as shown in Figure 5.10(b), are much finer. The image analysis of the foam bubble images leads to quantitative measures of bubble size distribution in terms of the bubble density and volume fraction as a function of bubble size. The resulting histograms are depicted in Figure 5.11 that confirms our visual estimation of foam texture.

Because of the fixed spacing of 5 cm (2 inches) between sampling ports machined into the core holder, there are not enough measurement points in the entrance zone to resolve more accurately the transition from coarse foam to strong foam. Nevertheless, the observed foam texture profile in Figure 5.9 clearly indicates that the net foam generation occurs mainly within the entrance region of less than $0.2L$ or 12 cm and

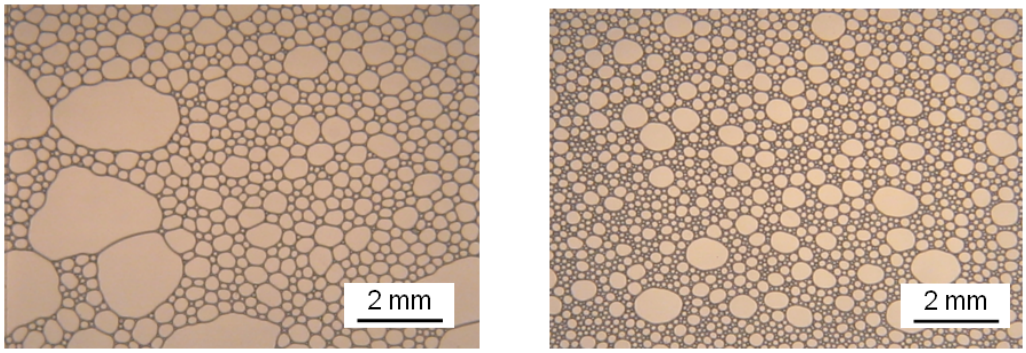

(a) sampled at $x/L = 0.08$ (b) sampled at $x/L = 0.50$

Figure 5.10: Images of foam bubbles sampled at (a) $x/L = 0.08$ and (b) $x/L = 0.50$.

that the rates of foam creation and decay almost balance throughout the majority of the core. This result confirms the applicability of the assumption of local equilibrium, and, consequently, our proposed model for modeling foam displacement as verified further with a transient flow in the next section.

5.3.3 Transient Foam Flow I: Constant Surfactant

Figs. 5.12–5.15 show the experimental and numerical results for the recent transient flow experiment with a surfactant-presaturated core in terms of aqueous-phase saturation, pressure drop, flowing foam bubble density, and texture history of effluent foam. The profiles of those variables are displayed at dimensionless times expressed as pore volume injected, *i.e.*, product of elapsed time and volume injection rate at the exit pressure condition divided by the total pore volume. The experimental data are designated in the figures by square dots that are simply connected by black dashed lines for easy reading. The solid lines and the dash-dot lines show the numerical predictions from the full physics model and the local equilibrium model, respectively. The transient flow tests were conducted with the same flow conditions as in the steady state flow described in the previous section. The numerical results shown in

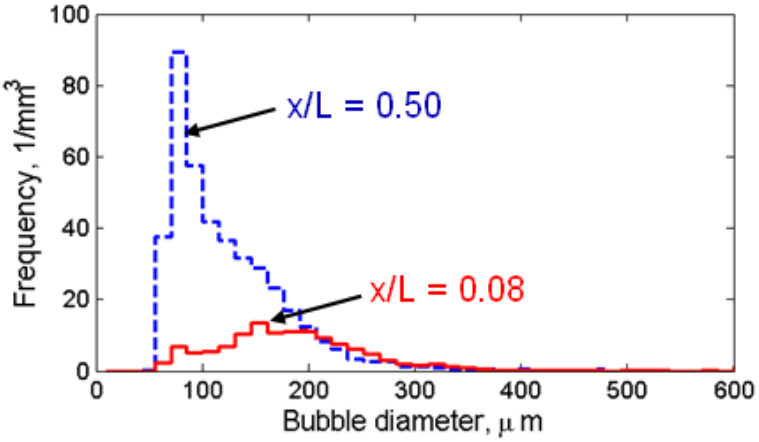

(a) bubble frequency

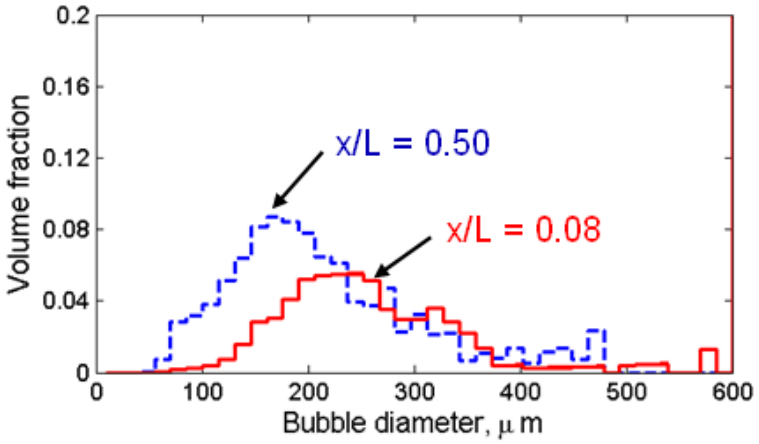

(b) volume fraction

Figure 5.11: Comparison of size distributions of foam bubbles sampled at $x/L = 0.08$ and $x/L = 0.50$.

Figs. 5.12–5.15 are obtained with a one-dimensional, uniform grid system containing 60 gridblocks. All foam model parameters are determined from the experimental data and existing theory by following the matching procedure described by Kovscek et al. (1995). Table 5.2 summarizes those model parameters.

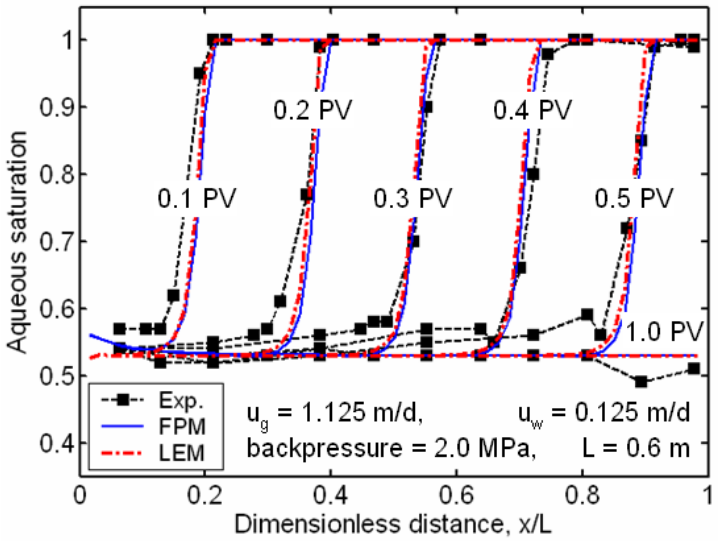

Figure 5.12: Experimental and numerical aqueous saturation profiles during transient foam flow.

As seen in Figure 5.12, the aqueous-phase saturation fronts at all the time levels are steep. The aqueous-phase saturation is approximately 0.52 upstream of the front and remains 1.0 downstream of the front. This clearly shows that the injected gas first desaturates the rock at the entrance and then propagates along the core in a piston-like fashion, providing a very efficient displacement of the aqueous phase. Also, even though gas and surfactant solution are injected separately, the low aqueous saturation near the inlet, as shown in Figure 5.12, suggests rapid foam generation in the entrance zone. The experimental pressure profiles in Figure 5.13 show shallow pressure gradient near the inlet, indicating that the foam resistance is small and foam textures are coarse in the entrance region. In addition, the steep pressure gradient

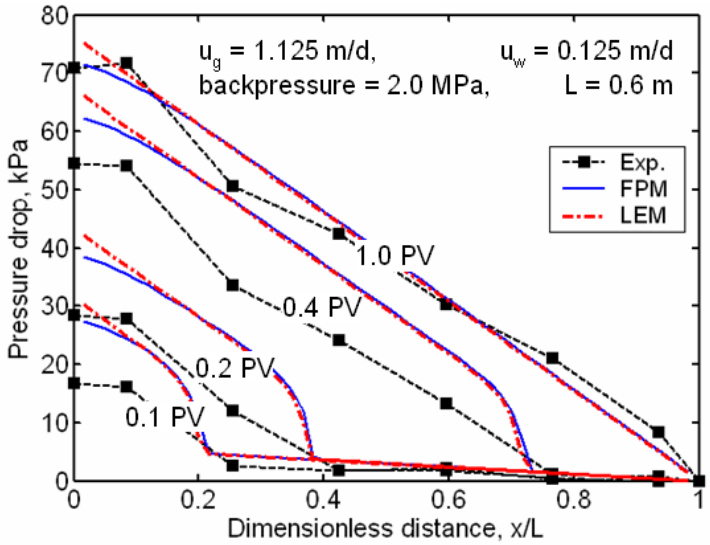

Figure 5.13: Experimental and numerical pressure profiles during transient foam flow.

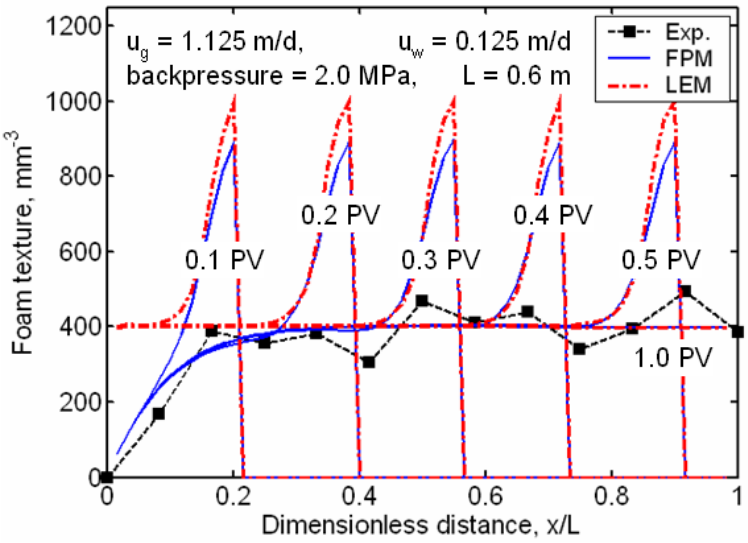

Figure 5.14: Foam texture profiles during transient foam flow. Experimental data are obtained at steady state.

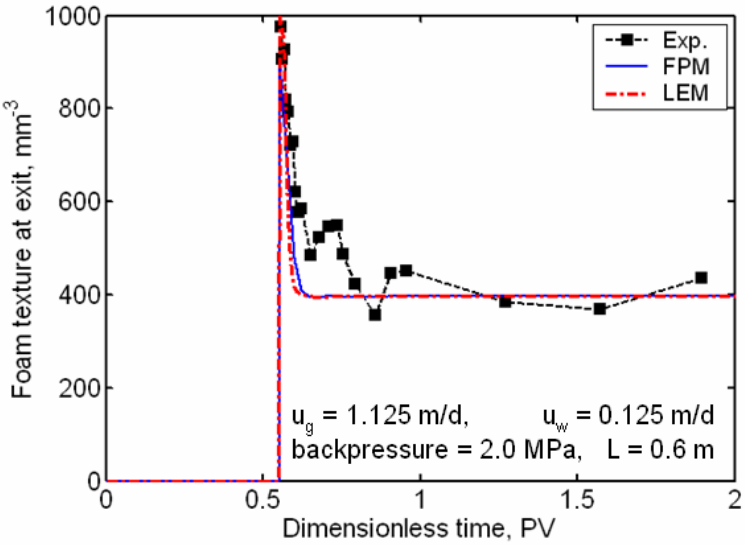

Figure 5.15: Experimental and numerical texture of effluent foam versus time during transient foam flow.

Table 5.2: Model parameters for foam flow simulation with population balance methods.

Two-phase flow parameters		Population balance parameters	
Parameter	Value	Parameter	Value
K	0.3 μm^2	k_1	1.65×10^{15} s$^{1/3}$ m$^{-13/3}$
ϕ	0.18	k_{-1}^0	10.0 m^{-1}
f	3.0	$P_{c,max}^*$	3.0×10^4 Pa
k_{rw}^0	0.70	α	7.4×10^{-18} Pa s$^{2/3}$ m$^{10/3}$
g	3.0	$X_{t,max}$	0.78
k_{rg}^0	1.0	C_s^0	0.083 wt%
S_{wc}	0.38	n^*	1×10^{12} m^{-3}
μ_w	1.0×10^{-3} Pa s	ω	3
μ_g	1.8×10^{-5} Pa s		

observed upstream of the front confirms the existence of strong foam flow.

In both saturation and pressure profiles, the theoretical predictions by the FPM and LEM virtually overlap with each other, and both track the experimental results well. Only a slight discrepancy between the FPM and LEM is observed in the relatively short entrance region. The FPM predicts that the aqueous-phase saturation is high at the core inlet and then drops to a steady value of 0.52 by $x/L = 0.1$. Also, the FPM results show a shallow pressure gradient near the core inlet that is consistent with the experimental observation. On the other hand, because of the local equilibrium approximation, the LEM does not capture the transition in the entrance region in term of aqueous saturation and pressure drop. The maximum errors in the entrance aqueous saturation and pressure drop due to the local equilibrium approximation, however, is less than 7% relative to those in the FPM results.

Because of the difficulty in measuring in-situ foam texture in a transient flow setting, experimental data of mean foam texture only at steady state are available in Figure 5.14. The foam texture profiles predicted by FPM and LEM at 0.1, 0.2, 0.3, 0.4, 0.5, and 1.0 PVI are reported in Figure 5.14 to illustrate the foam texture evolution. Coarse foam textures are observed near the inlet, within approximately one fifth of the core, at all time levels in the full physics model. This is consistent with the measured foam texture at steady state and the observation of shallow pressure gradient in Figure 5.13. Note again that nitrogen and surfactant solution are injected separately into the core and thus the foam bubble experiences net generation in the entrance region before it reaches the local equilibrium between foam generation and coalescence. As expected, the local equilibrium model does not capture this transition of foam texture within the entrance zone. Instead, it gives constant, finely-textured foam throughout the foamed-gas zone.

Another interesting feature of the foam texture transient profiles in Figure 5.14 is that the foam texture peaks at the foam front in both models. We conducted a

sensitivity analysis on the gridblock size by refining the current model by factors of 2, 4, 8, and 16 to check the convergence behavior of the numerical solution of foam texture, as described in the Appendix B. In summary, our sensitivity study shows that the predicted texture front becomes slightly sharper as the gridblock size decreases from 0.01 m to 1.25×10^{-3} m and that the converged front is obtained when the gridblock size is equal to or smaller than 1.25×10^{-3} m. All the cases with different gridblock sizes confirm the existence of the observed foam texture peak. Prior studies have predicted, but not measured, an elevation in foam texture at the displacement front (Kam et al., 2007; Kovscek et al., 1997).

The fine foam texture at the front is mainly due to intensive net foam generation. The aqueous-phase saturation increases from 0.52 to 1.0 across the front and the foam coalescence rate drops quickly with high aqueous-phase saturation. On the other hand, the interstitial gas and water velocities at the front gives a high foam generation rate. Consequently, a region of intensive net foam generation exists near the front leading to large foam textures. Downstream of the front, no gas is present and the foam textures are zero. The magnitude of the foam texture peak in the numerical results is set by the limiting foam texture, n^* that is determined from the experiment data as described next.

The existence of the foam texture peak predicted by the models is also confirmed with our measurement of foam texture of effluent foam bubbles versus time. As shown in Figure 5.15, the foam texture of 1,000 mm^{-3} is recorded at 0.55 PVI when the foam front breaks through. Afterward, the texture of effluent foam decreases rapidly with time and stabilizes to a steady-state value of 400 mm^{-3} after approximately 1.0 PVI. The limiting foam texture, n^*, in our models is set by the porous medium according to the one bubble per pore limit. As pore size decreases, n^* increases. The maximum foam texture observed experimentally provides a good estimation of n^* for the numerical models. Our choice of $n^* = 1000$ mm^{-3} for the FPM and

LEM is based on such an experimental observation. Figure 5.15 also shows that the theoretical predictions give similar trends as the experimental data, but with sharper drop in the foam texture after gas breakthrough.

5.3.4 Transient Foam Flow II: Transient Surfactant

The second transient foam flow of interest is the case where unfoamed gas and surfactant solution are coinjected into a porous medium fully saturated with brine but not surfactant solution initially. Figures 5.16–5.19 present the experimental and computed aqueous phase saturation profiles, the computed and measured pressure drops, the computed foam texture, and aqueous phase concentration of surfactant for such a experiment conducted by Kovscek et al. (1995). For numerical predictions, the 0.60 m long core cylinder is represented with a one-dimensional, uniform grid system consisting of 60 gridblocks, and the same set of model parameters as provided in Table 5.1 is used.

Different from the previous case where one single sharp front propagates through the core, Figure 5.16 indicates two separated fronts at early times for this transient flow. The faster front, *e.g.*, located at $x/L = 0.38$ at 0.1 PVI, corresponds to the displacement due to unfoamed gas. Because of its high mobility, the unfoamed gas breaks through quickly, resulting in a liquid recovery less than 0.2. The foamed gas displacement forms the second front that appears to be much sharper, as seen at later times in Figure 5.16. The foam piston-like front, after gas breakthrough, continues down the core expelling most of the liquid that the first unfoamed gas displacement front left behind. The pressure drops shown in Figure 5.17 track the saturation profiles well. The steep pressure gradients indicate the presence of foamed gas. Despite the little mismatch for the first front at early times, good agreement between numerical predictions and experimental measurement is observed in both Figure 5.16 and Figure 5.17.

Figure 5.18 compares the local equilibrium and full physics model foam textures. A discrepancy in calculations again exists in the relatively short entrance region. This entrance region is only about 15% of the core length. Because the concentration of surfactant decreases in the flow direction, as seen in Figure 5.18, foam stability also decreases in the flow direction. Just downstream of the surfactant, no surfactant is present in the liquid and available to stabilize the dispersed gas phase. Hence the foam texture declines smoothly to zero in this case. It is also noticed that there are several numerical artifacts in the foam texture solution from LEM. This is likely due to the numerical instability of LEM for the solution near the front where sharp changes in both saturation and surfactant occur. We argue that such small numerical errors are limited to a narrow front region and have negligible effects on the predictions of other key parameters, such as pressure and saturation profiles.

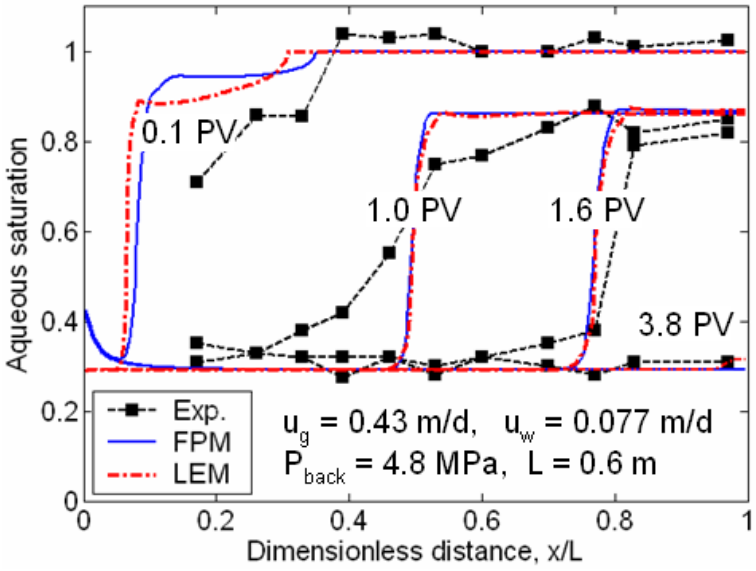

Figure 5.16: Experimental and numerical aqueous saturation profiles during transient foam flow.

Overall, the comparisons of numerical results and experimental measurements presented in Figures 5.12–5.15 and Figures 5.16–5.19 show good agreement. Especially,

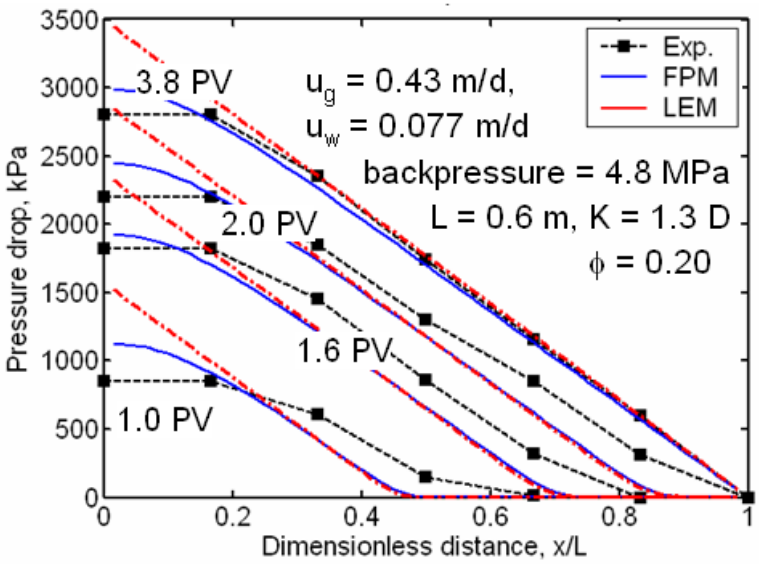

Figure 5.17: Experimental and numerical pressure profiles during transient foam flow.

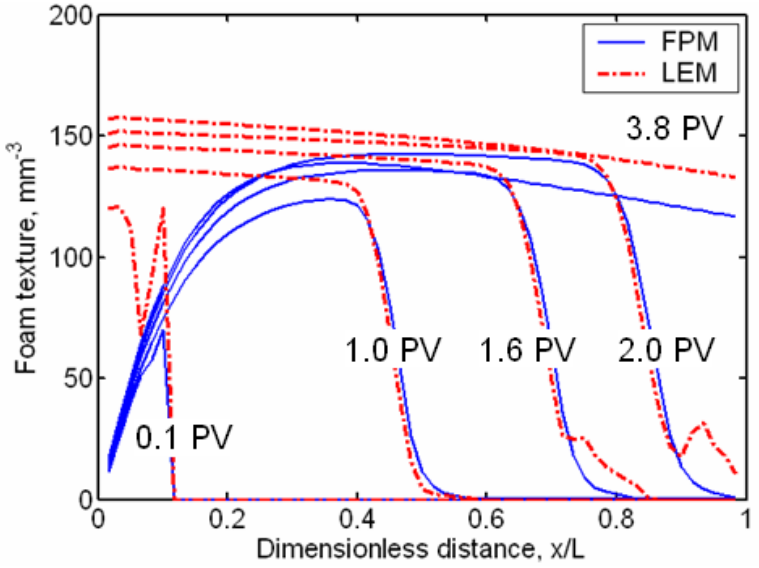

Figure 5.18: Foam texture profiles during transient foam flow.

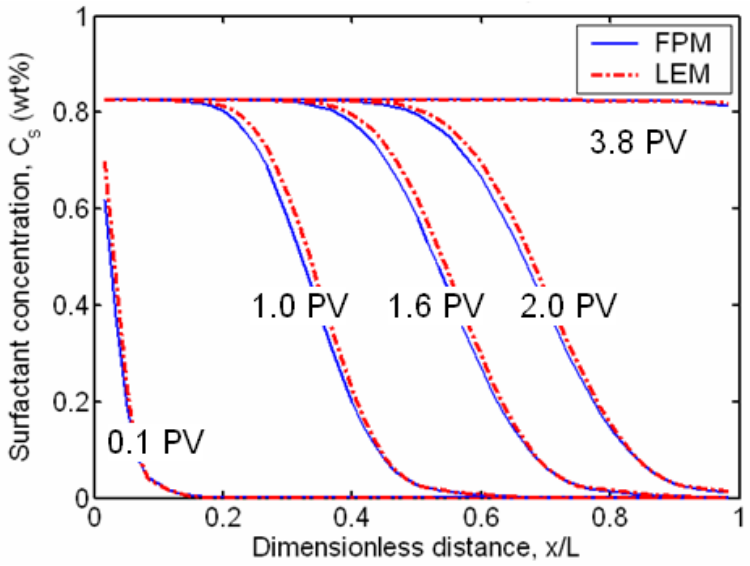

Figure 5.19: Surfactant concentration profiles during transient foam flow.

our local equilibrium model reproduces the transient flow behavior very well except the entrance and front regions for the two foam flow experiments reported above and in the previous subsection. Of the various measurements, pressure drop appears to present the least agreement. Experimentally, the pressure drop is resolved at 10 cm intervals in the central section of the core. Calculations of the pressure drop response arising from a peak in foam texture at the displacement front display a significant pressure gradient in a roughly 1 cm region (Figure 5.13). Hence, the pressure measurements are not at sufficient spatial resolution to resolve the effect on pressure drop of an elevation in foam texture at the displacement front. As illustrated in the transient foam flow experiment, both the entrance and front regions are small for typical foam flood or field applications. The resulting error due to the approximation in the non-equilibrium regions in LEM is expected to be acceptable.

Notably, even though no optimization effort has been devoted to the implementation of the local equilibrium model for fast simulation run times, we observe nearly

50% CPU time cut in simulation runs of the presented transient flow with local equilibrium as compared to simulations with the full physics model. This is expected because the formulation of the local equilibrium model eliminates the coupled foam population balance equation, and therefore reduces the linear system of equations by one per block. More results of CPU time comparison are available in Appendix B.

5.3.5 Transient Foam Flow III: Radial Flow

With excellent results of the LEM for predicting linear foam flows as presented in the previous two subsections, we next consider simultaneous injection of surfactant solution and nitrogen into a radial, one-dimensional, homogeneous porous medium to test the applicability of the LEM to radial flow. The porous medium is 1 m thick, 72 m in radius, with a permeability and porosity of 1.3 D and 0.25, respectively. The porous medium is presaturated with a surfactant solution initially in a fashion similar to the injection of a large slug of surfactant solution in a surfactant-alternating gas process. The volumetric injection rates of surfactant solution and nitrogen are 0.165 m^3/day and 3.00 m^3/day, respectively, relative to a back pressure of 4.73 MPa, yielding a gas fractional flow of 0.95. In numerical simulation, a one-dimensional, radial grid system consisting of 72 grid blocks with $dr = 1$ m is adopted to represent the porous medium. With assumption of the same rock type of the porous media as that used in the transient foam flow II, the foam model parameters summarized in Table 5.1 are used for predicting the radial foam flow.

Figures 5.20–5.22 give the numerical simulation results for this radial foam flow obtained with the FPM and the LEM. As seen from the profiles of aqueous saturation in Figure 5.20, both the FPM and LEM predict a sharp aqueous front that propagates through the porous medium at a reducing front velocity because of the constant injection rate and the radial geometry. The breakthrough of the aqueous front occurs at 0.75 PVI approximately. Considerable pressure gradients, as depicted in Figure 5.21,

are observed in the region upstream of the aqueous saturation front, indicating the presence of strong aqueous foam. The pressure gradient gradually decreases along the radius away from the center where gas and liquid are coinjected. The variation in the pressure gradient is consistent with the foam texture profiles shown in Figure 5.22. Both the models predict finer foam texture near the injection point and the foam bubbles become coarser as they move along the radius. This is because of the velocity dependency of foam generation and coalescence mechanisms. Larger aqueous phase velocity results in more rapid snap off events and consequently higher foam generation rates. With the constant liquid injection rate and the radial geometry of the flow, the aqueous phase velocity decreases quadratically as the injected fluid flows into wider region along the radial direction. As a result, foam bubbles experience a coarsening effect as they moves radially through the porous medium. Foam texture peaks are again shown at the fronts where, as discussed in the previous two transient foam flows, net foam generation occurs due to the sharp changes in gas and aqueous phase saturations. The comparison of the predicted profiles of the key measures presented in Figures 5.20–5.22 reveals excellent agreement between the LEM and FPM, although slight difference exist near the injection point.

In summary, considering the well-matched results presented above for the three different foam flows, the proposed local equilibrium model is proved to be an effective approach for modeling foam flows in porous media as an alternative to the full physics population balance model.

5.4 Concluding Remarks

This chapter presents experimental and numerical investigations of foam flow in porous media. We propose a foam texture dependency of the foam generation coefficient and extend a previous population balance model to the low-quality and

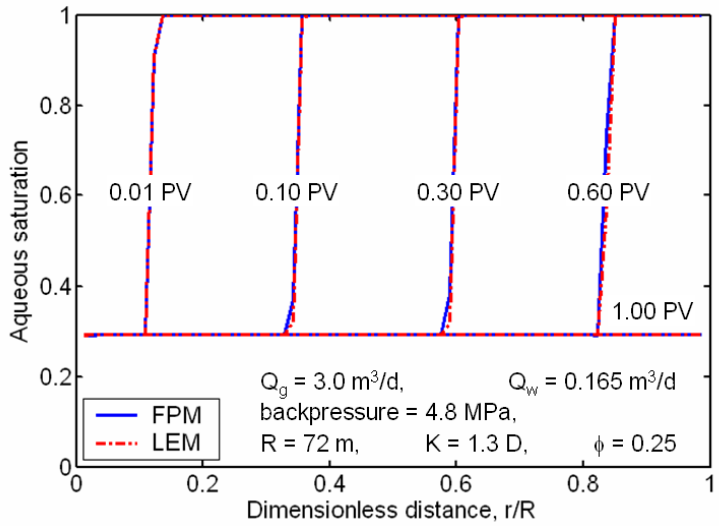

Figure 5.20: Numerical aqueous saturation profiles predicted by FPM and LEM during radial foam flow.

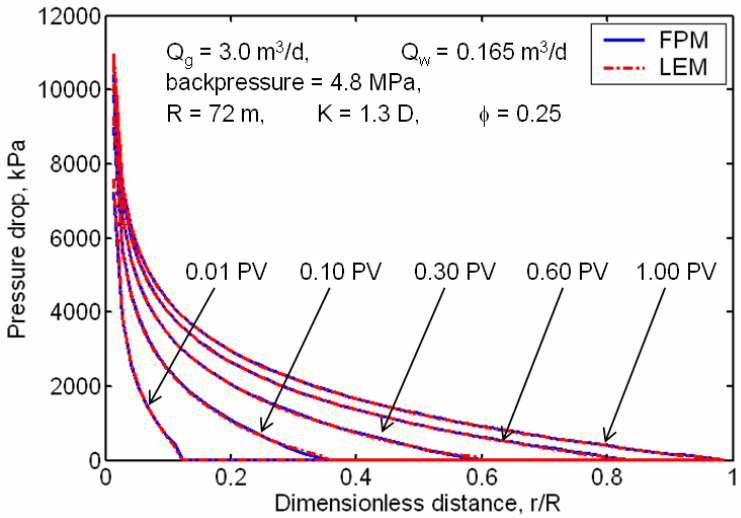

Figure 5.21: Numerical pressure profiles predicted by FPM and LEM during radial foam flow.

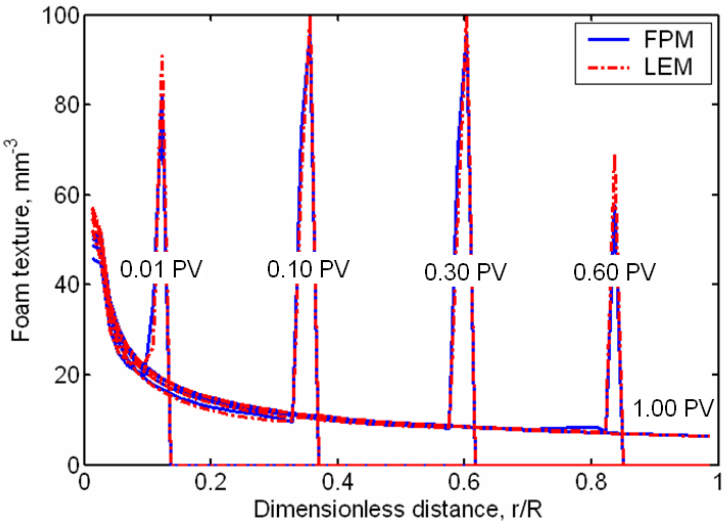

Figure 5.22: Foam texture profiles predicted by FPM and LEM during radial foam flow.

high-quality strong foam flow regimes. The population balance model with foam texture dependency of foam generation predicts successfully the steady-state pressure gradient trend in the low-quality and high-quality foam flow regimes as well as a smooth transition between regimes.

A simplified population-balance model resulting from the local equilibrium approximation is also proposed and implemented for simulating foam processes. Experiments of steady-state and transient foam flows were conducted with a one-dimensional, linear core to verify our new models quantitatively. Experimental estimates of steady-state in-situ foam texture are achieved with a visualization cell. The profile of measured foam steady-state texture shows that the entrance region required for foam texture to reach local equilibrium is shorter than 12 cm for the case under study. Foam generation and decay rates balance throughout the majority of the core. These observations support the assumption of local equilibrium as an approximation for transient foam modeling.

The predictions of the local equilibrium model for two transient foam coreflood

experiments are in good agreement with both the full physics model and experimental results, except for a slight mismatch in the entrance region. For a field-scale radial flow, the local equilibrium model gives virtually identical results to the full physics model. Moreover, the local equilibrium model is more efficient in terms of computational cost in comparison to the full physics model, thereby appearing to be a potentially effective tool for modeling at field scale. Consequently, we will apply this local equilibrium model in the next chapter to simulate and evaluate the novel concept of FA-SAGD from a numerical perspective.

Chapter 6

Foam-Assisted SAGD

The economical success of a SAGD process relies on two key operations, even development of the steam chamber along the full length of the injector well and effective control of steam breakthrough by sustaining a liquid level between the injector and producer (*i.e.*, steam trap control). As mentioned in Chapter 2, experiments showed promising performance of the SAGD process in high-quality, homogeneous reservoirs. For fields with intrinsic heterogeneity, however, the steam chamber normally formed only around well segments surrounded by high permeability formations. The resulting low sweep efficiency led to substantial reduction in the oil production rate and total oil recovery. The injectivity variability along the horizontal injection well also complicates the control of steam breakthrough. To overcome those difficulties, we propose the use of steam foam to divert live steam from high permeability zones and delay steam breakthrough. In this chapter, we first introduce the basic idea of Foam-Assisted SAGD (FA-SAGD) and analyze its potential advantages over the conventional SAGD process. Additional treatments added to the previous foam simulator for simulating SAGD and FA-SAGD processes are described. After giving the details of the synthetic reservoir simulation model, we test the newly-developed foam simulator for SAGD-type simulations by comparing the oil production rates

predicted by numerical simulation and Butler's analytical theory. Then, simulation results of FA-SAGD and SAGD are shown and discussed to illustrate the difference in the performance of the two processes. The chapter completes with a brief summary.

6.1 Concept of Foam-Assisted SAGD

The idea of FA-SAGD originates from the unique behaviors of foam flowing in porous media. In a FA-SAGD process, surfactant solution is coinjected, continuously or intermittently, with steam into a reservoir to generate steam foam in place with the typical SAGD well-pair configuration. Foaming steam during the SAGD operation potentially improves SAGD performance in two ways.

The first mechanism is due to the strong dependency of foam texture on the liquid phase saturation that may result in favorable in-depth modification to the steam chamber. Figure 6.1 depicts the expected distributions of steam and steam foam within the steam chamber for SAGD and FA-SAGD, respectively, in the vertical cross-section perpendicular to the horizontal well direction. Due to gravity, steam is dry or the steam quality is high in the upper portion of the steam chamber. In the lower part of the steam chamber, steam becomes wetter because liquid water moves downward and accumulates under buoyancy forces. The variation of the steam quality within the steam chamber in the SAGD process is illustrated by colors in Figure 6.1(a). Bright red color indicates high steam quality and shading (dark) red color designates low steam quality. The foam generation rate, as described in Chapter 5, increases proportionally with the liquid phase velocity (see Eq. (5.1)). This foam generation dependency and the steam quality distribution described above make it very likely that, if steam and surfactant solution is coinjected as proposed for a FA-SAGD process, strong (fine) foam may be created in the lower portion of the steam chamber, *i.e.*, mainly in the interwell region. As illustrated in Figure 6.1(b), only

weak (coarse) foam will be expected in the upper portion of the steam chamber. The presence of strong steam foam normally causes an increase in flow resistance to steam flow. Hence, in the FA-SAGD process, high flow resistance exists in the interwell region that reduces steam flowing towards the production well and thereby making steam trap control much easier to achieve.

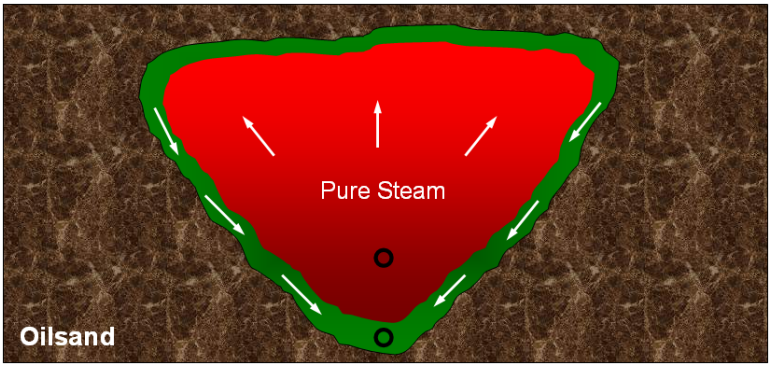

(a) SAGD

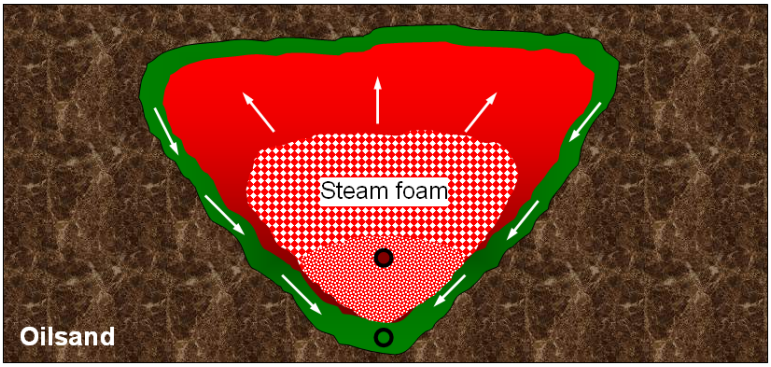

(b) FA-SAGD

Figure 6.1: Schematic of (a) SAGD and (b) FA-SAGD.

The second mechanism relies upon the potential of foam to block partially high-permeability oil-depleted regions and to divert steam flow into low permeability zones. For a heterogeneous reservoir, the formation permeability may varies significantly along the horizontal wells whose lengthes are typically 500–1,000 m. For steam only injection, such variation normally results in inconsistent injectivity along the well

length, that, in turn, causes uneven steam chamber development. A field example is shown in Figure 1.2 in Chapter 1. By injecting steam together with a small amount of surfactant solution, strong foam may be generated in-situ in the high permeability segments. The resulting flow resistance in the high permeability zones blocks steam flow and diverts steam to low permeability regions. The diverting effect of foam will even out the steam injection profile along the well, thereby resulting in uniform steam chamber development and better performance.

The numerical evaluation of the second mechanism of FA-SAGD requires three-dimensional simulation with heterogeneous reservoir settings. Because of the limitations of the current simulator, we focus only on two-dimensional simulation of FA-SAGD and examine the first mechanism described above to demonstrated the advantage and feasibility of foaming steam in SAGD.

6.2 Additional Treatments for FA-SAGD Simulation

The FA-SAGD process involves complex water-steam-oil three-phase flow and rupture temperature transient across the reservoir. According to the experimental observations reported in the literature, both the presence of oil phase and temperature variation affect foam flow behavior. Therefore, additional treatments are required to address such effects in the simulation of the FA-SAGD process. The following two subsections provide corresponding details.

6.2.1 Effect of Oil on Foam Mechanisms

The presence of oil destabilizes foam. Several researchers observed that the pressure gradient in flowing foam decreases with increasing oil saturation. This indicates

that the flow resistance of the foam decreases and that the rate of foam coalescence increases. Generally in these studies, the pressure gradient gradually increases as oil saturation decreases from about 0.40 to 0.15 and then sharply increases to near the pressure gradient of oil-free foam as the oil saturation further decreases from 0.15 to 0.05. According to those observations and the pinch-off mechanism theory, Myers and Radke (2000) suggested a complicated function, particularly for the case at residual oil saturation, for the foam coalescence rate. Nevertheless, for simplicity, we incorporate the following expression to address the additional foam coalescence due to the presence of oil:

$$r_{co} = k^0_{-2} \left(\frac{S_o - S_{or}}{S_{oi} - S_o} \right) |v_f| n_f \quad , \tag{6.1}$$

where k^0_{-2} is the number of oil-gas contact sites per volume of gas and the other variables have their usual definitions. Myers and Radke (2000) argued that the number of residual oil globules per volume of gas increases with decreasing pore size or permeability and therefore k_{-2} should increases as the permeability decreases.

6.2.2 Mass Balance of Surfactant

As indicated in Eq. (5.4), the surfactant concentration in the wetting phase (*i.e.*, aqueous phase in this study) determines the stability of newly-generated foam bubbles and thus affects directly the rate of foam coalescence. The rate of surfactant propagation in the aqueous phase is affected by adsorptive losses on the rock surface and by partitioning into a bypassed oil phase. In general, surfactant adsorption decreases with increasing temperature because the surfactant solubility increases with increasing temperature. In addition, only adsorptive losses are significant in comparison with losses by partitioning into an oil phase. Hence, we consider only surfactant adsorption on the rock in the current model. Following Friedmann et al. (1991)'s

work, we further assume that surfactant adsorption on the rock can be modeled with a Langmuir-type model and is unaffected by foam lamellae. Those assumptions lead to the following mass balance equation (in one dimension) that is adopted here to track the surfactant concentration:

$$\frac{\partial}{\partial t}\left[\phi S_w C_s + (1-\phi)\delta\rho_r\Gamma\right] + \frac{\partial}{\partial x}(u_w C_s) = C_s Q_w \quad , \tag{6.2}$$

where C_s is the surfactant concentration, δ is the rock surface area per unit mass, ρ_r is the density of rock, and Γ is the surfactant adsorption on the rock. The other symbols have their usual definitions. The surfactant adsorption on the rock, Γ is modeled by

$$\Gamma = K_s A_s C_s/(1 + K_s C_s) \quad , \tag{6.3}$$

and

$$K_s(T) = K_s(T_0)\exp\left[-\frac{\Delta Q}{R}\left(\frac{1}{T_0} - \frac{1}{T}\right)\right] \quad , \tag{6.4}$$

where A_s is a constant in Langmuir model, T_0 is a reference temperature, $K_s(T_0)$ is a constant value measured at the reference temperature, R is gas constant, and ΔQ is the heat change of adsorption.

6.3 Reservoir Simulation Model

A synthetic oilsand reservoir described by Butler (1998b) is adopted with minor changes for the numerical investigation of FA-SAGD. The reservoir has a 20 m pay zone with permeability of 1 D, porosity of 0.33 and the initial oil saturation of 0.75. The oil viscosity is 100,000 cp at the reservoir temperature, 15°C, and reduces to 80 cp when its temperature increases to 100°C. The initial reservoir pressure is 1,200 kPa. Table 6.1 summarizes the key reservoir properties as well as the foam model

parameters. The relative permeability curves are shown in Figure 6.2.

Table 6.1: Reservoir properties and population balance parameters for FA-SAGD studies.

Reservoir Properties		Population balance parameters	
Parameter	Value	Parameter	Value
Reservoir temperature	15°C	k_1	2.3×10^{14} $s^{1/3}$ $m^{-13/3}$
Oil density	1.00 g/cc	k^0_{-1}	4.5 m^{-1}
Oil viscosity at T_{res}	100,000 cp	k^0_{-2}	0.1 m^{-1}
Oil viscosity at 100°C	80 cp	$P^*_{c,max}$	3.0×10^4 Pa
Reservoir thickness	20 m	α	9.2×10^{-17} Pa $s^{2/3}$ $m^{10/3}$
Thermal diffusivity	0.07 m^2/day	$X_{t,max}$	0.90
Porosity	0.33	C^0_s	0.083 wt%
Initial oil saturation	0.75	n^*	1×10^{11} m^{-3}
Residual oil saturation	0.13	ω	3
Reservoir permeability	1.00 D		
Initial reservoir pressure	1,200 kPa		

In a commercial SAGD project, the field is normally developed by a series of horizontal well pairs at a lateral spacing ranging from 75 to 150 m, as described in Chapter 3. Similarly, a confined reservoir simulation model is considered here. Due to the element of symmetry and the assumption of a homogeneous system, we model only one half of the repeated unit. A uniform grid system with 2 m × 2 m grid blocks, as shown in Figure 6.3, is used to represent the vertical cross-section of the reservoir for numerical simulation. The dimension along the horizontal well is 1 m in the model and the production rates will be reported per unit length base. The boundary condition is assumed to be no flow and heat losses to overburden and underburden are computed by a semianalytical model developed by Vinsome and Westerveld (1980).

For both SAGD and FA-SAGD simulations presented next, the recovery processes starts with a preheating period of 3 months that is normally required to establish hydraulic and thermal communication between the injection and the production wells.

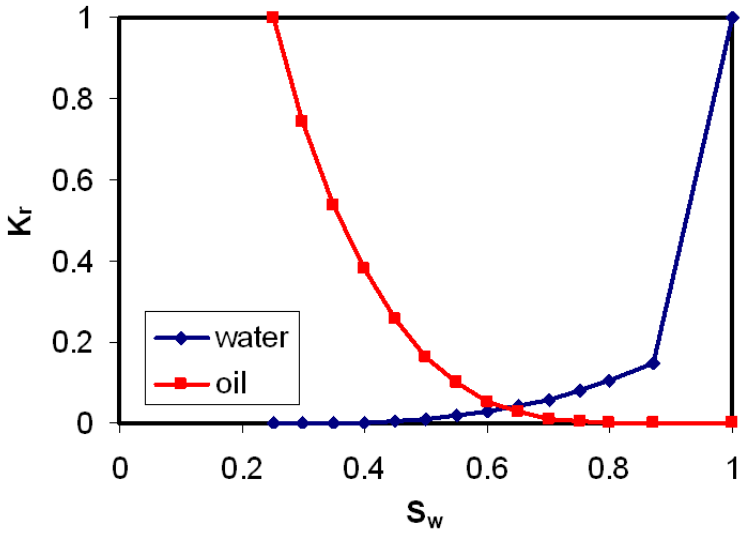

(a) Water-Oil system

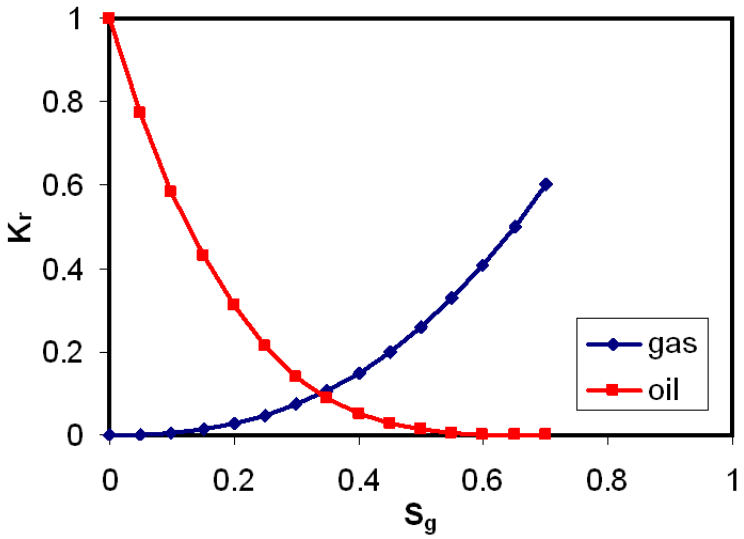

(b) Gas-oil system

Figure 6.2: Relative permeability curves for SAGD and FA-SAGD simulations: (a) water-oil system and (b) gas-oil system.

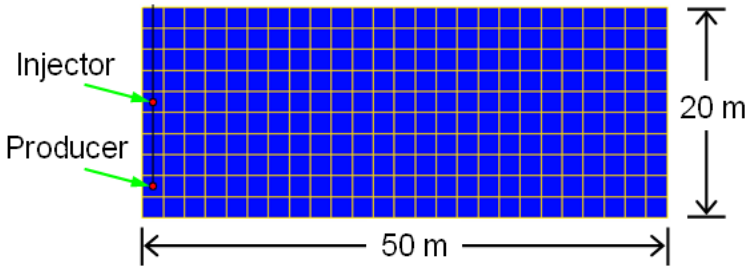

Figure 6.3: Geometries of the two-dimensional reservoir model for simulating SAGD and FA-SAGD.

After the oil between the wells becomes mobile, steam or steam and surfactant solution are injected at the maximum pressure of 1,300 kPa and the production well is operated at a fixed minimum bottom hole pressure of 1,200 kPa. The simulation runs are terminated after 15 years of operation.

6.4 Results and Discussion

Simulations of FA-SAGD are conducted with the recently-developed foam simulator that is implemented with the simplified local-equilibrium foam model. The focus of this study is to examine the foam effects on the steam chamber development and on the oil production. Before analyzing and discussing the simulation results of FA-SAGD, we present the verification of the capability of the simulator for modeling SAGD-type processes by comparing its simulation results of a typical SAGD process against the Butler's analytical solution and CMG STARS's simulation results, as shown next.

6.4.1 Verification of Foam Simulator for SAGD Simulation

Figure 6.4 and Figure 6.5 compare the oil production rate and the cumulative oil production predicted by three methods for the synthetic oilsand reservoir operated in

a SAGD mode. The three methods include Butler's analytical theory, simulation using STARS (Computation Modeling Group), and simulation using the foam simulator (M^2NOTS). The gravity drainage theory developed by Butler incorporates thermal and flow dynamics occurring at the steam chamber boundaries and effects of the steam chamber rising and shape. The derived analytical solution of the oil drainage rate as a function of time was confirmed with field observations. More details of the Butler's analytical solution are available elsewhere (Butler, 1998b). Identical reservoir models are supplied to STARS and M^2NOTS to ensure an apples-to-apples comparison.

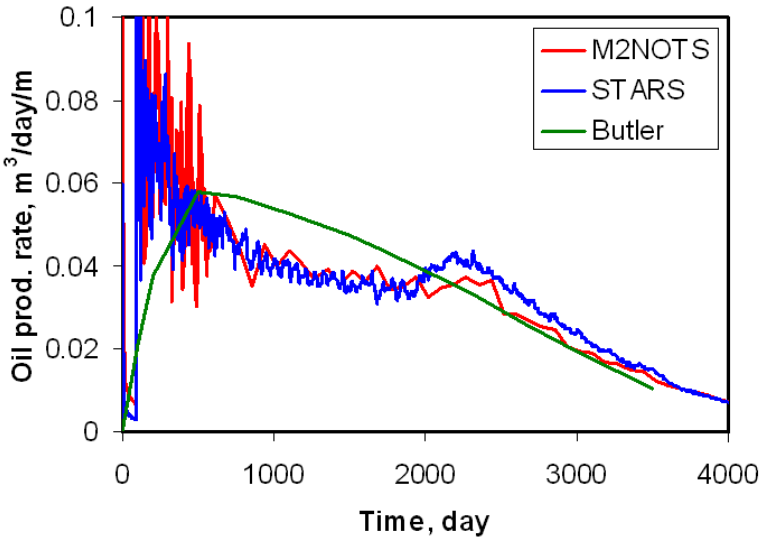

Figure 6.4: Comparison of the oil production rate predicted by Butler's analytical method, STARS, and this work (M^2NOTS).

As seen in Figure 6.4, our simulator gives consistent results with Butler's gravity drainage theory and STARS simulation. The numerical results by STARS and M^2NOTS predict the typical three stages of SAGD production life, *i.e.*, a steam chamber rising period, a plateau production stage, and a depleting production stage due to the boundary effect, while the Butler's theory captures only the steam chamber

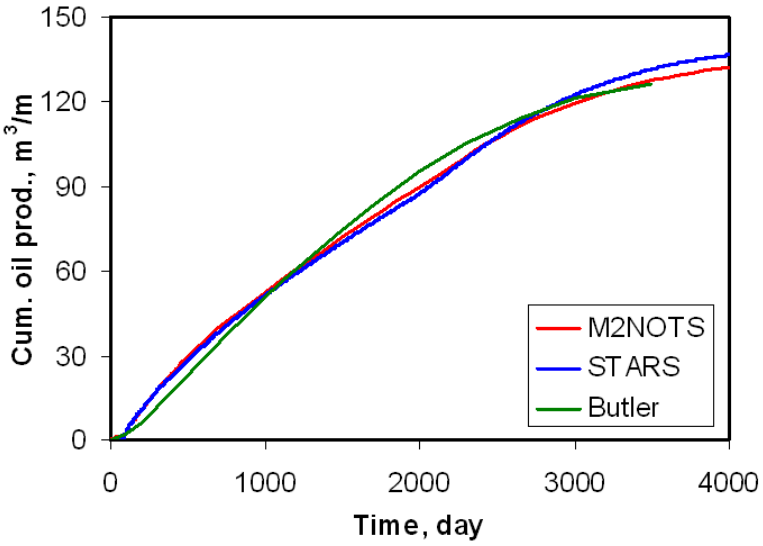

Figure 6.5: Comparison of the cumulative oil production predicted by Butler's analytical solution, STARS, and this work (M^2NOTS).

rising and the declining oil production after reaching a peak when the steam chamber extends vertically to the top of the pay zone. Nevertheless, the magnitude of the three oil production rate curves shows good agreement. It is noticed that the oil production rate curves for STARS and M^2NOTS simulations exhibit considerable oscillations, especially during the early stages of steam injection. This is likely due to frequent phase changes in grid blocks close to the well region. The material balance error in the simulation results, however, was examined and found to be plausible. Therefore, we believe that the simulation results shown in Figure 6.4 are valid. Better agreement is exhibited in Figure 6.5 in which the three curves almost overlap with each other with a maximum error less than 5%.

Figure 6.6 presents four snap-shots of the temperature profiles at 300, 1000, 2000, and 5000 days of steam injection predicted by our own simulator. Those temperature profiles reveal clearly the different production stages in a classic SAGD project. Close comparison of the temperature profiles and other key parameters profiles between the

M^{2}NOTS and STARS simulation results (not shown here) further confirms that our foam simulator is capable of simulating the SAGD-type processes.

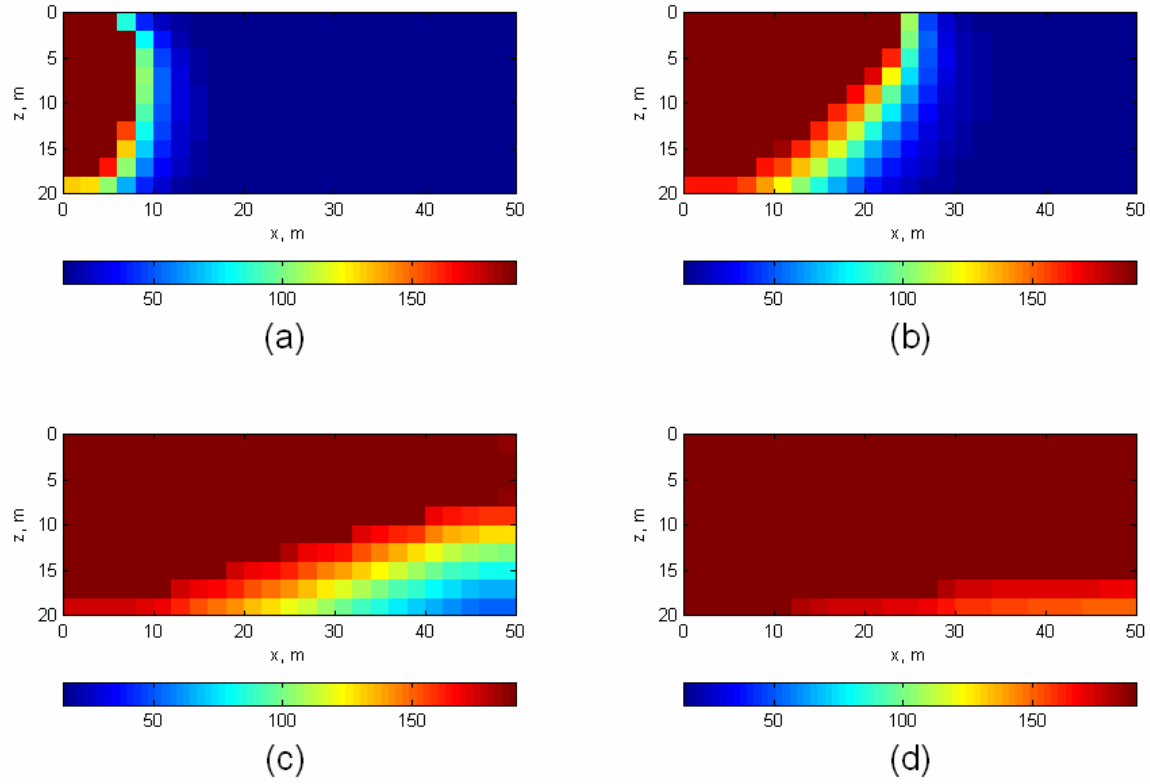

Figure 6.6: Temperature profiles during SAGD at (a) 300, (b) 1000, (c) 2000, and (d) 5000 days. The color bar gives temperature values in unit of °C.

6.4.2 FA-SAGD versus SAGD

Next, we include the option of foam modeling implemented to M^{2}NOTS to simulate the FA-SAGD process. In the simulation runs, the local equilibrium model that was developed and verified in Chapter 5 was used to shorten the CPU time. A maximum bottom hole pressure of 1300 kPa and a constant production pressure of 1200 kPa are set as well controls at the injection well and the production well, respectively. The injected steam has a quality of 0.9 and the liquid portion of the injected steam

contains surfactant concentration of 1.0 wt%.

Figure 6.7 shows the temperature profiles at various stages of the production as a result of coinjecting steam and surfactant solution. The region with temperature equal to the steam temperature corresponding to the pressure lays out the steam chamber. The steam saturation profiles given in Figure 6.7 confirm a bowl-shaped steam chamber developed within the reservoir. Similar to the SAGD process, the steam chamber in the FA-SAGD process experiences rising, expanding, and depleting stages. Notice that, in the steam saturation profiles, the variation of the steam quality within the steam chamber, *i.e.*, dryer steam in the top and wetter steam in the lower portion of the steam chamber, is consistent with the analysis of the steam quality distribution under the gravity effect in a typical SAGD process presented at the beginning of this chapter.

Because of the confinement boundary conditions and thermal expansion caused by the temperature increase, as shown in Figure 6.9, pressure builds up ahead of the steam chamber. The high pressure zone moves outwards as the steam chamber expends and finally disappears. Within the steam chamber, considerable pressure gradients exist around the injection point, indicating the presence of strong foam.

Figure 6.10 presents the foam texture profiles at 300, 1000, 2000, and 5000 days of injection predicted by the numerical simulation. As expected, the steam chamber is filled with steam foam that is generated in-situ and results in the high pressure gradient observed in Figure 6.9. It is worthwhile pointing out that the steam foam texture is not uniform throughout the steam chamber. As seen in Figure 6.10, strong steam foam is created and accumulates mainly in the interwell region. The foam becomes much coarser in the upper portion of the steam chamber. This distribution of foam texture is a result of the steam quality variation due to gravity within the steam chamber. It is also observed that strong foam is generated at the boundary of the steam chamber. Similar phenomena is reported for the one-dimensional coreflood

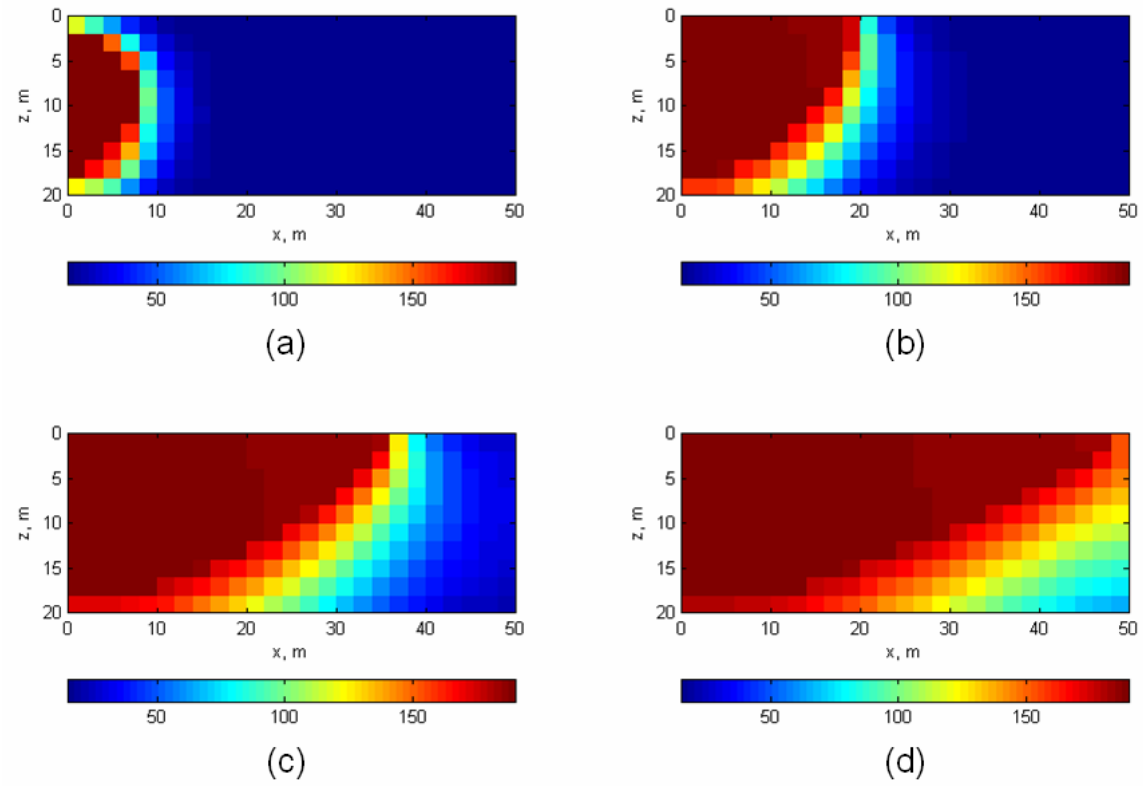

Figure 6.7: Temperature profiles during FA-SAGD at (a) 300, (b) 1000, (c) 2000, and (d) 5000 days. The color bar gives temperature values in unit of °C.

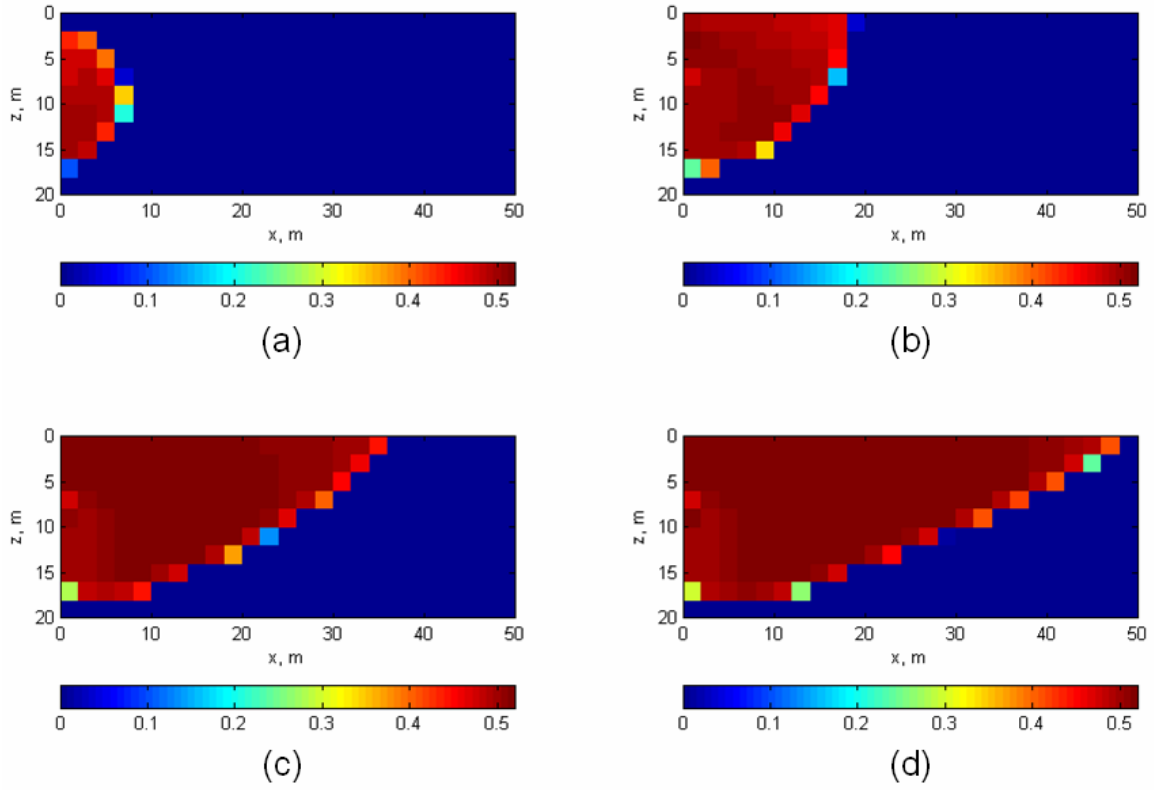

Figure 6.8: Steam saturation profiles during FA-SAGD at (a) 300, (b) 1000, (c) 2000, and (d) 5000 days.

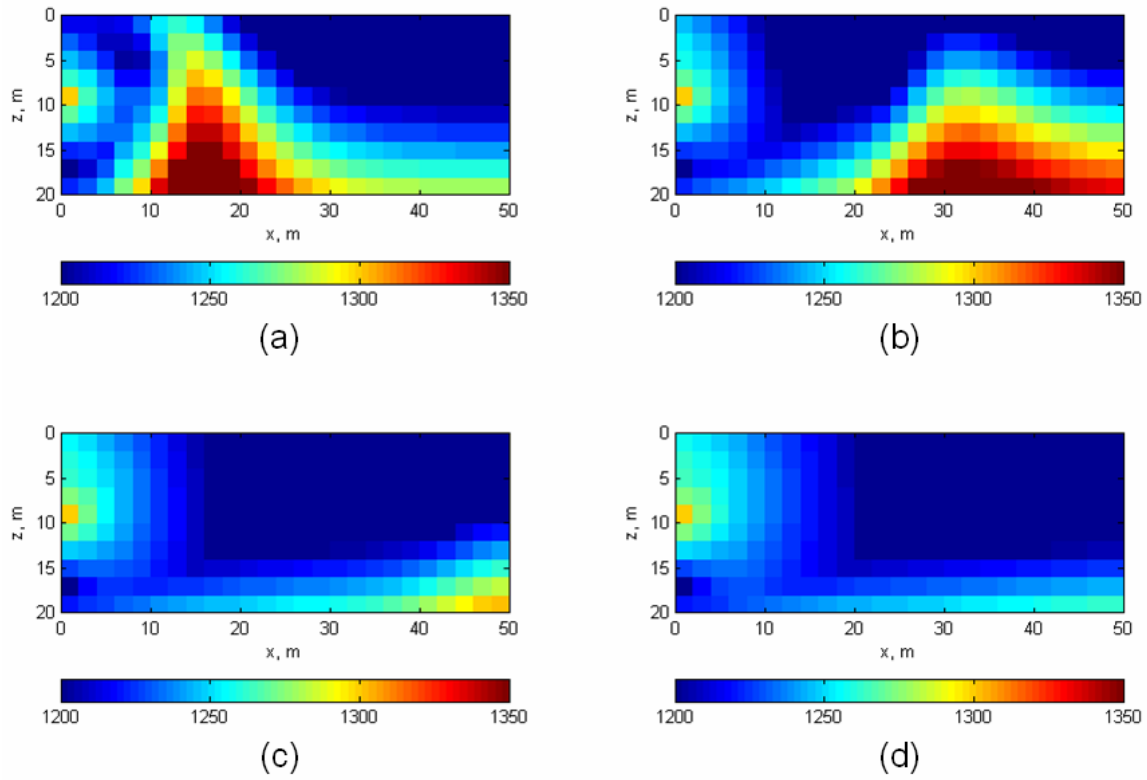

Figure 6.9: Pressure profiles during FA-SAGD at (a) 300, (b) 1000, (c) 2000, and (d) 5000 days. The color bar gives pressure values in unit of kPa.

experiment in Chapter 5 (see Figure 5.14). The fine foam texture at the steam chamber edge is attributed to the net foam generation because of the sharp changes in phase saturations across the boundary.

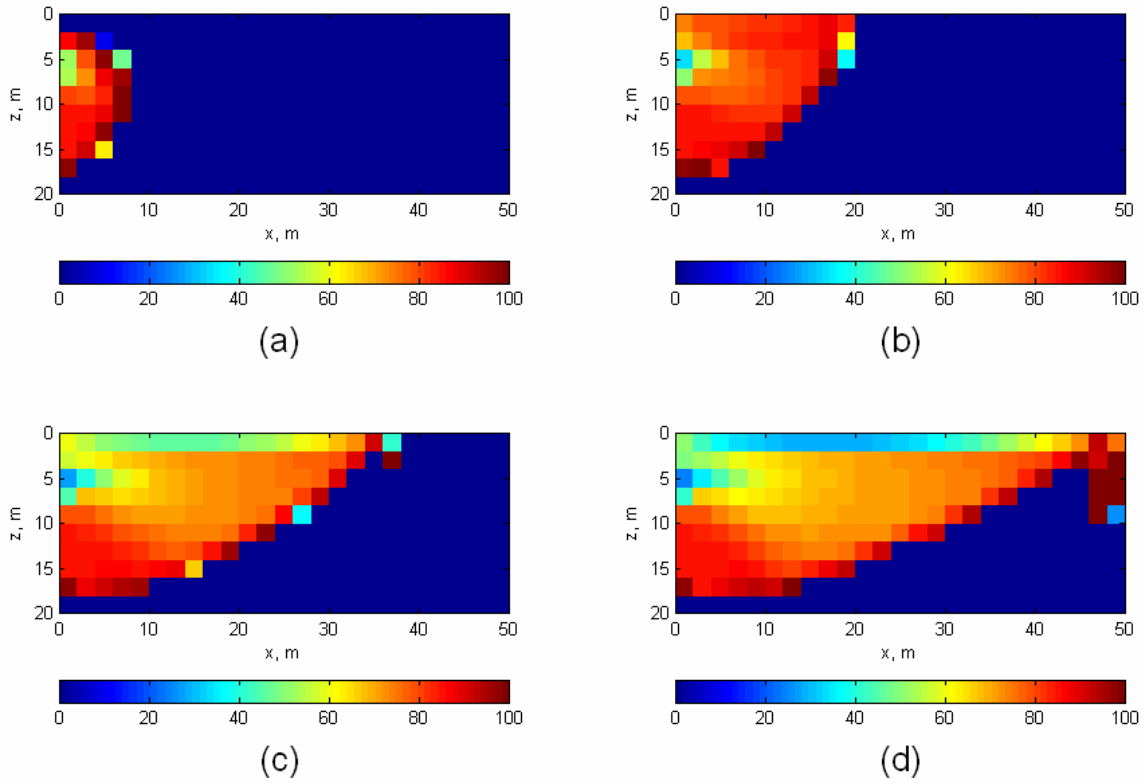

Figure 6.10: Foam texture profiles during FA-SAGD at (a) 300, (b) 1000, (c) 2000, and (d) 5000 days. The color bar gives foam texture values in unit of mm^{-3}.

As seen in Figure 6.11, oil within the steam chamber is depleted efficiently and the remaining oil saturation is close to the residual oil saturation. The water saturation profiles presented in Figure 6.12 show clearly the steam condensation area that is along the boundary of the steam chamber. The condensed water flows together with the heated oil in a manner of cocurrent flow along the slopes of the steam chamber towards the production well. This cocurrent flow contributes to most of the oil production.

A simulation run for the SAGD case that operates at the exactly same conditions

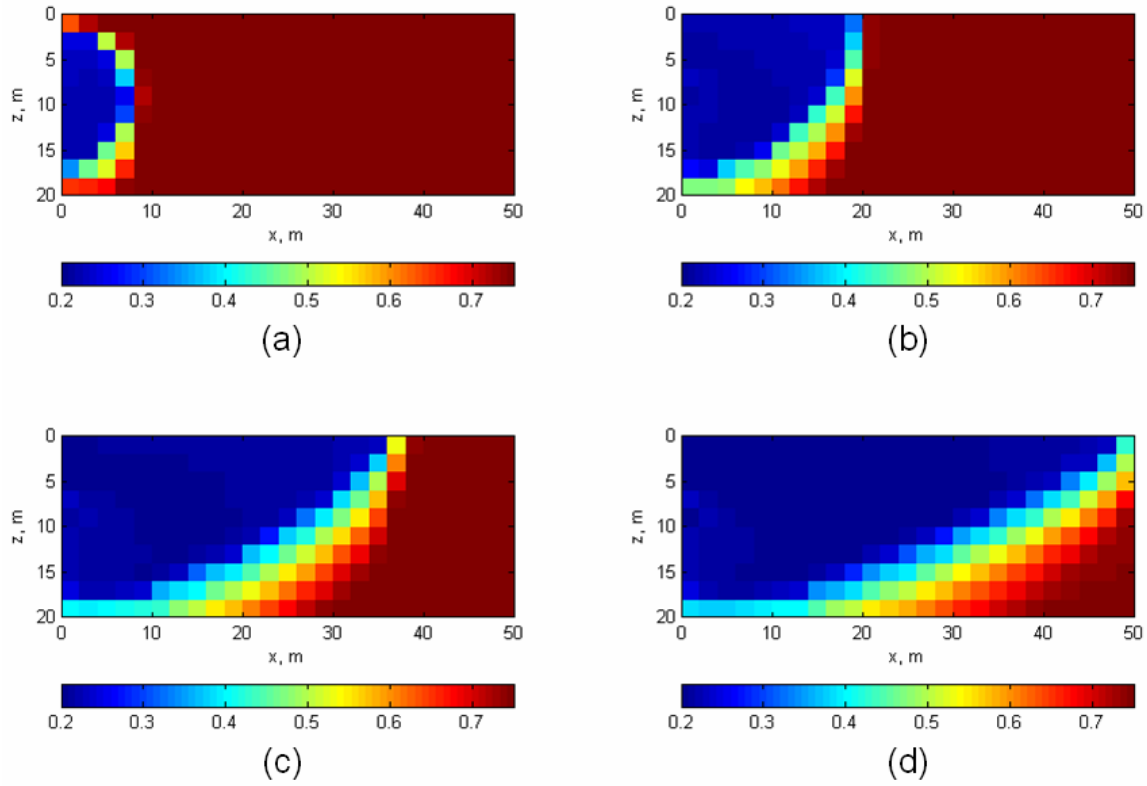

Figure 6.11: Oil saturation profiles during FA-SAGD at (a) 300, (b) 1000, (c) 2000, and (d) 5000 days.

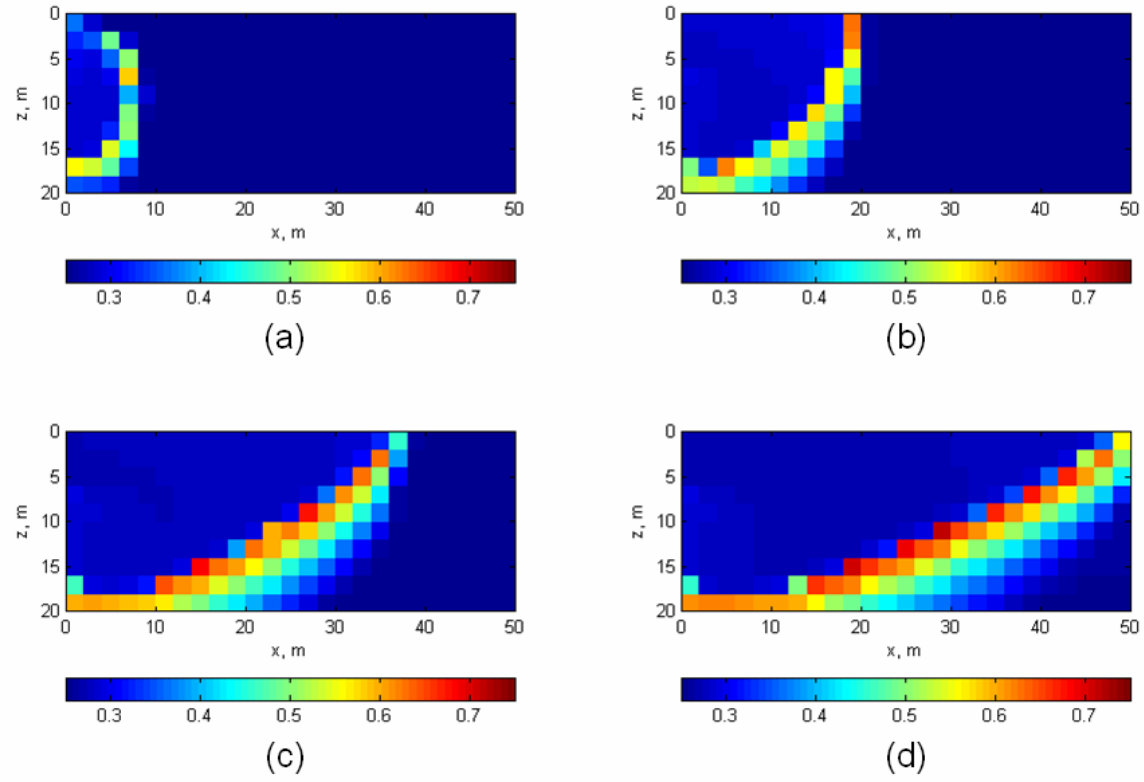

Figure 6.12: Water saturation profiles during FA-SAGD at (a) 300, (b) 1000, (c) 2000, and (d) 5000 days.

as the FA-SAGD case is performed. Figure 6.13 provides a side-by-side comparison of key parameter profiles, including temperature, steam saturation, pressure, and oil saturation, at the same recovery (*i.e.*, 40%) between FA-SAGD and SAGD. Two major differences between FA-SAGD and SAGD are identified from this close comparison. First, FA-SAGD has a more bowl-shaped steam chamber, while the upper front of the steam chamber in the SAGD case extends laterally further, resulting in a flat, plate-shaped chamber. This difference in the steam chamber shape may result in different heat losses to overburden and consequently yielding different energy efficiencies. Theoretically, heat loss to overburden is proportional to the temperature gradient, thermal diffusivity, and the area of contact. The bowl-shaped steam chamber in the case of FA-SAGD has less high temperature area exposing to overburden in comparison to the plate-shaped chamber in SAGD. Hence, FA-SAGD is expected to be more energy efficient. Second, the remaining oil saturation within the steam chamber is lower in FA-SAGD than in SAGD. This happens because the presence of strong steam foam within the steam chamber in FA-SAGD causes high pressure gradients that drive the oil phase to flow even at very low oil saturation close to its residual value. The reduction in the remaining oil saturation increases the final oil recovery factor.

Figure 6.14–6.17 further compare the performance of FA-SAGD and SAGD in terms of oil production rates, steam injection and production rates, and cumulative steam injection versus cumulative oil production.

As shown Figure 6.14, there is not much difference in the oil production rate between SAGD and FA-SAGD in the early stage *i.e.*, for the first 500 days. In the later stage, however, the oil production rate curve for FA-SAGD is lower than that of SAGD until the SAGD case proceeds to depleting production due to the boundary effect.

Countercurrent flow exists in the early stage of steam chamber expansion, whereas

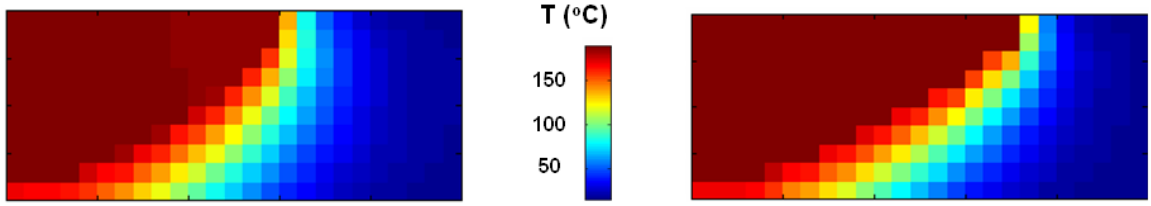

(a) Temperature

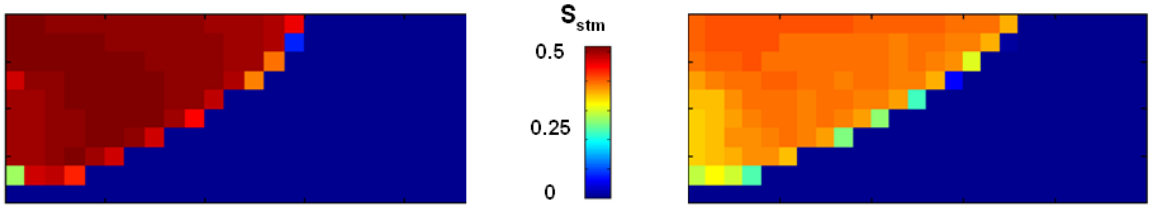

(b) Steam saturation

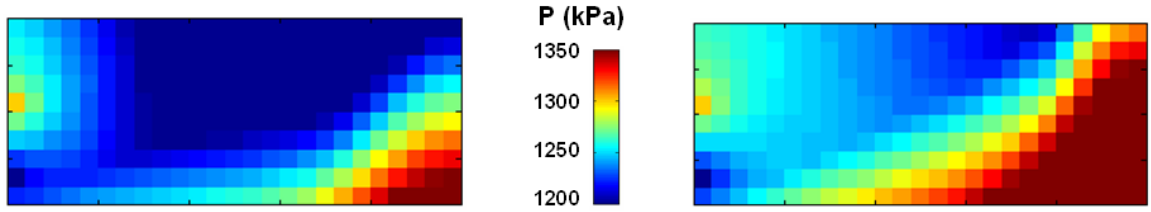

(c) Pressure

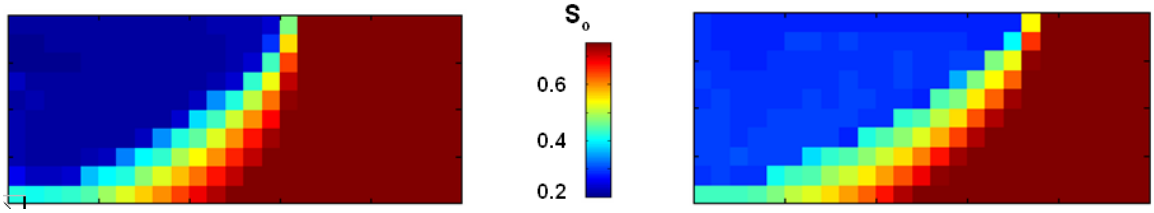

(d) Oil saturation

Figure 6.13: Comparison of FA-SAGD and SAGD: (a) temperature, (b) steam saturation, (c) pressure, and (d) oil saturation. The profiles on the left column are for FA-SAGD and the ones on the right column are for SAGD.

cocurrent flow remains at the boundary of steam chamber through the process. When steam and surfactant solution are coinjected, steam foam is generated mainly in the steam-water zone. In front of the steam condensation zone along the slope of the steam chamber where cocurrent flow occurs and is responsible for the main oil production, no foam or weak foam is expected because of the lack of gas phase saturation and the presence of the oil phase. Therefore, no impact on cocurrent flow and on the oil production is expected throughout the process during FA-SAGD process. During the early stage of the process, the hot oil in the ceiling of the steam chamber is held by the generated foam and is forced to the boundary and produced by cocurrent flow. Since the cocurrent flow contributes the main portion of oil production, the effect of foam on the countercurrent flow is likely to be negligible.

The unexpected reduction in the oil production rate for FA-SAGD observed in Figure 6.14 is attributed to the mobility reduction of the vapor phase due to the presence of steam foam. Gravity drainage processes rely mainly upon the drive of the gravity that causes lighter fluids to move upward and heavier fluids downward. The potential is normally determined by the density difference between steam and liquid phases. In the FA-SAGD case, because steam moves through the steam chamber in the form of steam foam, it has a much greater effective viscosity. The resultant reduction in steam mobility increases the energy requirement to drain oil downward, and consequently causing a reduction in the oil production rate. This is a negative effect of foaming steam in the FA-SAGD process.

Nonetheless, foaming steam has a positive impact on controlling live steam production in the FA-SAGD process. The steam injection rate, as shown in Figure 6.15, is almost doubled in SAGD compared to FA-SAGD. A significant portion of the injected steam is directly produced in SAGD (Figure 6.16). On the other hand, the steam production rate in FA-SAGD at the same operation conditions is much less

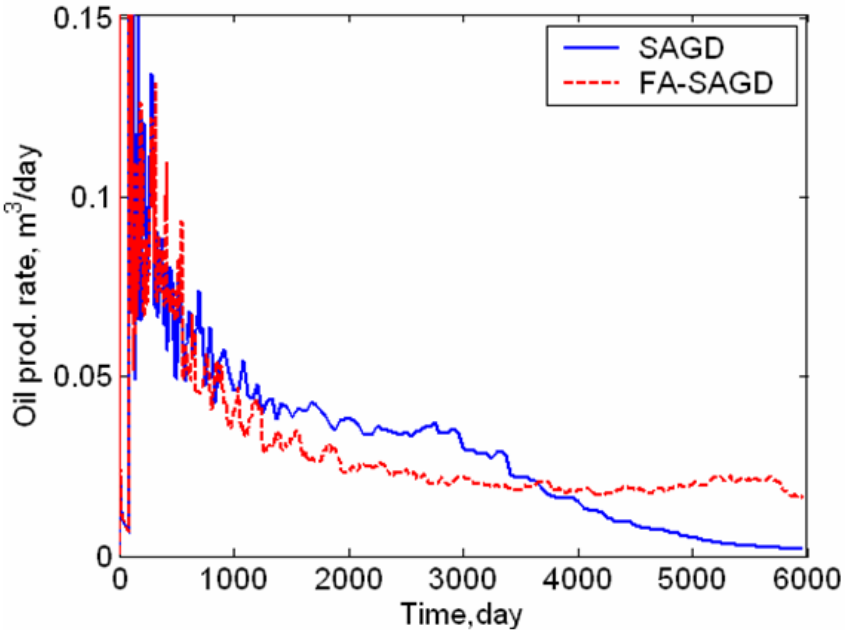

Figure 6.14: FA-SAGD versus SAGD: oil production rate as a function of time

than that of SAGD because of strong steam foam generated in between the injection and production wells. The presence of steam foam effectively reduces live steam flow from the injector to the production well and thereby improving the recovery performance in terms of energy efficiency.

The improvement of FA-SAGD over SAGD with respect to the energy efficiency is more obvious in the plot of cumulative oil production versus cumulative steam injection, as shown in Figure 6.17. The slope of the curves in Figure 6.17 gives an indication of the process energy efficiency. The steeper the slope, the more energy efficient the process is. In addition, the end point of each curve tells the final oil recovery. As seen in Figure 6.17, for the same amount of produced oil, the required amount of steam in FA-SAGD is less than half of that in SAGD. As pointed out previously, this is mainly due to the presence of strong steam foam in the interwell region that provides effective blockage to steam flow from the injection well to the production well.

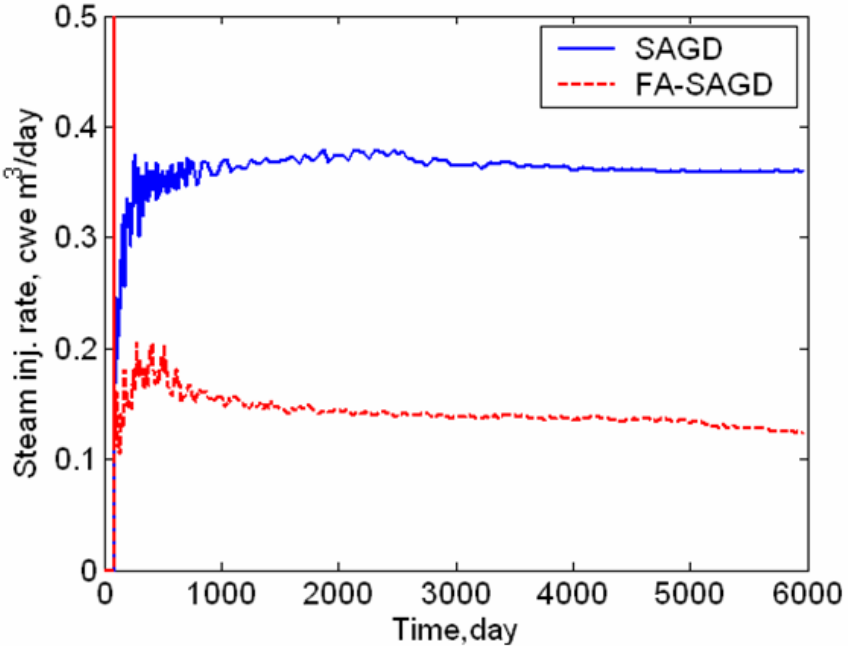

Figure 6.15: FA-SAGD versus SAGD: steam injection rate as a function of time.

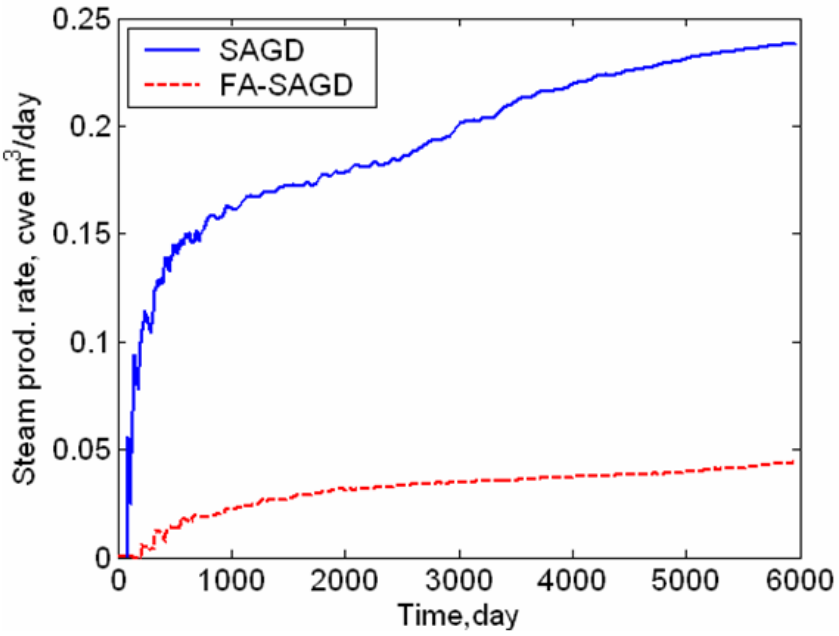

Figure 6.16: FA-SAGD versus SAGD: steam production rate as a function of time. FA-SAGD.

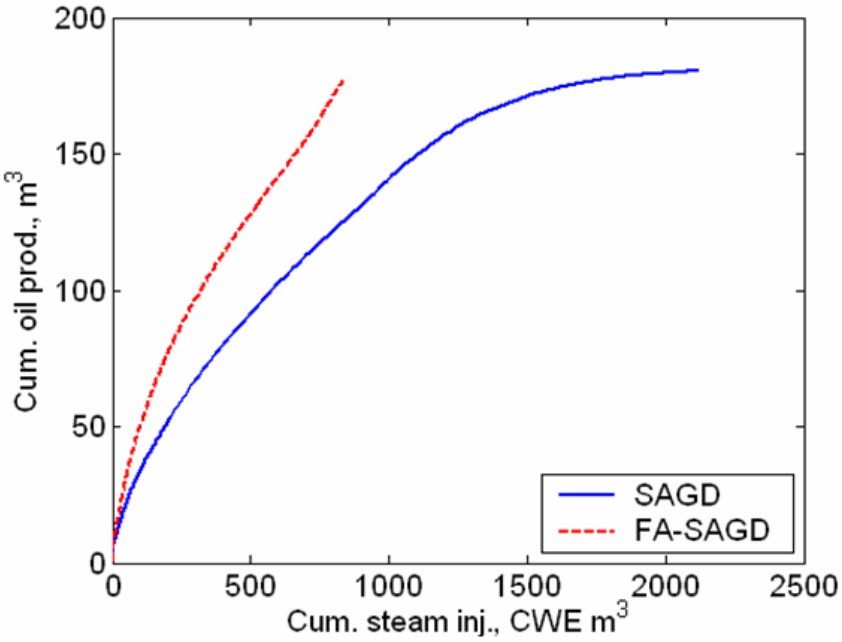

Figure 6.17: Comparison of the process efficiency between SAGD and FA-SAGD: cumulative steam injection versus cumulative oil production.

6.5 Concluding Remarks

This chapter examines the idea of FA-SAGD as a potentially improved alternative to the conventional SAGD process. We lay out the concept of FA-SAGD in detail and discuss additional code development required to model FA-SAGD processes. The verification of the capability of the recently-developed foam simulator for SAGD-type simulation is achieved by comparing the results from our own simulator to Butler's analytical solution and STARS numerical solution. Both SAGD and FA-SAGD are simulated successfully. It is found that strong steam foam is generated and accumulates in the interwell region. The presence of strong steam foam helps control steam breakthrough and therefore yielding better performance in comparison to SAGD. The presence of steam foam in the upper portion of the steam chamber reduces the gas phase mobility, which results in a reduction in the oil production rate. Still, FA-SAGD

provides better overall performance than SAGD. Although this work was limited to two-dimensional simulation, we anticipate an exciting and promising research area for a potential alternative to SAGD. There are many questions to be answered by future work as discussed later in Chapter 7.

Chapter 7

Conclusions and Future Directions

This dissertation addressed the role of reservoir heterogeneities on SAGD performance and proposed two approaches, hydraulic fracturing and deployment of aqueous foams, to improve the conventional SAGD process in heterogeneous reservoirs. To assess the impacts of foaming the steam phase, we also developed a numerical model for foam that is incorporated into a standard reservoir simulation framework for reproducing and predicting foam flow behaviors through porous media. In this chapter, we summarize this research and make recommendations for future research directions.

7.1 Conclusions of the Present Work

A numerical investigation of the role of reservoir heterogeneity on the success of the SAGD process was reported. SAGD performance was assessed by performing reservoir simulation with heterogeneous reservoirs whose properties are populated by including a distribution of shaly sands with a stochastic representation based on a geostatistical method. The main conclusions are summarized next.

- According to characteristic flow length, two flow regions, the near well region

(NWR) and the above well region (AWR), are identified for decoupling successfully the complex effect of reservoir heterogeneity on the SAGD process.

- The drainage flow of hot fluids within the NWR is of short characteristic length and is found to be very sensitive to the presence of shale. Significant variations in the oil production rate (*e.g.*, from 900 bbl/day to 300 bbl/day) and the cumulative oil steam ratio (*e.g.*, from 0.2 to 0.3 bbl oil/bbl CWE steam) are observed with a moderate change to the shale distribution within the NWR (*e.g.*, denser and more continuous shale). Therefore, it is recommended that horizontal well pairs be placed in the high quality region (less shale) of a formation in practice to optimize SAGD performance.

- The AWR affects mainly the vertical and horizontal expansion of the steam chamber that is of characteristic flow length on the order of half of formation height. The SAGD performance is insensitive to the presence of short, discontinuous shale barriers in the AWR, while it is affected adversely, *e.g.*, a reduction in the oil production rate by 60%, when the AWR contains long, continuous shale or a high fraction of shale.

For reservoirs with poor vertical communication due to the presence of shale or other low permeability layers, we proposed hydraulic fracturing to accelerate steam chamber growth and consequently oil production in a conventional SAGD process. Potential improvement of SAGD performance by hydraulic fracturing was studied numerically. The following conclusions are drawn from this investigation:

- The orientation of hydraulic fractures generally depends on the depth of the formation of interest. Fractures are usually horizontal for shallow SAGD projects and vertical direction for deep SAGD projects.

- It was found that vertical hydraulic fracturing improves well injectivity dramatically to achieve an economical oil production rate in a SAGD process for reservoirs with poor vertical communication. Examination of the temperature profiles predicted by simulation indicates that a vertical hydraulic fracture accelerates significantly steam chamber growth vertically. For the synthetic reservoir studied in this work, adding a vertical fracture along the well direction lifts the oil production rate approximately by a factor of two, *i.e.*, from 300 bbl/day to 600 bbl/day, and the cumulative oil-steam ratio increases from 0.2 to 0.3 bbl oil/bbl CWE steam. Therefore, hydraulic fracturing may be desired especially for deep SAGD projects.

- We also found that a vertical hydraulic fracture along the well direction is superior to a fracture perpendicular to the well direction with respect to oil recovery. The field practice that a horizontal well is drilled along the direction of maximum horizontal stress to ensure well stability coincides with the requirement of vertical hydraulic fractures parallel to the well direction.

Moreover, a novel concept of FA-SAGD was proposed for better recovery performance in comparison to the conventional SAGD, especially for heterogeneous reservoirs. This study comprised two parts: development of comprehensive, efficient foam models and numerical evaluation of the FA-SAGD process.

In the first part, we conducted experimental and numerical investigations of foam flow in porous media. We proposed foam texture dependency of foam generation by snap-off to extend the previous population balance model to reproduce steady state foam behaviors in the low-quality and high-quality regimes. A simplified population-balance model with the local equilibrium approximation was developed for simulating foam processes. Experiments of steady-state and transient foam flows were conducted

with a one-dimensional, linear core to verify our new models quantitatively. In addition, the local equilibrium model was applied to simulate a one-dimensional, radial foam flow at the field scale. The following conclusions have been derived:

- The modified population balance model with foam texture dependency of foam generation predicts successfully the steady-state pressure gradient trend in the low-quality and high-quality regimes as well as a smooth transition in between.

- Experimental estimates of in-situ foam texture is achieved with a visualization cell for a steady-state foam flow. The measured mean foam texture of 400 mm^{-3} or a mean bubble diameter of 170 μm for a strong foam inside the Berea sandstone core (K = 0.3 μm^2 and $\phi = 0.18$) is consistent with the literature. The profile of measured foam texture shows that the entrance region required for foam texture to reach local equilibrium is shorter than 12 cm for the case under study and that foam generation and decay balance throughout the majority portion of the core. These observations support the assumption of local equilibrium as an approximation for foam modeling in the proposed local equilibrium.

- A local equilibrium bubble population balance model has been derived with foam texture dependency of foam generation and the assumption of local equilibrium for modeling foam displacement in porous media. The local equilibrium model is capable of predicting the steady-state foam behaviors in low-quality and high-quality regimes. Also, the numerical predictions of the local equilibrium model for two transient foam coreflood experiments, one with constant surfactant concentration and the other with transient surfactant concentration, are in good agreement with both the full physics model and experimental results. Only a slight mismatch in the entrance region due to net foam generation

is found. Moreover, the local equilibrium model is shown to be applicable to model radial foam flow at the field scale.

- The local equilibrium model is more efficient in term of computational cost in comparison to the full physics model. A speed-up factor more than two by the local equilibrium model compared to the full physics model is observed. In summary, the local equilibrium model appears to be an effective tool for foam modeling, especially for field-scale applications.

With the recently-developed foam models implemented into a nonisothermal, compositional reservoir simulation framework, we simulated and evaluated the FA-SAGD process as a potential method to improve the SAGD performance. The following conclusions have been obtained:

- Coinjecting steam and surfactant solution in FA-SAGD results in strong foam accumulated in the interwell region and relatively weak foam in the upper portion of the steam chamber. The resultant steam chamber shape becomes more bowl-like as compared to that in SAGD.

- The presence of steam foam within the steam chamber decreases the mobility of steam and thereby impairs the gravity drainage. A reduction in the oil production rate is observed in FA-SAGD during the production plateau in comparison to SAGD.

- FA-SAGD exhibits better energy efficiency than SAGD due to the existence of strong steam foam within the interwell region. The increased flow resistance because of the presence of strong foam between the wells delays steam breakthrough and reduces the amount of live steam produced at the production well.

7.2 Directions for Future Research

Some possibilities and suggestions for improving the present study as well as for future research directions are outlined below.

7.2.1 Gas Trapping Model

At present, foam trapping was implemented simply with a constant factor or a simple function of foam texture. The fraction of trapped foam, however, depends upon not only foam texture, but also other variables. Recently, Tang and Kovscek (2006) measured the flowing gas fraction of an aqueous foam at steady state and concluded that the trapped gas fraction is a weak function of pressure gradient, foam-bubble size and the permeability of the porous medium. They also derived an expression for the fraction of foamed gas that is mobile, as follows

$$X_f = \frac{\psi}{S_g}\left[\frac{f_c|\nabla p|}{k^{1/2}n_f}\right]^{\eta} \quad , \tag{7.1}$$

where ψ is a constant of proportionality, f_c is the percolation fraction, and η is a percolation exponent constant. From their recently-obtained experimental data, Tang and Kovscek (2006) determined the parameter values of $\psi = 1.4$, $\eta = 0.4$, and $f_c = 0.25$ for strong foam flow through porous media where gas is largely immobile. Eq. (7.1) is a closed form expression for the fraction of mobile gas within aqueous foam in sandstone that is directly employable in population balance simulators of foam dynamics. Implementation of this foam-trapping expression into the current foam model is expected to increase the model capability and provide more accurate prediction of foam behaviors. Nevertheless, cautions should be taken when applying such implementation for modeling transient foam flow, as Eq. (7.1) was obtained only with steady-state flow data. Further experimental measurements of the trapped gas

fraction in a wide range of flow conditions are necessary to reaffirm the validity of Eq. (7.1) or to propose new expressions for the trapped gas fraction. A more complete understanding of the foam trapping mechanism will contribute to accurate predictions of foam dynamics.

7.2.2 Snap-Off Generation Model: $k_1(n_f)$ Function

To address the dependency of active foam generation sites on the pre-existing gas bubbles during the snap-off process, we introduced a foam generation coefficient, k_1, as a function of foam texture, n_f in Chapter 5. The function of $k_1(n_f)$, as seen in Eq. (5.2), implies that k_1 reduces as n_f increases. The parameter, ω, in Eq. (5.2) determines the shape of the function. The choice of the parameter value $\omega = 3$ used for modeling various foam flow experiments in Chapter 5 is arbitrary rather than based on any experimental data. As shown in Appendix B, varying the parameter ω, from 0.5 to 1, 2, and 3, results in noticeable changes in the numerical predictions. It is believed that the shape of the $k_1(n_f)$ function depends mainly upon the distribution of pore sizes within a rock in which foam generation occurs. Therefore, the parameter value of ω should be determined experimentally for a rock of interest to provide a more accurate function of $k_1(n_f)$ for foam calculation.

Here, we suggest conducting a series of steady-state foam flow experiments at various injection conditions. For example, fix the gas velocity at 1.125 m/d and vary the liquid velocity from 0.0125 to 1.25 m/d, yielding a gas fraction in range of 99% to 47%. With the experimental setup described in Chapter 5, we can easily measure the corresponding pressure drops across the core and texture of effluent foam bubbles. Figure 7.1 and Figure 7.2 give the pressure drops and average foam textures predicted by the local equilibrium model with different parameter values of ω, *i.e.*, different shapes of the k_1 function, for steady-state foam flows. Direct comparison of experimental data and numerical predictions will lead to an estimation of the

parameter value of ω for the snap-off generation function.

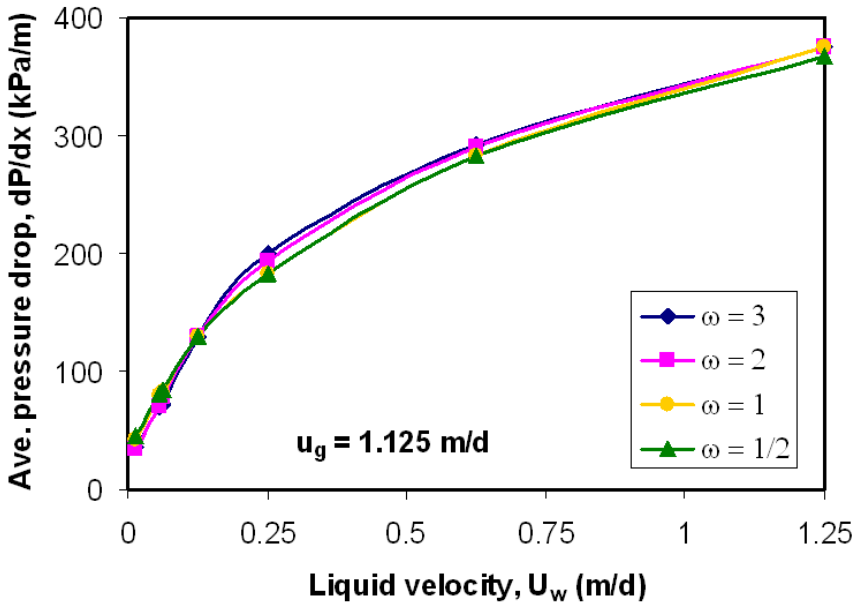

Figure 7.1: Sensitivity of calculated average pressure drop with variation of foam generation rate constant.

7.2.3 Three-Dimensional Simulation of FA-SAGD

In the present work, simulations of FA-SAGD were limited to a two-dimensional, vertical cross section due primarily to a slow computation speed of the current foam simulator. With improvement on numerical performance of the foam simulator and sufficient computation resources in the future, three-dimensional simulations of FA-SAGD need to be performed to advance our understanding of the physics mechanisms associated with the FA-SAGD process. For instance, injecting steam foam instead of steam into reservoirs is likely to reduce the effect of heterogeneity along the horizontal wellbore on the steam injection profile and consequently more uniform steam chamber growth is achieved along the whole well length. Such advantages of FA-SAGD over conventional SAGD need to be demonstrated by three-dimensional simulations in a

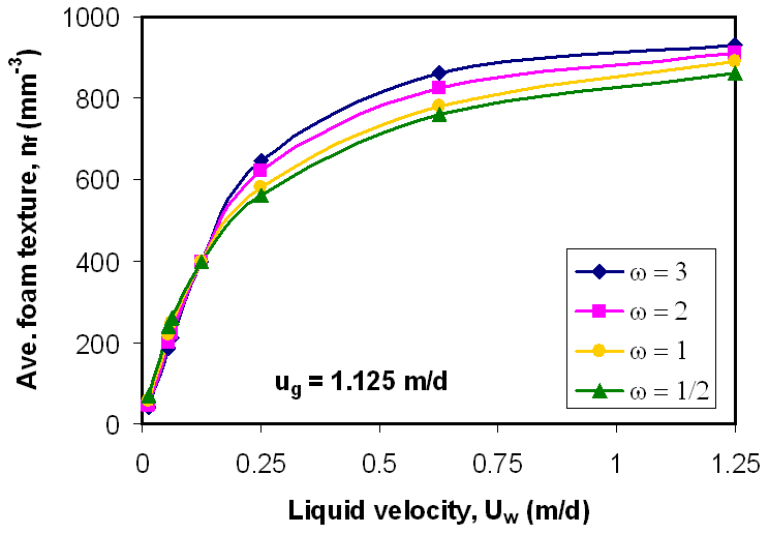

(a)

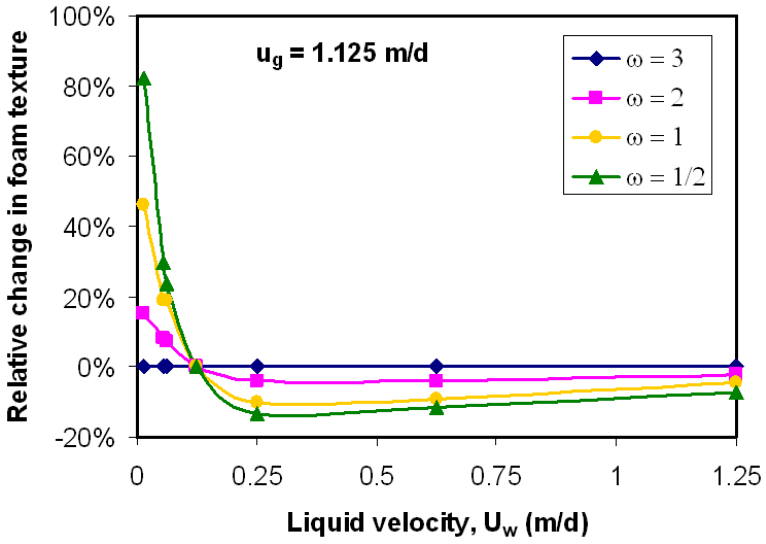

(b)

Figure 7.2: Sensitivity of calculated foam texture with variation of foam generation rate constant: (a) average value and (b) change in average in percentage relative to the case $\omega = 3$.

heterogeneous setting.

7.2.4 Experimental Evaluation of FA-SAGD

The proposed FA-SAGD process was studied in this work mainly from a numerical perspective. An experimental investigation of FA-SAGD is an indispensable complement to the current study and presents to be a promising research area to explore for future work. There are several key questions to be addressed experimentally, including which surfactant to be used, what values the model parameters are for the particular type of surfactant, how to construct three-dimensional sandpack models for FA-SAGD lab runs, etc. Accordingly, the future investigation can be divided into several phases.

In the first phase, a series of surfactant screening tests need to be conducted to find suitable surfactants capable of generating foam at steam temperature, *e.g.*, 220°C, in the presence of oil, and in the presence of formation brine. This search can start with the commercially available chemicals reported in the literature. Ideally, the steam foam should generate within the reservoir only in those regions that have been swept by the steam to some residual oil saturation. The foams should therefore be stable in the presence in relatively small amounts of oil, but should collapse at higher saturations. The foam should be stable over the range of temperatures and pressure encountered in the field. Surfactant retention by, and ion exchange with, the reservoir sands should be minimized where possible. According to those criteria, the number of surfactant candidates should be narrowed down to two or three.

Next, surfactants that pass the screening test are examined extensively with experiments that consider foam generation and gas diversion in porous media. The experiments are carried out at elevated temperature by injecting saturated steam laden with aqueous surfactant. The experimental setup described in Chapter 5 can be used for this test with minor modifications, *e.g.*, adding thermocouples along the

core for monitoring temperature changes. The propagation of steam through the core is monitored using X-ray computed tomography to image the in-situ phase saturations and the pressure drop along sections of the core is recorded by pressure transducers mounted to the core holder. In this way, various surfactants are screened for their tolerance to elevated temperature. Also, foam displacement data is collected that is useful to determine model parameters for modeling.

In the third phase, a three-dimensional sandpack model with appropriately scaled geometries and properties is designed and constructed to mimic the processes of SAGD and FA-SAGD at the laboratory scale. In the experiments, the temperature profile within the sandpack is monitored with distributed thermocouples. An X-ray CT scanner is used to track the development of steam chamber or/and foamed gas. In the mean time, corresponding simulations are used to match and interpret the experimental results and observation.

7.2.5 Is FA-SAGD the Key to Carbonate Reservoirs?

Previous SAGD research has focused mainly on oil sand and little attention has been paid to bitumen carbonates until very recently as a result of the high oil price and continuously declining discovery of conventional oil resources (Alvarez et al., 2008; Das, 2007). According to the EUB 2005 publication, bitumen resources of 71.1×10^9 m^3 (more than 400 billion bbl) of OBIP is found in the Devonian and Carboniferous carbonate rocks located beneath the Alberta oil sand formation. Recovery of bitumen from these huge carbonate resources, however, represents a great challenge from both technical and economical standpoints. Carbonate reservoirs in Western Canada are normally characterized with extraordinarily viscous oil and extremely high heterogeneity. The oil contained in the carbonate rocks is completely immobile, with viscosity higher than 1.0×10^6 cp at reservoir conditions. In general, those reservoirs are naturally fractured, composed of low permeability matrix ($\sim$ 10 mD), partially

dolomatized and karsted (Buschkuehle et al., 2007). Applications of SAGD to carbonate reservoirs appear to be problematic. One of the main issues is the loss of steam confinement due to the presence of long extended fractures or karsts that often provide high permeability channels for steam to escape. Secondly, avoiding live steam production is difficult to achieve during SAGD operations in naturally fractured carbonate reservoirs. In those reservoirs, the injection and production wells are likely penetrated by the same naturally-existing fractures that impair the effectiveness of steam trap control and make the process economically challenging.

The concept of FA-SAGD proposed in this work, on the other hand, may be a potential alternative to SAGD for exploiting the bitumen carbonates. As demonstrated in this work and elsewhere, foaming steam in place creates an effective blockage in the highly permeable regions (*e.g.*, fractures or karsts) that would otherwise become primary conduits for flow, resulting in early breakthrough or loss of confinement. This selective blockage effect of steam foam not only provides necessary confinement to trap steam within the reservoir, but also helps mitigate the difficulty in preventing live steam production. In the latter case, if the injection and production wells are connected by a fracture or karsted formation (highly permeable), strong steam foam will be preferentially generated and accumulated in the interwell region because of favorable foam creation conditions, *i.e.*, low steam quality due to gravity and large flow velocities due to high permeability. The resultant high flow resistance imposed by foamed steam minimizes or even stops steam flow into the production well without affecting the warm oil and condensate flowing along the steam chamber slopes. One concern of applying steam foam to carbonates, however, is that Ca^{++} dissolved into the aqueous phase from carbonate rocks tends to destabilize foam. Therefore, special surfactants may be needed. Nevertheless, with suitable foamer agents, steam confinement in carbonate reservoirs may be readily achieved during the FA-SAGD process, leading to a successful recovery. FA-SAGD for carbonate bitumen recovery

deserves research attention and should be explored in the future research work.

Appendix A

Reservoir Simulation Model Details

A.1 Example of STARS Input File for SAGD Simulation

```
**  ==============  Overview  ======================
**  SAGD simulation featured with:
**  1)  2D - Cartesian
**  2)  Horizontal wells
**  3)  Compositional treatment of oil and gas phases.
**  4)  Automatic initial vertical equilibrium calculation.

**  ==============  INPUT/OUTPUT CONTROL  ======================
*interrupt *stop
*title1 'Athabasca-Type Reservoir'
*title2 'SAGD Operation with Steam Trap Control'
*title3 'Homogeneous Reservoir Properties'
```

```
*INUNIT *FIELD
*OUTPRN *WELL *ALL
*OUTPRN *GRID *NONE
*OUTPRN *ITER *NEWTON
*WPRN *GRID 200
*WPRN *ITER 200
*PRNTORIEN 2 0
*WPRN  *SECTOR 100
*WSRF  *SECTOR 100
*OUTSRF *SPECIAL
        *MATBAL  WELL 'C20_35'  ** Cumulative oil production
        *MATBAL  WELL 'WATER'   ** Cumulative water production
*OUTSRF *GRID *PRES *SW *SO *SG *TEMP *QUALBLK *CCHLOSS
        *VISO *MOLDENO *MASDENO *MASDENW *FLUIDH *THCONDUCT

**  ==============  GRID AND RESERVOIR DEFINITION  =================
*GRID *CART  67 1 20
*KDIR *DOWN
*DI *IVAR 33*4.92 1*3.28 33*4.92   ** 328 ft(100 m) total
*DJ *con 3280.84             ** 3280.84 ft (1000 m) total
*DK *con 3.28                    ** 65.62 ft (20 m) total
*DEPTH  1 1 1 984.25   ** Reservoir depth at pump 300 m.
*POR  *con 0.32
*PERMI *con 3000
*PERMJ *EQUALSI
*PERMK *EQUALSI * 0.6              ** Kv/Kh = 0.6
*END-GRID  ** Announce Stars definition of the reservoir done

** ======= Reference pressure for the rock compressibility ========
```

```
*PRPOR 14.6
*ROCKTYPE 1
*CPOR 5e-4
*ROCKCP 35
*THCONR 106
*thconw 8.6
*thcono 1.8
*thcong 1.2
** Heat loss to overburden and underburden
*HLOSSPROP *OVERBUR 35.07 24.01 *UNDERBUR 35.07 24.01
*HLOSST 50      ** Init. temperature of over/underburden (oF)
*HLOSSTDIFF 10  ** Limit of T difference for heat loss cal. (oF)
*THTYPE *CON 1

**  ==============  FLUID DEFINITIONS  ================================
**--Generated by Winprop "Stars PVT simulation"
MODEL  6  6  6 **  6 components, with water (default) first COMPNAME
        'WATER'      'C1'    'C2 toC14'  'C20_35'   'C36+'      'C3'
**      --------   --------   --------   --------   --------   --------
  CMM     0.0000    16.0400   220.5230   554.5500  1060.0000    44.0970
  PCRIT      0.00     667.62     288.87     157.99      94.77     615.76
  TCRIT      0.00    -116.63     725.56    1073.07    1507.67     205.97
  KV1    0.000E+0   1.542E+5   5.746E+5   2.085E+6   8.907E+6   3.002E+5
  KV2    0.000E+0   0.000E+0   0.000E+0   0.000E+0   0.000E+0   0.000E+0
  KV3    0.000E+0   0.000E+0   0.000E+0   0.000E+0   0.000E+0   0.000E+0
  KV4         0.0    -1867.0    -9002.3   -14542.1   -22527.7    -4119.9
  KV5        0.00    -459.67    -459.67    -459.67    -459.67    -459.67
  MOLDEN 0.00E+0  1.074E+00  2.624E-01  1.179E-01  5.602E-02  7.347E-01
  CP     0.00E+0  6.280E-05  8.425E-06  3.094E-06  2.391E-06  3.628E-05
```

```
  CT1    0.00E+0  2.085E-03  3.526E-04  1.389E-04  7.282E-05  1.284E-03
 VISCTABLE
** T, oF  'WATER'     'C1'    'C2 toC14'   'C20_35'     'C36+'       'C3'
**         ------    --------   --------    --------    --------     --------
   50.000  0.E+00  8.3409E+02  3.5938E+03  7.9816E+03  2.7011E+04  1.5495E+03
  103.571  0.E+00  9.6654E+01  3.6476E+02  7.2077E+02  2.0548E+03  1.7264E+02
  157.143  0.E+00  2.1894E+01  7.4059E+01  1.3287E+02  3.2875E+02  3.7860E+01
  210.714  0.E+00  7.6664E+00  2.3653E+01  3.9128E+01  8.5947E+01  1.2900E+01
  264.286  0.E+00  3.5936E+00  1.0252E+01  1.5826E+01  3.1410E+01  5.9082E+00
  317.857  0.E+00  2.0569E+00  5.4842E+00  7.9766E+00  1.4505E+01  3.3146E+00
  371.429  0.E+00  1.3520E+00  3.3987E+00  4.6933E+00  7.9087E+00  2.1411E+00
  425.000  0.E+00  9.7832E-01  2.3354E+00  3.0811E+00  4.8556E+00  1.5258E+00
  478.571  0.E+00  7.5735E-01  1.7269E+00  2.1881E+00  3.2497E+00  1.1652E+00
  532.143  0.E+00  6.1306E-01  1.3419E+00  1.6400E+00  2.3103E+00  9.3186E-01
  585.714  0.E+00  5.1066E-01  1.0775E+00  1.2750E+00  1.7127E+00  7.6782E-01
  639.286  0.E+00  4.3744E-01  8.9293E-01  1.0262E+00  1.3207E+00  6.5130E-01
  692.857  0.E+00  3.5347E-01  7.0019E-01  7.8364E-01  9.7011E-01  5.2163E-01
  746.429  0.E+00  2.8212E-01  5.4376E-01  5.9405E-01  7.0982E-01  4.1297E-01
  800.000  0.E+00  2.1805E-01  4.0987E-01  4.3800E-01  5.0668E-01  3.1682E-01
 PRSR   14.696 ** reference pressure, corresponding to the density
 TEMR   60.000 ** reference temperature, corresponding to the density
 PSURF  14.696 ** pressure at surface, for reporting well rates, etc.
 TSURF  60.000 ** temperature at surface, for reporting well rates

**  ==============  ROCK-FLUID PROPERTIES  ======================
 rockfluid
 rpt 1 **STONE2 default**
 swt   **  Water-oil relative permeabilities
**   Sw          Krw         Krow
```

```
**  ----      --------      --------
 0.2          0             0.7
 0.25         0.0006        0.525
 0.3          0.0013        0.3955
 0.35         0.0024        0.2905
 0.4          0.0035        0.2135
 0.45         0.006         0.1575
 0.5          0.009         0.1155
 0.55         0.014         0.0784
 0.6          0.02          0.0476
 0.65         0.03          0.0231
 0.7          0.05          0.0001
 1            1             0
slt **NOSWC  **  Liquid-gas relative permeabilities
**   Sl           Krg           Krog
**  ----      --------      -------
 0.20         0.85          0
 0.25         0.731         0
 0.30         0.6205        0.0105
 0.35         0.527         0.0238
 0.40         0.4446        0.0392
 0.45         0.3723        0.0616
 0.50         0.3128        0.0882
 0.55         0.2618        0.119
 0.60         0.2168        0.154
 0.65         0.1675        0.1925
 0.70         0.1301        0.238
 0.75         0.0961        0.2926
 0.80         0.0663        0.3514
```

```
 0.85        0.0383      0.4172
 0.90        0.0085      0.4984
 0.95        0           0.5894
 1.00        0           0.7
*SWR   0.20
*SORW  0.10
*KRTYPE *CON 1  ** Entire grid

**  ==============  INITIAL CONDITIONS  ======================
*INITIAL
*VERTICAL *ON
*REFPRES 420
*REFDEPTH 1031.824
*SW *CON 0.20
*SO *CON 0.80
*TEMP *CON 50  **Initial reservoir temperature 50 degree F
** Compositions of the initial oil phase
*mfrac_oil 'C1'       *con 0.001
*mfrac_oil 'C2 toC14' *con 0.4
*mfrac_oil 'C20_35'   *con 0.3
*mfrac_oil 'C36+'     *con 0.3

**  ==============  NUMERICAL CONTROL  ======================
*NUMERICAL
*DTMAX 5
*NEWTONCYC 8
*NORM     *PRESS 16  *SATUR 0.2   *TEMP 10  *Y 0.2   *X 0.2
*MINPRES 1.0
*CONVERGE *PRESS 1
```

```
*MATBALTOL  0.00001
*PIVOT *ON
*RANGECHECK OFF
*RUN

**  =============  RECURRENT DATA  ========================
*DATE 2004 01 01
*DTWELL 1e-5
   *WELL 'Injector'
   *WELL 'Producer'
   *INJECTOR 'Injector'
**--------------'WATER'  'C1'  'C2 toC14'  'C20_35'  'C36+'  'C3'
   *INCOMP WATER  1.0     0.0      0.0        0.0     0.0   0.0
   *TINJW 435  ** degree F
   *QUAL .95
   *OPERATE  *STW 7000
   *OPERATE  *MAX  *BHP 435
**----------    rad   geofac wfrac  skin
   *GEOMETRY *J  0.35 0.249   1.0   0.0
   *PERF GEO 'Injector' ** i    j  k    wi.
                  34 1:1 15   3252.5
   *PRODUCER 'Producer'
   *OPERATE *MIN *BHP 416
   *OPERATE *MAX *STL 7000
   *OPERATE *MIN STEAMTRAP 18.0
   ** These values are calculated from Appendix A
   **---------- rad    geofac wfrac  skin
   GEOMETRY *J  0.35   0.249   1.0   0.0
   *PERF GEO 'Producer' ** i   j   k  wi. Attach horizontal well to s/s
```

```
                 34 1:1 19  3252.5        ** wellbore
*SHUTIN 'Injector'
*UHTR *IJK 34 1:1 15 347320
*TMPSET *IJK 34 1:1 15 456
*UHTR *IJK 34 1:1 19 347320
*TMPSET *IJK 34 1:1 19 456
*TIME 1.
*TIME 5.
*TIME 10.
*TIME 15
*TIME 30
*TIME 100
*UHTR *IJK 34 1:1 15 0  ** SHUTOFF Heating in injector
*UHTR *IJK 34 1:1 19 0  ** SHUTOFF Heating in producer
*OPEN 'Injector'
*TIME 105
*TIME 110
*TIME 120
*TIME 150
*TIME 200
*TIME 400
*TIME 500
*TIME 1000
*TIME 2000
*TIME 3000
*TIME 4000
*STOP
```

A.2 Grid-Size Sensitivity Analysis

A sensitivity study on grid size is conducted to assess its effect on the simulation results and to determine the appropriate grid size that balances accuracy and computation time. It is believed that in the SAGD process the displacement and thermal fronts in the vertical cross section are much sharper than those in the direction along the well direction. Hence, grid dimensions in the x-z plane more significantly affect numerical results and our sensitivity analysis is mainly based on a two-dimensional, homogeneous model (100 m wide, 20 m thick). A series of numerical simulations are performed with four grid systems that are composed of grid blocks of 39×20, 101×20, 201×41, and 299×60, respectively. Table A.1 lists the block size of the above four grids. Note that the coarsest grid (39×20) is non-uniform in the x-direction, with the block width varying gradually from 1 m in the center to 5 m at the outer boundaries.

Table A.1: Grid dimensions of the four grid systems for the grid-size sensitivity analysis.

	Number of grid blocks	Grid size (m)	
		dx	dz
Nonuniform	39×20	$1 \sim 5$	1
Uniform	101×20	1	1
Uniform	201×41	1/2	1/2
Uniform	299×60	1/3	1/3

Figure A.1 illustrates the comparison of the simulation results obtained with the four grids in the form of the oil production rate and cumulative oil recovery versus time. The four grids yield almost identical results for the first 800 days of injection and a similar trend for the rest of the production life. As seen in Figure A.1(a), the coarsest grid (39×20) predicts the lowest oil rate for the main production plateau,

and reducing the grid size results in higher oil rates. The increase of the oil rate with a finer grid is likely attributed to the sharper thermal and displacement fronts resolved by the finer grid that result in faster heat conduction across the chamber boundary and consequently a larger oil drainage rate. It is also observed that the discrepancy in the oil rate due to the grid size becomes smaller as the grid size decreases, indicating convergence of the numerical solution.

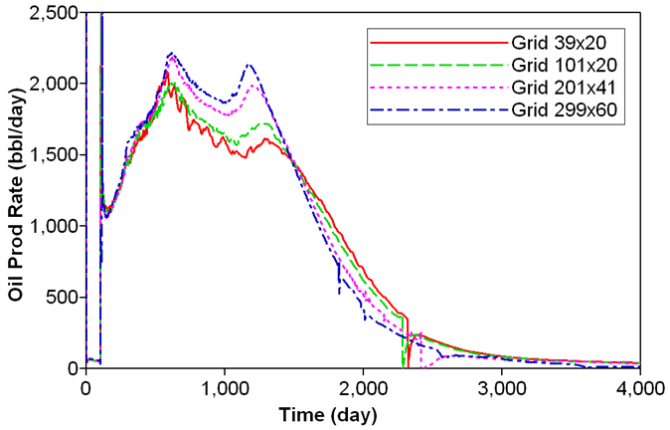

(a)

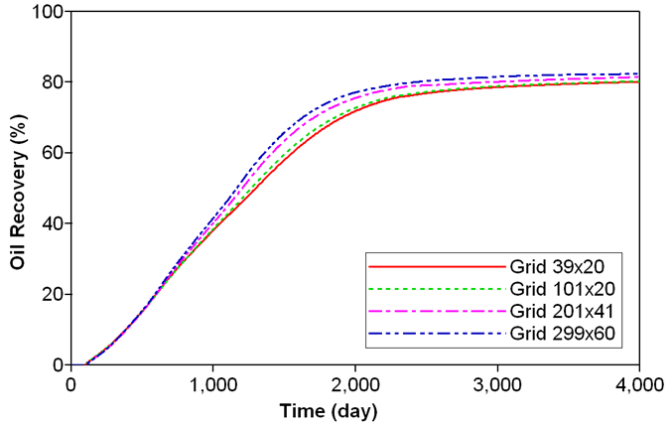

(b)

Figure A.1: Results of grid-size sensitivity analysis: (a) oil production rates and (b) cumulative oil recovery.

The cumulative oil production shown in Figure A.1(b) exhibits a similar trend with

respect to the grid size. The difference between the grids is much less pronounced. The relative difference in the cumulative oil production between the nonuniform grid and the finest grid (grid size of 1/3 m $\times$ 1/3 m) is less than 10%. In typical reservoir characterization, a reservoir model constructed from seismic and log data is normally subject to large uncertainties, for example, $\pm$30% in permeability. Such uncertainties can easily cause up to 50% error in the prediction of oil production. Compared with the former error, the uncertainty caused by the usage of nonuniform grid is acceptable; therefore, the nonuniform grid 37×20 or finer grid is appropriate for the simulation of the reservoir model in this study.

Appendix B

Implementation of LEM and Sensitivity Study

B.1 Improved LEM: Local Equilibrium Approximation

The formulation derived for the local equilibrium model in Chapter 5 eliminates one additional equation that is normally required in population balance approaches to track foam texture evolution during foam flow. The simulation runs with the foam simulator implemented with the LEM equation, Eq. (5.17), however, is found to be slow because of small time steps and frequent time step cuts. This unexpected low computation speed is likely attributed to the increase in the stiffness of the equation system introduced by the assumption of local equilibrium. Appropriate improvement is needed to reduce such stiffness and speed up simulation runs, thus improving the computational efficiency. To that end, we modified the original formulation of LEM and derived a so-called local equilibrium approximation (LEA) formulation as described below.

As described in Chapter 5, the assumption of local equilibrium sets the convection and accumulation terms in the original full physics equation to zero and yields Eq. (5.15). Here, we add a small fraction of the accumulation term back to the simplified equation to introduce a damping effect that reduces the stiffness of the equation system. The resultant equation is given by

$$\beta \frac{\partial}{\partial t}(S_g n_f) = S_g(k_1|v_w||v_f|^{\frac{1}{3}} - k_{-1}|v_f|n_f) \quad , \tag{B.1}$$

where β is a fraction constant that determines the magnitude of the damping effect introduced by the accumulation term. As shown later in the sensitivity study, a value of β between 0.05 – 0.15 gives excellent results in terms of both accuracy and computational performance. Note that it is assumed that the porous medium has a homogeneous porosity and therefore the porosity, ϕ is eliminated from the equation.

Applying backward discretization in time and implicit treatment of the foam texture, n_f, to Eq. (B.1) yields the discretized form of local equilibrium approximation,

$$\left({n_f}^{\nu+1}\right)^{\omega} + \frac{\left(\frac{\beta}{\Delta t} + k_{-1}^0|{v_f}^{\nu+1}|\right) n^{*\omega}}{k_1^0|{v_w}^{\nu+1}||{v_f}^{\nu+1}|^{1/3}} {n_f}^{\nu+1} - \left(\frac{\beta}{\Delta t}\frac{{S_g}^{\nu}{n_f}^{\nu}}{{S_g}^{\nu+1}k_1^0|{v_w}^{\nu+1}||{v_f}^{\nu+1}|^{1/3}} + 1\right) n^{*\omega} = 0 \quad , \tag{B.2}$$

where the superscripts ν and $\nu+1$ designate values at the time levels of t^{ν} and $t^{\nu+1}$, respectively, and $\Delta t = t^{\nu+1} - t^{\nu}$ is the current time step size. Because there is no convection term and thus no spacial dependency involved in Eq. (B.2), we obtain an explicit equation for the foam texture in each individual grid block that can be easily solved. For instance, with $\omega = 3$, we have a cubic form of the equation,

$$\left({n_f}^{\nu+1}\right)^3 + A{n_f}^{\nu+1} + B = 0 \quad , \tag{B.3}$$

where

$$A = \frac{\left(\frac{\beta}{\Delta t} + k_{-1}^{0}|{v_f}^{\nu+1}|\right)(n^*)^3}{k_1^0|{v_w}^{\nu+1}||{v_f}^{\nu+1}|^{1/3}} \quad , \tag{B.4}$$

and

$$B = \left(\frac{\beta}{\Delta t}\frac{{S_g}^{\nu}{n_f}^{\nu}}{{S_g}^{\nu+1}k_1^0|{v_w}^{\nu+1}||{v_f}^{\nu+1}|^{1/3}} + 1\right) n^{*3} \quad . \tag{B.5}$$

This cubic equation is solved using standard analytical formulae (Hodgman, 1959). Compared to Eq. (5.17) for the local equilibrium model, the additional terms with a multiplier, $\frac{\beta}{\Delta t}$ in Eq. (B.2) for the local equilibrium approximation model improves the numerical performance significantly. The multiplier, $\frac{\beta}{\Delta t}$ controls the numerical solution effectively according to the time step size. For example, at very small time steps, $\frac{\beta}{\Delta t}$ becomes $\gg 1$ that overweighs all the other terms in Eq. (B.2) and sets the solution of n_f at the new time equal to its value at the previous time step. On the other hand, at very large time steps, $\frac{\beta}{\Delta t}$ becomes $\ll 1$ and Eq. (B.2) reduces to Eq. (5.17). As shown later in this appendix, significant improvement to the computation speed while maintaining accuracy of the numerical solution of foam flow are observed with this new local equilibrium approximation approach.

B.2 Algorithm for Foam Texture Calculation in LEM/LEA

The foam models presented in this work are implemented as an option to M^{2}NOTS that is a compositional extension of TOUGH2. M^{2}NOTS is a classic, nonisothermal, compositional simulator based on the integral finite difference method (IFDM) (Narasimhan and Witherspoon, 1976). In this framework, the average foam bubble density is treated as a nonchemical component of the gas phase, and solved fully implicitly with the full physics model or explicitly with the local equilibrium model.

The pseudocodes for the full physics model was provided in detail by Kovscek (1994), and, for illustration, the algorithm for the LEM/LEA calculations is given below,

0. Given the solution of the standard flow equation system at the kth iteration and the time level, $t^{\nu+1}$,

1. Obtain phase velocities at each grid block at the baseline values of the primary variables and their incrementals (numerical Jacobean calculation used here)

   (a) Loop through all the connections between grid blocks and sum flow of each phase into and out of a grid block in the three orthogonal directions.

   (b) Loop through all the grid blocks that contain any sink/source and account for the contribution to phase velocities due to sink/source flows.

   (c) Loop through all the grid blocks, calculate the arithmetic average of phase velocities for each direction for each grid block, and take the magnitude of the resultant vector for foam texture calculation

2. Retrieve updated values of other variables required for foam texture calculation, that include ${S_g}^{\nu+1,k}$, ${P_c}^{\nu+1,k}$, ${C_s}^{\nu+1,k}$, etc.

3. Compute the foam texture, ${n_f}^{\nu+1,k+1}$ at the given local conditions from Eq. (5.17) or Eq. (B.2) for each grid block.

4. According to the presence of foam, update the gas mobility within each grid block by the ratio of relative permeability to foamed gas up on the gas effective viscosity. The foamed gas relative permeability is evaluated at the flowing gas saturation using the gas relative permeability relation (*e.g.*, Kovscek and Radke (1994)). The effective viscosity is computed using Eq. (5.6).

5. Process to the next iteration, k+1 and iterate through steps 1–4 until converged.

B.3 Parameters in LEA

B.3.1 Effect of Parameter β

The parameter β in the LEA model controls the damping effect and is critical for accurately and effectively solving the foam texture based on the local equilibrium approximation. The effect of the parameter β is examined by conducting a series of simulation runs for the transient foam flow described in Section 5.3.3 with β varying from 0 to 1. Note that $\beta = 0$ corresponds to the LEM (Eq. (5.17)). The foam model parameters listed in Table 5.1 are used. The numerical results of those runs are compared in Figures B.1–B.3 that give the predicted profiles of foam texture, aqueous phase saturation, and pressure, respectively, at three different dimensionless times.

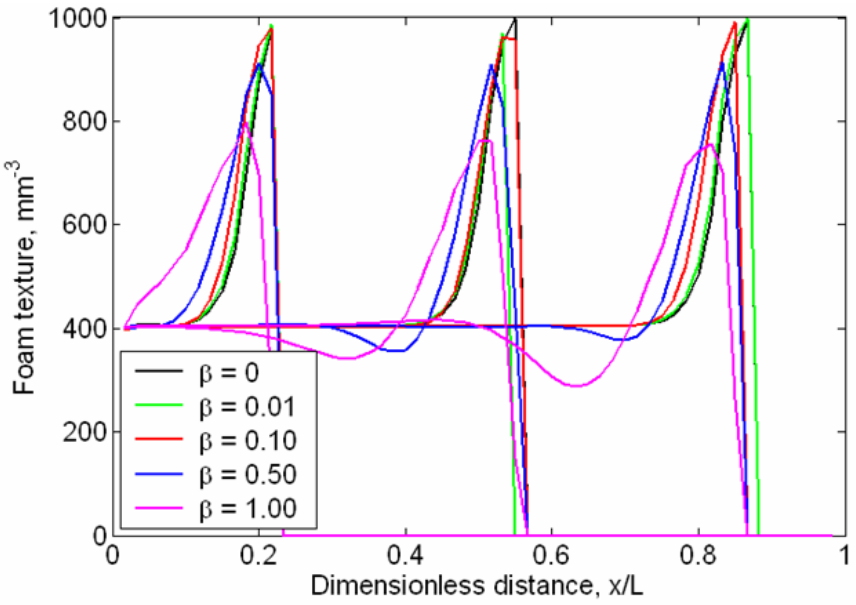

Figure B.1: Profiles of foam texture predicted by the LEA with β varied from 0 to 1.0 at dimensionless times of 0.1, 0.3, and 0.48 PVI.

All the cases give converged solutions that predict approximately the evolution

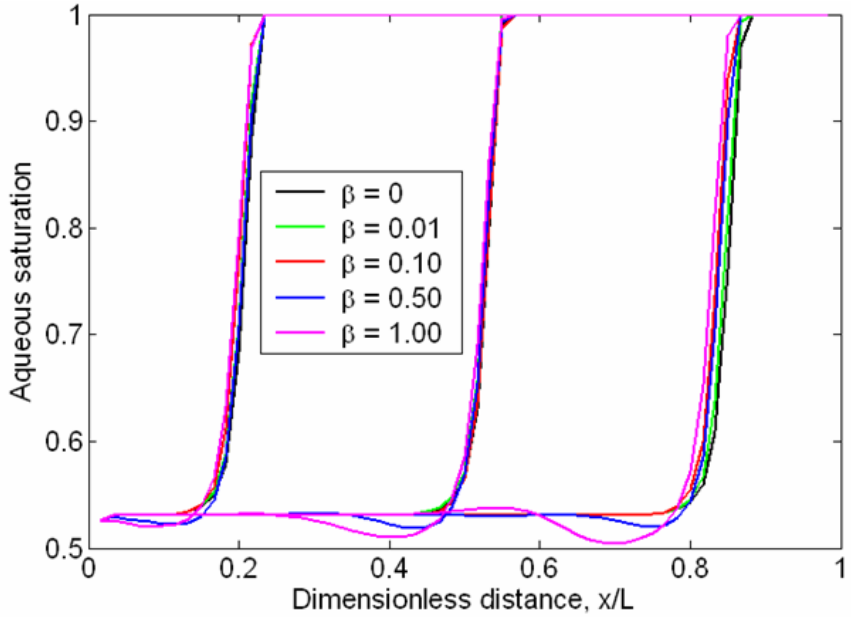

Figure B.2: Profiles of aqueous phase saturation predicted by the LEA with β varied from 0 to 1.0 at dimensionless times of 0.1, 0.3, and 0.48 PVI.

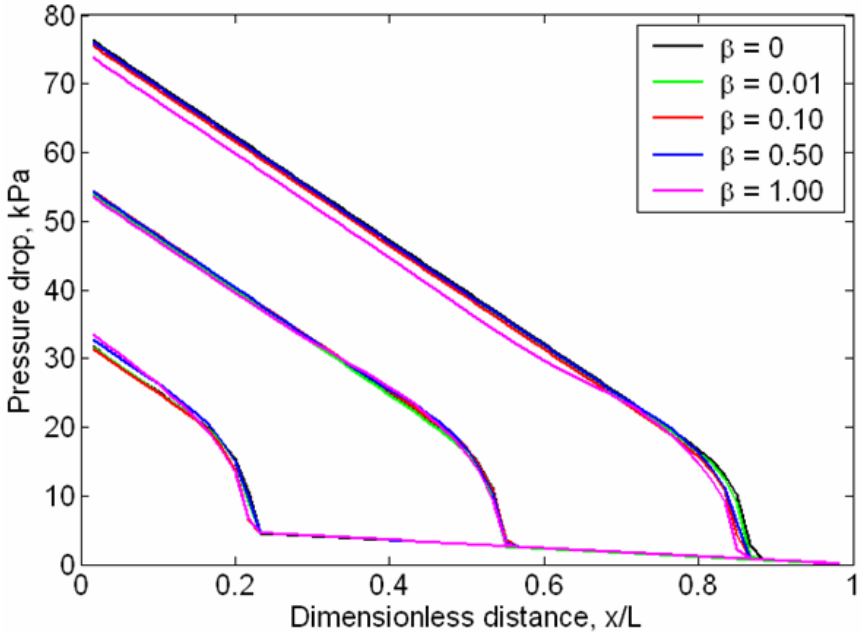

Figure B.3: Profiles of pressure predicted by the LEA with β varied from 0 to 1.0 at dimensionless times of 0.1, 0.3, and 0.48 PVI.

of the foam front through the porous medium. The value of β equal to or greater than 0.5, however, results in unphysical profiles of foam texture and aqueous phase saturation. For instance, the foam texture predicted by the cases of $\beta = 0.5$ and 1, as shown in Figure B.1, exhibits at the region upstream of the foam front a dip that is not observed in the results of the full physics model. Similarly, Figure B.2 also shows an expected decrease in aqueous phase saturation in the region upstream of the displacement front. The pressure profiles shown in Figure B.3 appear to be insensitive to the value of β. The abnormal reductions in the foam texture and aqueous phase saturation close to the displacement front are somewhat proportional to the value of β. These unrealistic fluctuations are mainly due to the smoothing effect introduced by the fractional accumulation term. With the value of β equal to or smaller than 0.1, as seen in Figure B.1 and Figure B.2, such unphysical fluctuations disappear and the corresponding solutions are almost identical to that of the LEM ($\beta = 0$). Further testing with different values of β indicates that the upper limit of the parameter β ensuring reliable solutions is 0.15.

The computation speed is affected significantly by the value of β in the LEA. Figure B.4 gives the CPU times required for a single simulation run of the transient foam flow with constant surfactant (see Chapter 5) using 59 gridblocks. A Dell server with dual 2.8 GHz processors and 3.75 GB RAM is used. The parameter ω, that is discussed in the next subsection, varies from 0.5 to 1, 2, and 3 for the CPU time comparison in Figure B.4. Despite the wide variation in the CPU time with different values of ω, the computational time is dramatically shortened by the LEA ($\beta > 0$) compared to the LEM ($\beta = 0$). For example, for $\omega = 3$, the CPU time required by the LEM is 52 seconds, while with $\beta = 0.1$ the CPU time is cut down to only 18 seconds, yielding a speed-up factor of nearly three. It is also observed in Figure B.4 that further increasing β does not impact the CPU time of the simulation run. Combining the observation of the accuracy of predicted profiles and the CPU time trend, we

recommend the optimum value range of β be 0.05–0.15.

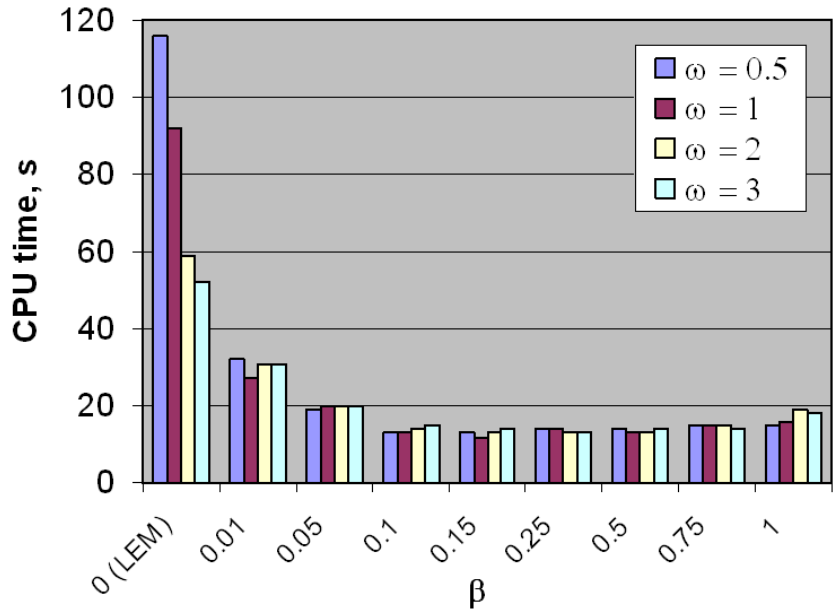

Figure B.4: Comparison of CPU time for a single simulation run.

B.3.2 Effect of Parameter ω

The parameter ω determines the function type of k_1 that describes the dependency of foam generation sites upon the density of the existing foam bubbles in pore spaces. It is believed that the k_1 function depends on the pore structure and pore size distribution. Here, we examine four types of k_1 functions, namely, square root, linear, quadratic, and cubic, that correspond to ω of 1/2, 1, 2, and 3, respectively, and are depicted in Figure B.5 as functions of n_f/n^*.

The simulation runs with the four values of ω give similar foam texture profiles, as seen in Figure B.6, with the main difference in the plateau level of foam texture in the zone upstream of the displacement front. The plateau level of foam texture in the displaced zone reflects the equilibrium between the foam generation and coalescence. With various dependencies of foam generation sites upon the density of the

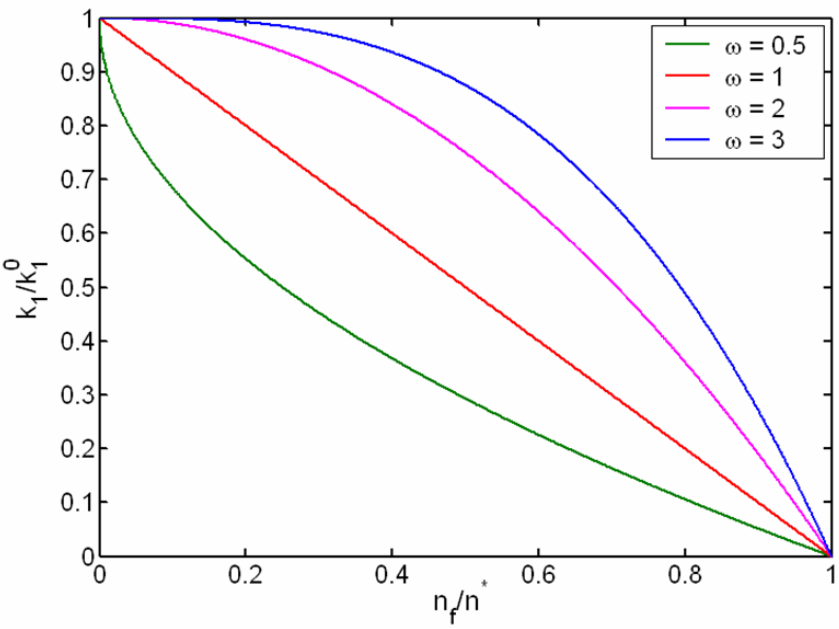

Figure B.5: Functions for calculating k_1 in the snap-off generation model.

existing foam bubbles specified by the value of ω, the difference in the foam texture in the equilibrium zone is expected. Figure B.7 and Figure B.8 provide the simulated aqueous phase saturation and pressure profiles at three different dimensionless times. Slight difference is observed in the saturation profiles between cases with different values of ω, while the pressure gradients in the zone with the presence of foam vary significantly between cases. According to Eq. (5.6), the effective viscosity of foam is inversely proportional to the foam texture. Foams with finer texture or smaller foam bubbles experience greater flow resistance. Therefore, the variation in the plateau level of foam texture in the equilibrium region results in the difference in pressure gradients shown in Figure B.8. As described later in Chapter 7, the more appropriate function of $k_1(n_f)$ may be determined experimentally by conducting foam flow experiments with various injection conditions and consequently make the prediction of foam flow by the foam models presented in this work more accurate.

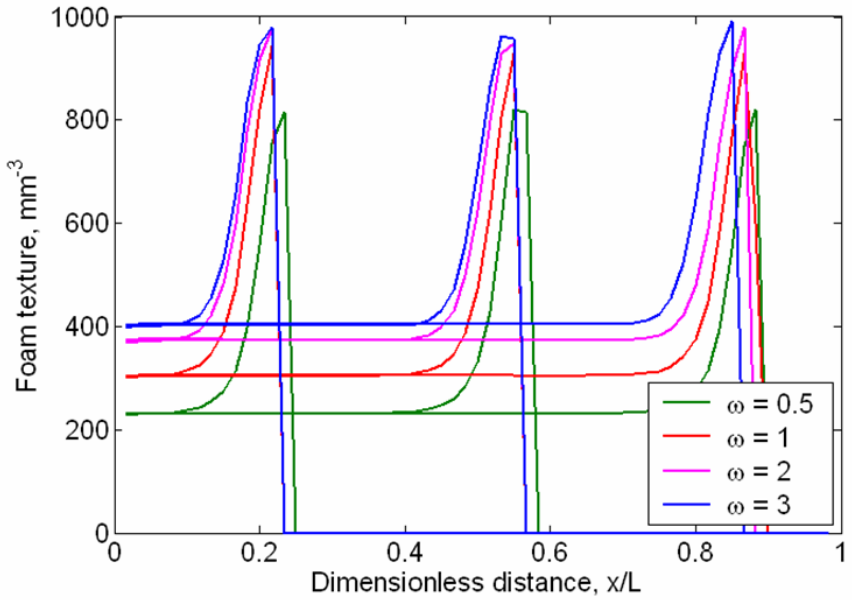

Figure B.6: Foam texture profiles predicted by the LEA with different values of ω at dimensionless times of 0.1, 0.3, and 0.48 PVI.

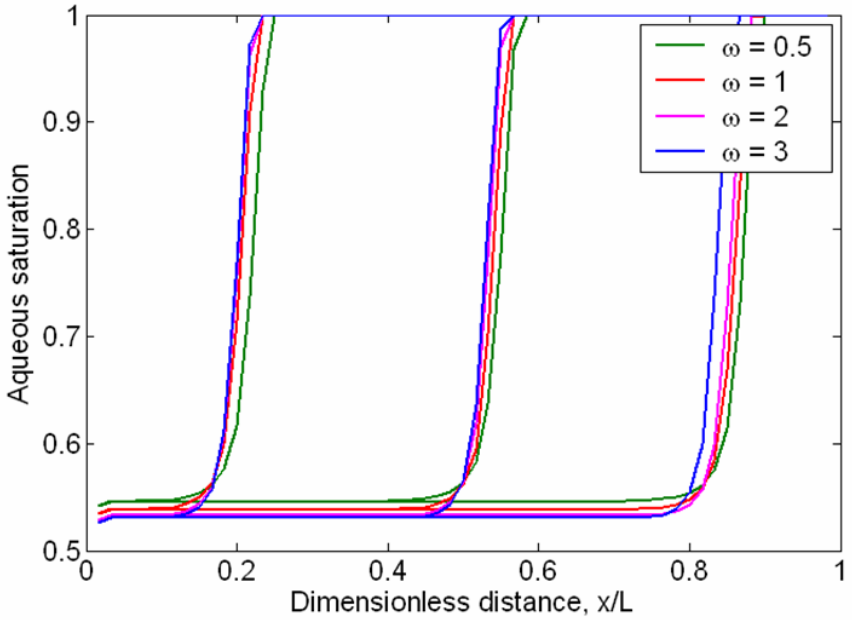

Figure B.7: Aqueous phase saturation profiles predicted by the LEA with different values of ω at dimensionless times of 0.1, 0.3, and 0.48 PVI.

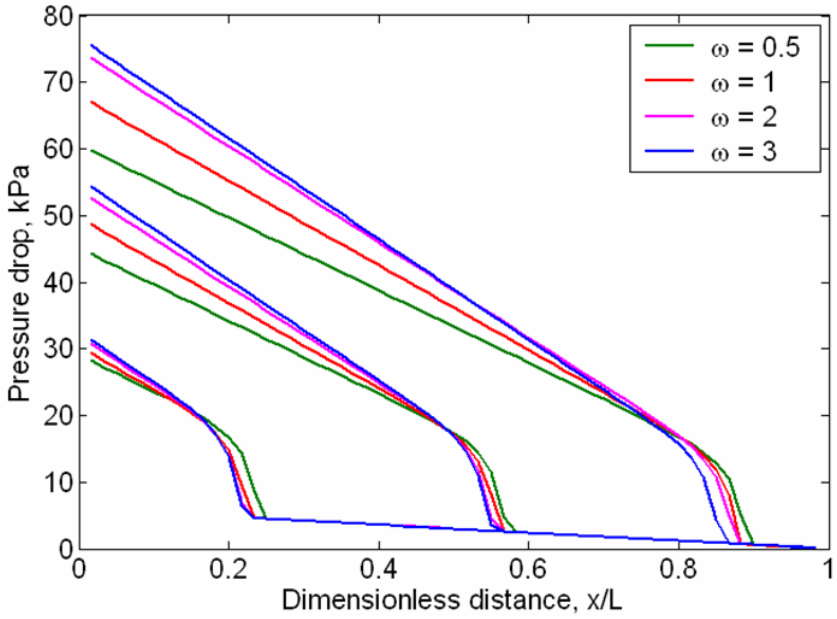

Figure B.8: Pressure profiles predicted by the LEA with different values of ω at dimensionless times of 0.1, 0.3, and 0.48 PVI.

B.4 Sensitivity of Gridblock Size

A grid refinement sensitivity analysis is conducted for the local equilibrium model to assess the effect of gridblock size on the numerical prediction of one-dimensional foam flow. In this analysis, five gridblock sizes are used to perform numerical simulation with the LEM-based foam simulator. The base case mimics foam flow in the 0.60 m long cylindrical core with a one-dimensional, uniform grid system containing 60 gridblocks that are each 0.01 m. For the refined cases, the number of grid blocks is multiplied by 2, 4, 8, and 16 while holding the system length constant thereby giving gridblock sizes of 5×10^{-3}, 2.5×10^{-3}, 1.25×10^{-3}, and 6.25×10^{-4} m, respectively.

Figure B.9 compares the predicted profiles of foam texture at dimensionless times of 0.1, 0.3, and 0.5 PVI between the base and refined cases. All of the cases show similar features of a foam texture peak at the displacement front as a result of net foam generation (as described above). The simulated texture front becomes somewhat

sharper as the gridblock size decreases. The maximum in foam texture, however, does not increase. Comparison of the profiles shows no visual change in the profiles when the gridblock size is equal to or smaller than 1.25×10^{-3} m. The L2 error norm (normalized by the finest grid solution) for the profile at 0.3 PVI decreases linearly as the number of grid blocks increases. The L2 norm for n_f is 0.4, 0.3, 0.1 and 0 for each of the grids respectively. Figure B.10 and Figure B.11 give the comparisons of aqueous saturation and pressure profiles, respectively, for the base and refined cases. As expected, a similar sharpening effect is also observed here. The aqueous-phase saturation front is less sensitive to grid size in comparison to foam texture. In turn, the predicted pressure profile are even less sensitive to the gridblock size. The L2 error norms for Sw and p also decrease linearly as the number of grid blocks increases and the maximum errors are less than 0.05.

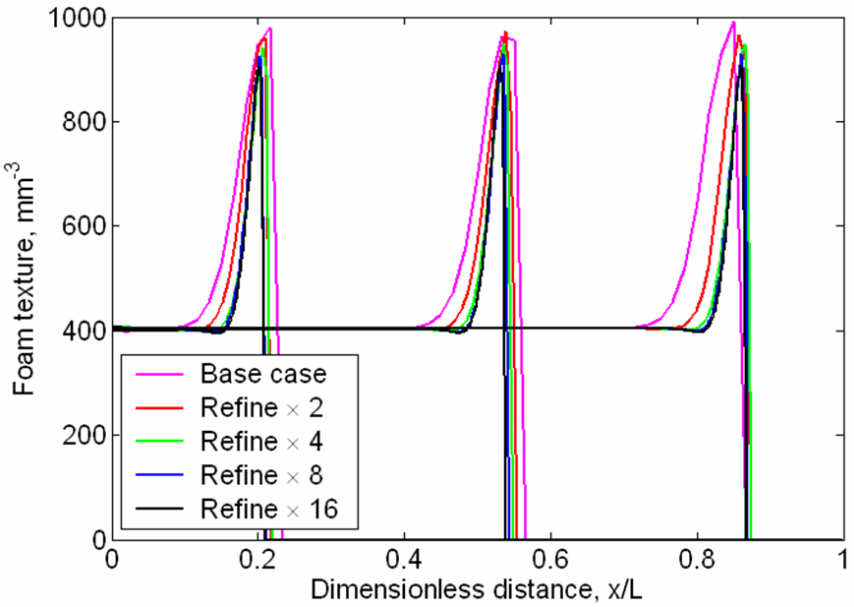

Figure B.9: Sensitivity of gridblock size: computed foam texture.

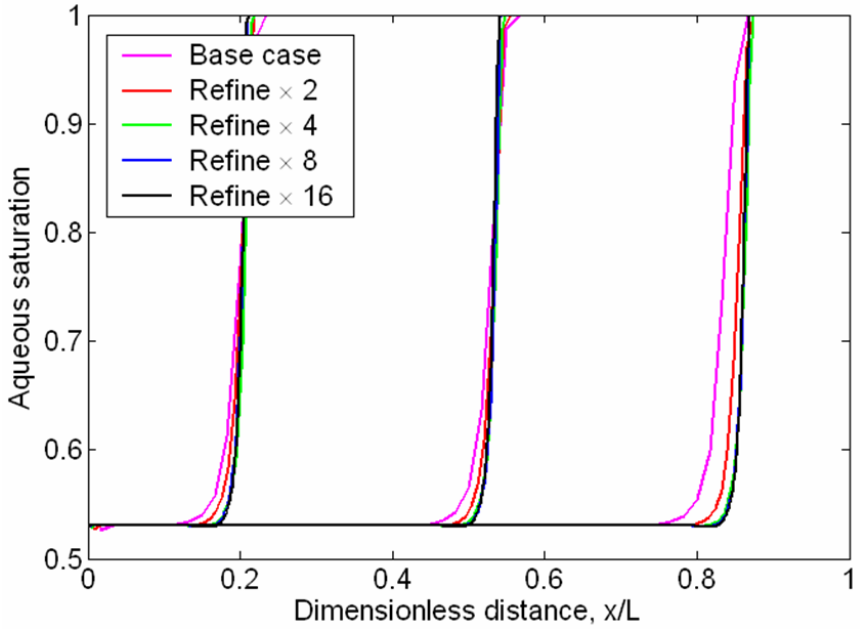

Figure B.10: Sensitivity of gridblock size: computed aqueous saturation.

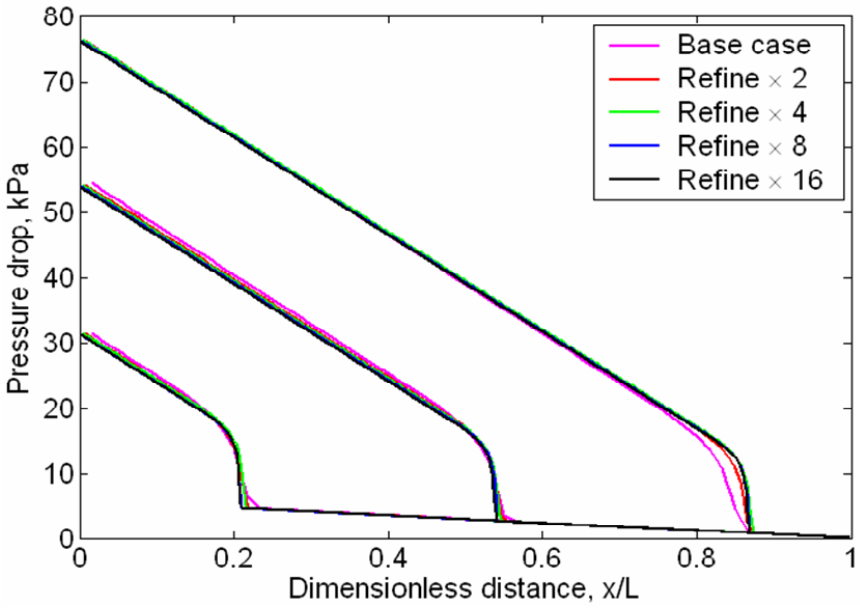

Figure B.11: Sensitivity of gridblock size: computed pressure.

Nomenclature

$\tilde{n}$	dimensionless number density of foam defined as $\frac{n}{n_c}$
$\tilde{t}$	dimensionless time defined as $\frac{t}{t_c}$
$\tilde{u}$	dimensionless Darcy phase velocity defined as $\frac{u}{U_c}$
$\tilde{v}$	dimensionless interstitial phase velocity defined as $\frac{v}{U_c}$
$\tilde{x}$	dimensionless length variable defined as $\frac{x}{L}$
d	diameter, m
es, eo, ev	exponent constants for estimating FM in STARS' foam model
f	exponent constant for water relative permeability
f_c	percolation fraction
f_g	fraction flow of gas
g	acceleration due to gravity, m^2/s; exponent constant for gas relative permeability
h	steam chamber height, m; depth of flow channel, m
k	effective permeability, m^2; foam generation or coalescence rate constant

k_r	relative permeability
m	constant between 3 and 4 from the temperature dependency of oil viscosity
n	number density of foam, m^{-3}
q_o	oil drainage rate, m^3/s
r	radial direction, m
t	time, s
u	Darcy phase velocity, m/s
v	interstitial phase velocity, m/s
x, y, z	three principle directions in a Cartesian system, m
A	area, m^2; a constant in the LEA equation
A_s	constant in the Langmuir model for surfactant adsorption
B	constant in the LEA equation
C	concentration, wt%
CT	CT number, H
D_v	vertical well spacing, m
Da	Damkohler number
FM	dimensionless factor of mobility reduction due to foam
J	Leverett J-function for capillary pressure

K	permeability, m^2
K_s	constant in the Langmuir model for surfactant adsorption
L	horizontal well length, m; core length, m
L_s	shale correlation length, m
MRF	maximum mobility reduction factor due to foam
N_c	capillary number
P	pressure, Pa
P_c	capillary pressure, Pa
P_s	probability of occurrence of shale; shale percentage
PV	pore volume injected
Q	heat of adsorption
Q_b	source/sink term for foam bubbles
Q_w	source/sink term for aqueous phase
R	gas constant, J/kg·K; reservoir radius, m
S	phase saturation
S_3	least principle stress, Pa
S_v	overburden stress, Pa
S_{Hmax}	maximum horizontal stress, Pa
S_{hmin}	minimum horizontal stress, Pa

T	temperature, °C
U_c	characteristic velocity, m/s
X	fraction of foam
X_D	dimensionless length

Greek

α	thermal diffusivity, m^2/s; proportionality constant in effective viscosity; constant in the equation of foam coalescence rate
β	constant in the local equilibrium approximation
Δ	difference or step size in time
δ	ratio of surface area to mass, m^2/kg
η	percolation exponent constant
Γ	surfactant adsorption on the rock
μ	dynamic viscosity, Pa·s
ν	kinematic viscosity, St
ω	exponent constant in foam generation coefficient
ϕ	porosity
ψ	constant of proportionality in foam trapping equation
ρ	density, kg/m^3
σ	surface tension, N/m

Superscripts

$*$	limiting foam texture or limiting capillary pressure
0	reference value
$\nu, \nu+1$	level of time in the numerical simulation
k	number of Newton-Raphson iterations in the numerical simulation
ref	at reference conditions

Subscripts

-2	foam coalescence due to oil
0	reference value
$1, -1$	generation, coalescence rate constant
a	air
b	foam bubble
c	connate water, coalescence, or characteristic value
d	reduced saturation
dry	air saturated
f	flowing foam
g	gaseous phase
le	local equilibrium
max	maximum value

o	oil phase
r	rock
s	surfactant or steam
t	trapped or stationary foam
w	aqueous phase or water
wc	connate water
wet	water saturated

Acronyms

AWR	above well region
BHP	bottom hole pressure
COSR	cumulative oil-steam ratio, bbl oil/bbl CWE steam
CSOR	cumulative steam-oil ratio, bbl CWE steam/bbl oil
CSS	cyclic steam stimulation
CWE	cold water equivalent of steam
ES-SAGD	expanding solvent steam-assisted gravity drainage
FA-SAGD	foam-assisted steam-assisted gravity drainage
FPM	full physics model
LEA	local equilibrium approximation
LEM	local equilibrium model

M^2NOTS	a compositional, nonisothermal reservoir simulator
NCG	noncondensable gas
NWR	near well region
OBIP	original bitumen in place
OOIP	original oil in place
OSR	oil-steam ratio, bbl oil/bbl CWE steam
RC	reservoir condition
SAGD	steam-assisted gravity drainage
SISIM	sequential indicator simulation
SOR	steam-oil ratio, bbl CWE steam/bbl oil
XSAGD	cross steam-assisted gravity drainage

Bibliography

Adenekan, A. E., Patzek, T. W. and Pruess, K.: 1993, Modeling of multiphase transport of multicomponent organic contaminants and heat in the subsurface: Numerical model formulation, *Water Resour. Res.* **29**(11), 3727–3740.

Akin, S.: 2004, Mathematical modeling of steam assisted gravity drainage, *paper SPE 86963 presented at the SPE International Thermal Operations and Heavy Oil Symposium*, Bakersfield, CA. 16–18 March.

Akin, S. and Kovscek, A. R.: 2003, Computed tomography in petroleum engineering research, *in* F. Mees, R. Swennen, M. V. Geet and P. Jacobs (eds), *Applications of X-ray Computed Tomography in the Geosciences*, Vol. 215, Geological Society, London, pp. 23–38. Special Publications.

Albahlani, A. M. and Babadagli, T.: 2008, A critical review of the status of SAGD: Where are we and what is next?, *paper SPE 113283 presented at the SPE Western Regional and Pacific Section AAPG Joint Meeting*, Bakersfield, CA. 31 March–2 April.

Alvarez, J. M., Sawatzky, R. P., Forster, L. M. and Coates, R. M.: 2008, Alberta's bitumen carbonate reservoirs — moving forward with advanced R&D, *paper 2008-467 presented at the World Heavy Oil Congress*, Edmonton, Canada. 10–12 March.

Alvarez, J., Rivas, H. and Rossen, W. R.: 2001, Unified model for steady-state foam behavior at high and low foam qualities, *SPE Journal* **6**(3), 325–333.

Aronson, A. S., Bergeron, V., Fagan, M. E. and Radke, C. J.: 1994, The influence of disjoining pressure on foam stability and flow in porous media, *Colloids Surfaces A: Physicochemical Engineering Aspects* **83**(2), 109–120.

Bagci, A. S.: 2006, Experimental and simulation studies of SAGD process in fractured reservoirs, *paper SPE 99920 presented at the SPE/DOE Symposium on Improved Oil Recovery*, Tulsa, OK. 22–26 April.

Bagci, S.: 2004, The effect of fractures on the steam-assisted gravity drainage process, *Energy & Fuels* **18**(6), 1656–1664.

Bertin, H. J., Quintard, M. Y. and Castanier, L. M.: 1998, Modeling transient foam flow in porous media using a bubble population correlation, *SPE Journal* **3**(4), 356–362. SPE-49020-PA.

Blaker, T., Aarra, M. G., Skauge, A., Rasmussen, L., Celius, H., Martinsen, H. A. and Vassenden, F.: 2002, Foam for gas mobility control in the Snorre field: The FAWAG project, *SPE Reservoir Evaluation Engineering* **5**(4), 317–323. SPE-78824-PA.

Burton, R. C., Chin, L. Y., Davis, E. R., Enderlin, M., Fuh, G., Hodge, R., Ramos, G. G., VanDeVerg, P., Werner, M., Mathews, W. L. and Petersen, S.: 2005, North slope heavy-oil sand-control strategy: Detailed case study of sand production predictions and field measurements for Alaskan heavy-oil multilateral field, *paper SPE 97279 presented at the SPE Annual Technical Conference and Exhibition*, Dallas, TX. 9–12 October.

Buschkuehle, B. E., Hein, F. J. and Grobe, M.: 2007, An overview of the geology

of the upper devonian Grosmont carbonate bitumen deposit, Northern Alberta, Canada, *Natural Resources Research* **16**(1), 3–15.

Butler, R. M.: 1994, Steam-assisted gravity drainage: Concept, development, performance and future, *Journal of Canadian Petroleum Technology* **32**(2), 44–50.

Butler, R. M.: 1998a, SAGD comes of AGE, *Journal of Canadian Petroleum Technology* **37**(7), 9–12.

Butler, R. M.: 1998b, *Thermal Recovery of Oil and Bitumen*, Prentice-Hall, Inc., Calgary, Alberta.

Butler, R. M.: 2001, Application of SAGD, related processes growing in Canada, *Oil & Gas Journal* **99**(20), 74–78.

Butler, R. M., Mcnab, G. S. and Lo, H. Y.: 1981, Theoretical studies on the gravity drainage of heavy oil during in-situ steam heating, *Canadian Journal Chemical Engineering* **59**(4), 455–460.

Butler, R. M. and Stephens, D. J.: 1981, The gravity drainage of steam heated heavy oil to parallel horizontal wells, *Journal of Canadian Petroleum Technology* **20**(2), 90–96.

Castanier, L. M. and Brigham, W. E.: 1991, An evaluation of field projects of steam with additives, *SPE Reservoir Engineering* **6**(1), 62–68.

Chambers, K. T. and Radke, C. J.: 1991, Capillary phenomena in foam flow through porous media, *in* N. Morrow (ed.), *Interfacial Phenomena in Petroleum Recovery*, Marcel Dekker, New York, pp. 191–255.

Chang, S. H., Owusu, L. A., French, S. B. and Kovarik, F. S.: 1990, The effect of microscopic heterogeneity on CO_2-foam mobility: Part 2 — mechanistic foam

simulation, *paper SPE 20191 presented at the SPE/DOE Enhanced Oil Recovery Symposium*, Tulsa, OK. 22–25 April.

Chou, S. I.: 1990, Percolation theory of foam in porous media, *paper SPE 20239 presented at the SPE/DOE Enhanced Oil Recovery Symposium*, Tulsa, OK. 22–25 April.

Chow, L. and Butler, R. M.: 1996, Numerical simulation of the steam-assisted gravity drainage process (SAGD), *Journal of Canadian Petroleum Technology* **35**(6), 55–62.

Cohen, D., Patzek, T. W. and Radke, C. J.: 1997, Onset of mobilization and the fraction of trapped foam in porous media, *Transport in Porous Media* **28**(3), 253–284.

Collins, P. M.: 2005, Geomechanical effects on the SAGD process, *paper SPE 97905 presented at the SPE/PS-CIM/CHOA International Thermal Operations and Heavy Oil Symposium*, Calgary, Alberta, Canada. 1–3 November.

Das, S.: 2005, Improving the performance of SAGD, *paper SPE 97921 presented at the SPE/PS-CIM/CHOA International Thermal Operations and Heavy Oil Symposium*, Calgary, Alberta, Canada. 1–3 November.

Das, S.: 2007, Application of thermal recovery processes in heavy oil carbonate reservoirs, *paper SPE 105392 presented at the SPE Middle East Oil & Gas Show and Conference*, Kingdom of Bahrain. 11–14 March.

de Vries, A. S. and Wit, K.: 1990, Rheology of gas/water foam in the quality range relevant to steam foam, *SPE Reservoir Engineering* **5**(2), 185–192. SPE-18075-PA.

Dilgren, R. E., Deemer, A. R. and Owens, K. B.: 1982, The laboratory development and field testing of steam/noncondensible gas foams in heavy oil recovery, *paper*

SPE 10774 presented at the SPE California Regional Meeting, San Francisco, CA. 24–26 March.

Djabbarah, N. F., Weber, S. L., Freeman, D. C., Muscatello, J. A., Ashbaugh, J. P. and Covington, T. E.: 1990, Laboratory design and field demonstration of steam diversion with foam, *paper SPE 20067 presented at the SPE California Regional Meeting*, Ventura, CA. 4–6 April.

Doan, L. T., Baird, H., Doan, Q. T. and Al, S. M. F.: 1999, An investigation of the steam-assisted gravity-drainage process in the presence of a water lag, *paper SPE 56545 presented at the SPE Annual Technical Conference and Exhibition*, Houston, TX. 3–6 October.

Edmunds, N. R.: 1998, Investigation of SAGD steam trap control in two and three dimensions, *paper SPE 50413 presented at the SPE International Conference on Horizontal Well Technology*, Calgary, Alberta, Canada. 1–4 November.

Edmunds, N. R.: 1999, On the difficult birth of SAGD, *Journal of Canadian Petroleum Technology* **38**(1), 14–17.

Edmunds, N. R., Kovalsky, J. A., Gittins, S. D. and Pennacchioli, E. D.: 1994, Review of Phase A steam-assisted gravity-drainage test, *SPE Reservoir Engineering* **9**(2), 119–124.

Egermann, P., Genard, G. and Delamaide, E.: 2001, SAGD performance optimization through numerical simulations: Methodology and field case example, *paper SPE 69690 presented at the SPE International Thermal Operations and Heavy Oil Symposium*, Porlamar, Margarita Island, Venezuela. 12–14 March.

Ettinger, R. E. and Radke, C. J.: 1992, Influence of foam texture on steady foam flow in Berea sandstone, *SPE Reservoir Engineering* **7**(1), 83–90. SPE-19688-PA.

Falls, A., Hirasaki, G. J., Patzek, T., Gauglitz, P., Miller, D. and Ratulowski, T.: 1988, Development of a mechanistic foam simulator: The population balance and generation by snap-off, *SPE Reservoir Engineering* **3**(3), 884–892.

Farouq-Ali, S. M.: 1997, Is there life after SAGD?, *Journal of Canadian Petroleum Technology* **36**(6), 20–23.

Fergui, A., Quintard, M., Bertin, H. and Defives, D.: 1995, Transient foam flow in porous media: Experiments and simulation, *paper presented at the 8th European IOR Symposium*, Vienna, Austria. 15 May.

Fisher, A. W., Foulser, R. W. and Goodyear, S. G.: 1990, Mathematical modeling of foam flooding, *paper SPE 20195 presented at the SPE/DOE Enhanced Oil Recovery Symposium*, Tulsa, OK. 22–25 April.

Fried, A. N.: 1961, The foam drive process for increasing the recovery of oil, *Technical report*, U.S. Dept of Interior, Bureau of Mines, Washington, DC. Report 5866.

Friedmann, F., Chen, W. H. and Gauglitz, P. A.: 1991, Experimental and simulation study of high-temperature foam displacement in porous media, *SPE Reservoir Engineering* **6**(1), 37–45. SPE-17357-PA.

Friedmann, F. and Jensen, J. A.: 1986, Some parameters influencing formation and propagation of foam in porous media, *paper SPE 15087 presented at the SPE California Regional Meeting*, Oakland, CA. 2–4 April.

Friedmann, F., Smith, M. E., Guice, W. R., Gump, J. M. and Nelson, D. G.: 1994, Steam-foam mechanistic field trial in the Midway-Sunset field, *SPE Reservoir Engineering* **9**(4), 297–304. SPE-21780-PA.

Gillis, J. V. and Radke, C. J.: 1990, A dual-gas tracer technique for determining trapped gas saturation during steady foam flow in porous media, *paper SPE 20519*

presented at the SPE Annual Technical Conference and Exhibition, New Orleans, LA. 23–26 September.

Goovaerts, P.: 1997, *Geostatistics for Natural Resources Evaluation*, Oxford University Press, Inc., New York, Oxford.

Haralick, R. M. and Shapiro, L. G.: 1992, *Computer and Robot Vision*, Addisonwesley Longman Publishing Co., Inc., Boston, MA, USA.

Hatziavramidis, D. T., Alameddine, B. R., Weinstein, H. G., Djabbarah, N. F. and Revay, J. M.: 1995, A mechanistic foam model for simulation of steam foam field applications, *paper SPE 30728 presented at the SPE Anuual Technical Conference and Exhibition*, Dallas, TX. 22–25 October.

Henry, R. L., Fisher, D. R., Pennell, S. P. and Honnert, M. A.: 1996, Field test of foam to reduce CO_2 cycling, *paper SPE 35402 presented at the SPE/DOE Improved Oil Recovery Symposium*, Tulsa, OK. 21–24 April.

Hill, A. D. and Rossen, W. R.: 1994, Fluid placement and diversion in matrix acidising, *paper SPE 27982 presented at the Tulas/SPE Centennial Petroleum Engineering Symposium*, Tulsa, OK. 29–31 August.

Hirasaki, G. J. and Lawson, J. B.: 1985, Mechanisms of foam flow in porous media: Apparent viscosity in smooth capillaries, *SPE Journal* **25**(2), 176–190.

Hodgman, C. D.: 1959, *CRC Standard Mathematical Table*, Chemical Rubble Publishing Co., Cleveland, OH.

Hubbert, M. K. and Willis, D. G.: 1957, Mechanics of hydraulic fracturing, *Trans. AIMME* **210**(6), 153–163.

Islam, M. R. and Ali, S. M. F.: 1990, Numerical simulation of foam flow in porous media, *Journal of Canadian Petroleum Technology* **29**(4), 47–51.

Ito, Y., Ichikawa, M. and Hirata, T.: 2001, The effects of gas injection on oil recovery during SAGD projects, *Journal of Canadian Petroleum Technology* **40**(1), 38–43.

Ito, Y. and Ipek, G.: 2005, Steam-fingering phenomenon during SAGD process, *paper SPE 97729 presented at the SPE/PS-CIM/CHAO International Thermal Operations and Heavy Oil Symposium*, Calgary, Alberta, Canada. 1–3 November.

Ito, Y. and Suzuki, S.: 1999, Numerical simulation of the SAGD process in the Hangingstone oil sands reservoir, *Journal of Canadian Petroleum Technology* **38**(9), 27–35.

Jimenez, A. I. and Radke, C. J.: 1989, *in* J. K. Borchardt and T. F. Yen (eds), *Oil-Field Chemistry: Enhanced Recovery and Production Stimulation*, ACS Symposium Series 396, Aerican Chemical Society, Washington, DC, chapter 25, pp. 460–479.

Jimenez, J.: 2008, The field performance of SAGD projects in canada, *paper IPTC 12860 presented at the International Petroleum Technology Conference*, Kuala Lumpur, Malaysia. 3–5 December.

Joshi, S. D. and Threlkeld, C. B.: 1985, Laboratory studies of thermally aided gravity drainage using horizontal wells, *AOSTRA J. of Research* **2**(1), 11–19.

Kam, S. I., Nguyen, Q. P., Li, Q. and Rossen, W. R.: 2007, Dynamic simulations with an improved model for foam generation, *SPE Journal* **12**(1), 35–48. SPE-90938-PA.

Kam, S. I. and Rossen, W. R.: 2003, A model for foam generation in homogeneous porous media, *SPE Journal* **8**(4), 417–425. SPE-77698-PA.

Kamath, V. A., Sinha, S. and Hatzignatiou, D. G.: 1993, Simulation study of steam-assisted gravity drainage process in Ugnu tar sand reservoir, *paper SPE 26075 presented at the SPE Western Regional Meeting*, Anchorage, Alaska, U.S.A. 26–28 May.

Khatib, Z. I., Hirasaki, G. J. and Falls, A. H.: 1988, Effects of capillary pressure on coalescence and phase mobilities in foams flowing through porous media, *SPE Reservoir Engineering* **3**(3), 919–926. SPE-15442-PA.

Kim, J., Dong, Y. and Rossen, W. R.: 2005, Steady-state foam behavior of CO_2 foam, *SPE Journal* **10**(4), 405–415.

Kisman, K. E. and Yeung, K. C.: 1995, Numerical study of the SAGD process in the Burnt Lake oil sands lease, *paper SPE 30276 presented at the SPE International Heavy Oil Symposium*, Calgary, Alberta, Canada. 19–21 June.

Kovscek, A. R.: 1994, *Foam Displacement in Porous Media: Experimental and Mechanistic Prediction by the Population Balance Method*, PhD thesis, University of California, Berkeley.

Kovscek, A. R., Patzek, T. W. and Radke, C. J.: 1995, A mechanistic population balance model for transient and steady-state foam flow in Boise sandstone, *Chem. Eng. Science* **50**(23), 3783–3799.

Kovscek, A. R., Patzek, T. W. and Radke, C. J.: 1997, Mechanistic foam flow simulation in heterogeneous and multidimensional porous media, *SPE Journal* **2**(4), 511–526. SPE-39102-PA.

Kovscek, A. R. and Radke, C. J.: 1994, Fundamentals of foam transport in porous media, *in* L. Schramm (ed.), *Foams: Fundamentals and Applications in the Petroleum*

Industry, ACS Symposium Series No. 242, American Chemical Society, Washington D.C., pp. 115–163.

Kovscek, A. R. and Radke, C. J.: 1996, Gas bubble snap-off under pressure-driven flow in constricted noncircular capillaries, *Colloids and Surfaces A: Physicochemical and Engineering Aspects* **117**(1–2), 55–76.

Kovscek, A. R. and Radke, C. J.: 2003, Pressure-driven capillary snap off of gas bubbles at low wetting-liquid content, *Colloids and Surfaces A: Physicochemical and Engineering Aspects* **212**(2–3), 99–108.

Kovscek, A. R., Tang, G. Q. and Radke, C. J.: 2007, Verification of Roof snap-off as a foam generation mechanism in porous media at steady state, *Colloids and Surfaces A: Physicochemical and Engineering Aspects* **302**(1–3), 251–260.

Marfoe, C. H., Kazemi, H. and Ramirez, W. F.: 1987, Numerical simulation of foam flow in porous media, *paper SPE 16790 presented at the SPE Annual Technical Conference and Exhibition*, Dallas, TX. 27–30 September.

Martinez, J. M.: 1996, *Foam-Flow Behaviour in Porous Media: Effects of Flow Regime and Porous-Medium Heterogeneity*, PhD thesis, The University of Texas at Austin.

Mast, R. F.: 1972, Microscopic behavior of foam in porous media, *paper SPE 3997 presented at the SPE Annual Meeting*, San Antonio, TX. 8–11 October.

Mohammadi, S. S., Coombe, D. A. and Stevenson, V. M.: 1993, Test of steam foam process for mobility control in S. Casper Creek reservoir, *Journal of Canadian Petroleum Technology* **32**(10), 49–54.

Myers, T. J. and Radke, C. J.: 2000, Transient foam displacement in the presence

of residual oil: Experiment and simulation using a population-balance model, *Ind. Eng. chem. Res.* **39**(8), 2725–2741.

Narasimhan, T. N. and Witherspoon, P. A.: 1976, An integrated finite difference method for analyzing fluid flow in porous media, *Water Resources Research* **12**(1), 57–64.

Nasr, T. N. and Ayodele, O. R.: 2006, New hybrid steam-solvent processes for the recovery of heavy oil and bitumen, *paper SPE 101717 presented at the SPE Abu Dhaba International Petroleum Exhibition and Conference*, Abu Dhabi. 5–8 November.

Nasr, T. N., Golbeck, H. and Heck, G.: 2003, Novel expanding solvent-SAGD process "ES-SAGD", *Journal of Canadian Petroleum Technology* **42**(1), 13–16.

Nasr, T. N., Law, D., Golbeck, H. and Korpany, G.: 2000, Counter-current aspect of the SAGD process, *Journal of Canadian Petroleum Technology* **39**(1), 41–47.

Osterloh, W. T. and Jante, M. J.: 1992, Effects of gas and liquid velocity on steady-state foam flow at high temperature, *paper SPE 24179 presented at the SPE/DOE Enhanced Oil Recovery Symposium*, Tulsa, OK. 22–24 April.

Owete, O. S. and Brigham, W. E.: 1987, Flow behavior of foam: A porous micromodel study, *SPE Journal* **2**(3), 315–323. SPE-11349-PA.

Parlar, M., Parris, M. D., Jasinski, R. and Robert, J. A.: 1995, An experimental study of foam flow through Berea sandstone with applications to foam diversion in matrix acidizing, *paper SPE 29678 presented at the SPE Western Regional Meeting*, Bakersfield, CA. 8–10 March.

Patzek, T. W.: 1988, Description of foam flow in porous media by the population balance approach, *in* D. Smith (ed.), *Surfactant-Based Mobility Control: Progress*

in Miscible-Flood Enhanced Oil Recover, American Chemical Society, Washington, DC, chapter 16, pp. 326–341.

Patzek, T. W.: 1993, Self-similar collapse of stationary bulk foams, *AIChE Journal* **39**(10), 1697–1707.

Patzek, T. W.: 1996, Field applications of steam foam for mobility improvement and profile control, *SPE Reservoir Engineering* **11**(2), 79–86. SPE-29612-PA.

Patzek, T. W. and Koinis, M. T.: 1990, Kern River steam-foam pilots, *Journal of Petroleum Technology* **42**(4), 496–503.

Patzek, T. W. and Myhill, N. A.: 1989, Simulation of the Bishop steam foam pilot, *paper SPE 18786 presented at the SPE California Regional Meeting*, Bakersfield, CA. 5–7 April.

Polikar, M., Cyr, T. J. and Coates, R. M.: 2000, Fast-SAGD: Half the wells and 30% less steam, *paper SPE 65509 presented at the SPE/PS-CIM International Conference on Horizontal Well Technology*, Calgary, Alberta, Canada. 6–8 November.

Pooladi-Darvish, M. and Mattar, L.: 2002, SAGD operations in the presence of overlying gas cap and water layer — effect of shale layers, *Journal of Canadian Petroleum Technology* **41**(6), 1–12.

Ransohoff, T. C., Gauglitz, P. A. and Radke, C. J.: 1987, Snap-off of gas bubbles in smoothly constricted noncircular capillaries, *AIChe Journal* **33**(5), 753–765.

Ransohoff, T. C. and Radke, C. J.: 1988, Mechanisms of foam generation in glass-bead packs, *SPE Reservoir Engineering* **3**(2), 573–585.

Redford, D. A. and Luhning, R. W.: 1999, In situ recovery from the Athabasca oil sands — past experience and future potential, part II, *Journal of Canadian Petroleum Technology* **38**(13), 1–13.

Reiss, J. C.: 1992, A steam-assisted gravity drainage model for tar sands: Linear geometry, *Journal of Canadian Petroleum Technology* **31**(10), 14–20.

Richardson, J. G., Harris, D. G., Rossen, R. H. and Hee, G. V.: 1978, The effect of small, discontinuous shales on oil recovery, *Journal of Petroleum Technology* **30**, 1531–1537.

Rossen, W. R.: 1996, *Foams in Enhanced Oil Recovery*, Marcel Dekker, Inc, New York.

Rossen, W. R. and Gauglitz, P. A.: 1990, Percolation theory and mobilization of foams in porous meida, *Am. Inst. Chem. Eng. J.* **37**(8), 1176–1188.

Rossen, W. R. and Wang, M. W.: 1997, Modeling foams for acid diversion, *paper SPE 38200 presented at the SPE European Formation Damage Conference*, The Hague, The Netherlands. 2–3 June.

Saltuklaroglu, M., Wright, G. N., Conrad, P. R., Conrad, J. R. and Manchester, G. J.: 2000, Mobil's SAGD experience at Celtic, Saskatchewan, *Journal of Canadian Petroleum Technology* **39**(4), 45–51.

Sasaki, K., Akibayashi, S., Yazawa, N., Doan, Q. T. and Ali, S. M. F.: 2001, Experimental modeling of the SAGD process — enhancing SAGD performance with periodic stimulation of the horizontal producer, *SPE Journal* **39**(4), 89–97. SPE-69742-PA.

Shin, H. and Polikar, M.: 2006, Fast-SAGD application in the Alberta oil sands areas, *Journal of Canadian Petroleum Technology* **45**(9), 46–53.

Shirley, A. I.: 1988, Foam formation in porous media: A microscopic visual study, *in* D. Smith (ed.), *Surfactant-Based Mobility Control: Progress in Miscible-Flood*

Enhanced Oil Recover, American Chemical Society, Washington, DC, chapter 16, pp. 234–257.

Stalder, J. L.: 2007, Cross SAGD (XSAGD) — an accelerated bitumen recovery alternative, *SPE Reservoir Evaluation & Engineering* **10**(1), 12–18. SPE-97647-PA.

Stone, H. L.: 1973, Estimation of three-phase relative permeability and residual oil data, *Journal of Canadian Petroleum Technology* **12**(4), 53–61.

Tan, T. B., Butterworth, E. and Yang, P.: 2002, Application of a thermal simulator with fully coupled discretized wellbore simulation to SAGD, *Journal of Canadian Petroleum Technology* **41**(1), 25–30.

Tang, G. Q. and Kovscek, A. R.: 2006, Trapped gas fraction during steady-state foam flow, *Transport in Porous Media* **65**(2), 287–307.

Turta, A. T. and Singhal, A. K.: 1998, Field foam applications in enhanced oil recovery projects: Screening and design aspects, *paper SPE 48895 presented at the SPE Annual Technical Conference and Exhibition*, Beijing, China. 2–6 November.

Vassenden, F. and Holt, T.: 1998, Experimental foundation for relative permeability modeling of foam, *paper SPE 39660 presented at the SPE/DOE Improved Oil Recovery Symposium*, Tulsa, OK. 19–22 April.

Vinsome, P. K. W. and Westerveld, J.: 1980, A simple method of predicting cap and base rock heat losses in thermal reservoir simulators, *Journal of Canadian Petroleum Technology* **19**(3), 87–90.

Webb, A. C., Schroder-Adams, C. J. and Pedersen, P. K.: 2005, Regional subsurface correlations of Albian sequences north of the Peace River in NE British Columbia:

Northward extent of sandstones of the Falher and Notikewin members along the eastern flank of the foredeep, *Bulletin of Canadian Petroleum Geology* **53**(2), 165–188.

Wen, X., Durlofsky, L. and Edwards, M.: 2003, Use of border regions for improved permeability upscaling, *Mathematical Geology* **35**(5), 521–547.

Yang, G. and Butler, R. M.: 1992, Effects of reservoir heterogeneities on heavy oil recovery by steam assisted gravity drainage, *Journal of Canadian Petroleum Technology* **31**(8), 37–43.

Zeilinger, S. C., M. Wang, K. R. K. and Rossen, W. R.: 1995, Improved prediction of foam diversion in matrix acidising, *paper SPE 29529 presented at the SPE Production Operations Symposium*, Oklahoma City, OK. 2–4 April.

Zhang, W., Youn, S. and Doan, Q.: 2007, Understanding reservoir architectures and steam-chamber growth at Christina Lake, Alberta, by using 4D seismic and crosswell seismic imaging, *SPE Reservoir Evaluation & Engineering* **10**(5), 446–452. SPE-97808-PA.

Zhou, Z. H. and Rossen, W. R.: 1995, Applying fractional flow theory to foam process at the limiting capillary pressure, *SPE Advanced Technology Series* **3**(1), 154–162. SPE-24180-PA.